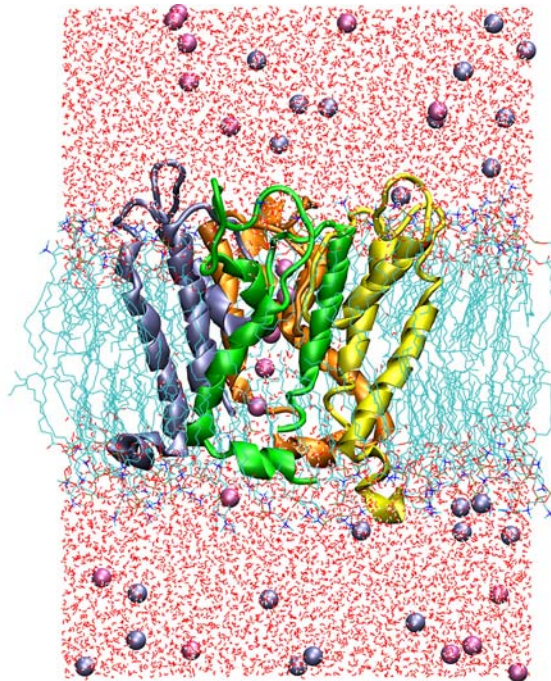


Computational study of the Kcv potassium channel



Von dem Fachbereich Biologie
der Technischen Universität Darmstadt

zur Erlangung des akademischen Grades
eines Doctor rerum naturalium (Dr. rer. nat.)

genehmigte Dissertation von

Dipl.-Biol. Sascha Tayefeh
aus Hanau

Berichterstatter: Prof. Dr. Gerhard Thiel
Mitberichterstatter: PD Dr. Stefan M. Kast, PD Dr. Adam Bertl

Tag der Einreichung: 1.6.2007
Tag der mündlichen Prüfung: 13.7.2007

Darmstadt 2007

*If one way be better than another,
that you may be sure is nature's way ...
Nature does nothing uselessly.
Aristotle*

Front page picture: Snapshot of a molecular dynamics simulation box.

All work presented in this thesis was performed by the author with the exception of the following contributions from others:

All **3D RISM calculations** throughout this work (Fig. 2.8, Fig 3.8, Fig 4.3 right) were carried out by Thomas Kloss, AG Kast, Eduard-Zintl Institut für Anorganische und Physikalische Chemie, Technische Universität Darmstadt.

The NMR structure of the Kcv N-terminus, which was used to construct chimera homology models (Fig. 3.2) was solved by the laboratory of Prof H. Schwalbe, Institut für Organische Chemie und Chemische Biologie, Johann Wolfgang Goethe-Universität, Frankfurt.

The molecular dynamics **trajectories with an external electric field** applied (Chapter 3: Kcv-HOM-K29_{deprot}-E1 and Kcv-HOM-K29_{deprot}-E2) were calculated by Michael Kreim.

Patch-clamp experiments on the Kcv-wt channel and its mutants, which are mentioned throughout this work, were carried out by:

Brigitte Hertel, Institut für Botanik, Technische Universität Darmstadt: KcvWT, KcvP13A, KcvΔN8, KcvΔN9. All published in (1).

Anna Moroni, Dipartimento di Biologia, CNR-IBF and INFM, Consiglio Nazionale della Ricerca-Istituto di Biofisica e Istituto Nazionale Fisica della Material, Unita di Milano UniVersita, Italy: KcvΔN14. Published in (2)

Manuela Gebhardt and Dirk Baumeister, Institut für Botanik, Technische Universität Darmstadt: Kcv-K29A, Kcv-K29H, Kcv-K29V, Kcv-K29L, Kcv-K29W, Kcv-K29S, Kcv-K29A (Fig 3.9).

-
- 1 Hertel, B. 2005. Struktur-Funktions-Beziehung in dem minimalen viralen K⁺ Kanal Kcv: Funktionelle Rolle des N-Terminus bei der Regulation von Kanalaktivität. PhD-Thesis. Technische Universität Darmstadt.
 - 2 Moroni, A., C. Visconti, V. Sangiorgio, C. Pagliuca, T. Meckel, F. Horvath, S. Gazzarrini, P. Valbuzzi, J. L. Van Etten, D. DiFrancesco, and G. Thiel. 2002. The short N-terminus is required for functional expression of the virus-encoded miniature K⁺ channel Kcv. *FEBS Lett.* 530:65-69.

Publications

Published and submitted papers:

Tayefeh, S., T. Kloss, G. Thiel, B. Hertel, A. Moroni, and S. M. Kast. 2007. Molecular Dynamics Simulation of the Cytosolic Mouth in Kcv-type Potassium Channels. *Biochemistry*. 46:4826-4839.

Hertel B., S. Tayefeh, M. Mehmel, S. M. Kast, J. L. Van Etten, A. Moroni, and G. Thiel. 2006. Elongation of outer transmembrane domain alters function of miniature K⁺ channel Kcv. 2006. *J. Membr. Biol.* 210:21-29.

Gazzarrini, S., M. Kang, J. L. Van Etten, S. Tayefeh, S. M. Kast, D. DiFrancesco, G. Thiel, and A. Moroni. 2004. Long-distance interactions within the potassium channel pore are revealed by molecular diversity of viral proteins. *J. Biol. Chem.* 279:28443-28449.

Papers in process:

Tayefeh, S., T. Kloss, M. Kreim, M. Gebhardt, D. Baumeister, B. Hertel, (Schwalbe group), (Weber group), A. Moroni, G. Thiel, and S. M. Kast. Model Development for the Viral Kcv Potassium Channel.

Contents

Chapter 1	General Introduction	1
Chapter 2	Molecular Dynamics Simulation of the Cytosolic Mouth in Kcv-type Potassium Channels	17
Chapter 3	Model Development for the Viral Kcv Potassium Channel	39
Chapter 4	The Dysfunctional Truncation Mutants	61
Chapter 5	Structure and Dynamics of the KcvP13A mutant model	65
Chapter 6	General Conclusion	69
	Zusammenfassung	73
Appendix I	Abbreviations	74
Appendix II	The Terminology of the Models	75
Appendix III	1- and 3-Letter Code of the Standard Amino Acids	76
Appendix IV	List of Scientific Computer Program	77
Appendix V	Computer Hardware	79
	Curriculum Vitae	80
	Danksagung	81
	Eidesstattliche Erklärung	82

Chapter 1

1 Introduction

K^+ channels are transmembrane proteins abundant in virtually all biological systems. Heartbeat regulation and the nervous system are only two of countless examples where K^+ channels play an important role (1). Although these have been subject to intense experimental and theoretical investigation, basic relationships between their structure and their function are not understood sufficiently. The main objective of this work was to explore structural, thermodynamic, and dynamical features of the viral K^+ channel Kcv on the atomic level. Of particular interest was the role of the N-terminal region. The studies were carried out by the means of molecular modeling, e.g. molecular dynamics (MD) simulations, Poisson-Boltzmann theory, normal mode analysis, and integral equation theory.

1.1 Potassium channels: An overview

1.1.1 Function

K^+ channels provide an energetically favorable pathway for K^+ ions across membranes (2). Without such specialized proteins, the hydrocarbon region of the lipid membrane would present a prohibitively high energy barrier to the passage of any ion (3). An ion pathway across a membrane cannot be an ordinary hole, since the regulation of the amount and the species of ions is essential for an efficient metabolism. Without regulation, for example, the cell could not keep up a membrane potential.

K^+ channels have the remarkable ability to conduct K^+ ions near the diffusion limit and yet, select for K^+ over similar ions like Na^+ by in some cases more than 1000 to 1 (2,4).

A channel is found either in a conducting ("open") or a non-conducting ("closed") state (5). The channel offers a pathway for K^+ ions only in the open state. A closed channel presents a barrier for ion transport. With a fluctuation between open and closed state ("gating"), the cell guards the ion transfer.

The experimental patch-clamp technique (2) provides the opportunity to monitor the function of ion channels (6). In such experiments, the membrane is clamped to a defined voltage. In this way, the current of one or more channel(s) can be measured. From the recording of these fluctuations, functional properties like, for example, conductivity, open-probability, and the dependency on various stimuli can be extracted.

1.1.2 Topology

Despite very low protein sequence identity between different K^+ channels, all channels with known X-ray structure share the same topology (7,8,9,10,11,12). K^+ channels appear to be oligomers in the active state and have a distinct number of transmembrane domains. The main

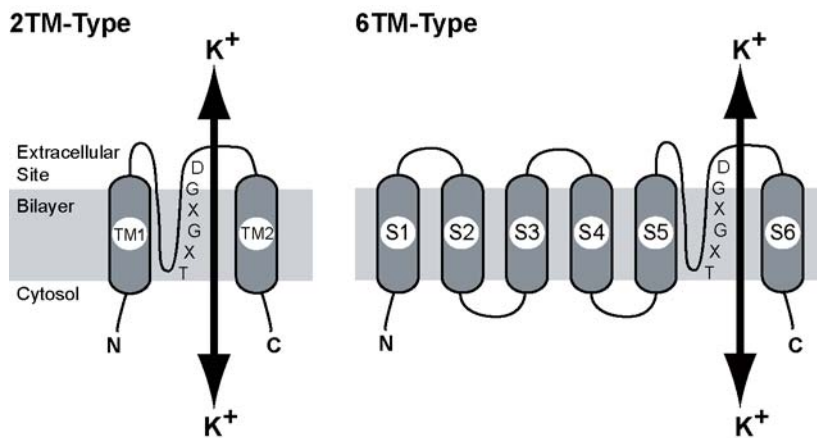


Figure 1.1: The topology of a 2TM-type (left) and a 6TM-type K^+ channel (right). The ion conduction pathway is determined by the selectivity filter (signature sequence "TXGXGD") located between the two C-terminal transmembrane domains.

("pore") region is the minimum unit necessary for the conduction of K^+ ions. It consists of two transmembrane (TM) domains per monomer. The short signature sequence ("TXGXGD") is part of the pore region. It is highly conserved and essential for ion selectivity ("selectivity filter") (13).

The basic K^+ channel type features the 2TM-motif (7,10). It consists of two transmembrane domains often referred to as "TM1" and "TM2" (Figure 1.1, left). The selectivity filter is located in between TM1 and TM2. In an extended K^+ channel type with the 6TM-motif (9,11,14,15), the basic structure is preceded by four additional hydrophobic transmembrane segments (Figure 1.1, right). The transmembrane domains of the 6TM-type channel are numbered from S1 to S6 (from the N- to the C-terminus). S5 and S6 is homolog to TM1 and TM2, respectively. Both the 2TM-motif and the 6-TM-motif type are usually tetramers in the active state. Besides, there are K^+ channel types with two pore domains in tandem. For example, a channel from *Caenorhabditis elegans* has been described with a monomer that consists of 2TM motifs (16), and in *Saccharomyces cerevisiae* a 2TM motif is linked to a 6TM motif. (17).

1.1.3 Atomic Structure

The first atomic structure of a K^+ channel was solved in 1998 (7) using X-ray crystallography. Until now, K^+ channel structures were determined from five more organisms (8,9,10,11,12). The typical resolution of a K^+ channel X-ray structures is $\sim 2\text{-}4 \text{ \AA}$.

As an example, Figure 1.2 shows the atomic structure of KirBac1.1, a 2TM-motif type inward-rectifying K^+ channel from *Burkholderia pseudomallei* (10). A cation crossing the channel from the extracellular site to the cytosol has to enter the narrow selectivity-filter first. The selectivity-filter is equipped with carbonyl oxygen atoms exposed to the K^+ conduction pathway (Figure 1.2., right). It has been suggested that the filter is constrained in an optimal geometry for coordinating dehydrated K^+ ions with carbonyl oxygen atoms (7,18,19). The selectivity filter replaces the hydration shell of the K^+ ion by coordinating the ion with oxygen atoms from the protein

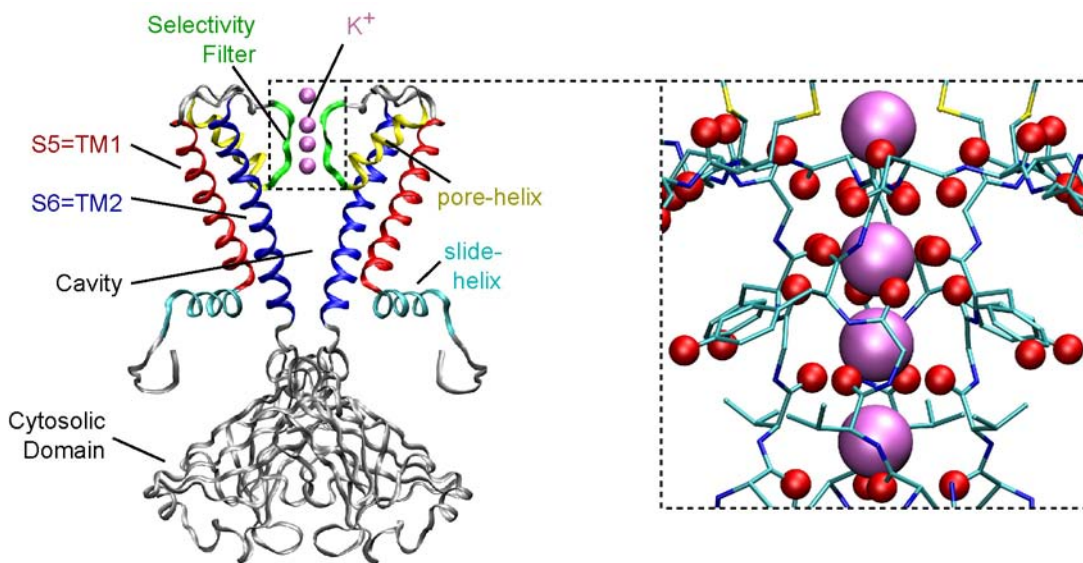


Figure 1.2: The atomic structure of the 2TM-type KirBac1.1 K^+ channel and cations as obtained from X-ray crystallography (10). LEFT: The backbone structure (ribbons) of two monomers. RIGHT: Detailed ball and stick view of the selectivity filter. K^+ ions: large magenta spheres. Oxygen atoms: small red spheres. For clarity, hydrogen atoms are neglected.

backbone. After passing the selectivity-filter, the K^+ ion enters the large, water-filled cavity. The hydration shell is rebuilt around K^+ ion by coordination with water molecules in the cavity. This architecture allows high K^+ ion throughput through the channel.

On the cytosolic site, the inner transmembrane domains as well as a large cytosolic domain are very narrow. Such a constriction ("cytosolic mouth") probably prevents further transition of the ion and led to the conclusion that this X-ray structure of KirBac1.1 is in the closed state (10). Concerted motion of the structural domains is suspected to enlarge the cytosolic mouth (20), allowing the further transition of K^+ ions into the cytosol. Indeed, X-ray structures of other K^+ channels show that the cytosolic mouth can appear in this proposed "open" conformation (7,9,11).

1.2 Kcv: A viral Potassium channels

PBCV-1 (*Paramecium bursaria* chlorella virus) is the prototype of the virus family *Phycodnaviridae* and infects green algae that live inside *P. bursaria* (21). The double-stranded DNA genome of PBCV-1 measures 330 kb (22), which is rather large for a viral genome. Sequence analysis predicts ~ 366 protein-encoding genes and 11 tRNA genes (23). Many gene products are exceptional for a virus, for example, DNA methyltransferases, DNA endonucleases, and, subject to this work, the K^+ channel termed Kcv (24). Kcv is a 2TM-type channel. With a monomer length of only 94 amino acids, this channel probably features just the most essential properties necessary for a functional channel.

Simple predictions provide a first impression of the structure (24,25,26). The C-terminus appears to be extraordinarily short and possibly lacks an attached cytosolic domain. A short N-terminal slide-helix is, just like in KirBac1.1, connected to TM1 via a kink-forming proline.

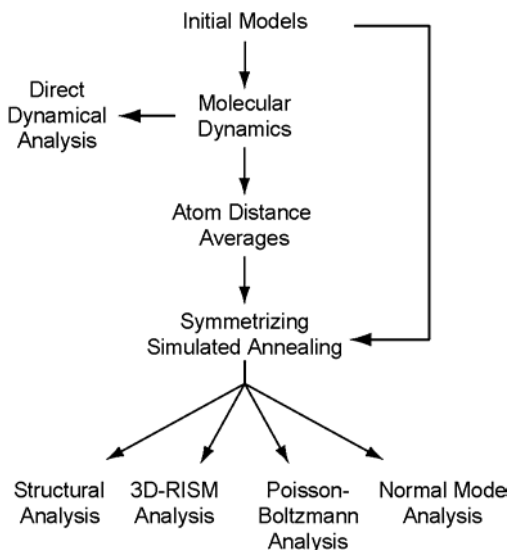


Figure 1.3: Modeling and analysis workflow.

gain of a time and voltage dependent component in the current-response (29). Hyperactivity and dysfunction have been interpreted as effects of elongated and truncated transmembrane domains (30), respectively, assigning anchoring and positioning function to TM1. The theoretical investigation of the impact of these mutations on the N-terminal region is the main objective of this work.

1.3 Theoretical Approach

To explore the role of the N-terminal region, insight into structural, thermodynamic, and dynamical properties of Kcv and some mutants on the atomic level would mean a major step forward. Theory provides appropriate tools that allow the study of these questions (31).

Figure 1.3 shows the modeling and analysis workflow of this work. Initial models were used as input for MD simulations. Apart from direct dynamical analysis, average atom distances of the protein were extracted from the trajectories. These distances were used for creating models reflecting the simulation environment. This was performed by a novel simulated annealing protocol introduced in this work. The final models were subject to further analysis.

1.3.1 Homology Modeling

The fabrication of a K⁺ channel crystal for X-ray crystallography is not straight forward. It may take years to find suitable conditions for a crystal to grow. The problem related to the determination of structures by nuclear magnetic resonance (NMR) spectroscopy concerns the size of a molecule. With increasing molecular size, the resolution of NMR spectra reduces, and K⁺ channels are too large to obtain useful spectra (32). Due to these difficulties, an experimental structure of the complete Kcv sequence has not been determined yet.

The prediction of protein structure, based primarily on sequence and structure homology ("homology modeling"), has become a popular tool in structural biology (33). In absence of

Kcv is well characterized by electrophysiological studies (24,27). It is slightly voltage-dependent and sensitive to typical K⁺ channel inhibitors (24). Single-channel measurements show that this channel fluctuates between open and closed state, just like larger K⁺ channels (28).

The short N-terminal slide-helix is essential for the function (26,29). Truncation mutants shortened by more than eight N-terminal amino-acids exhibit no current response in voltage-clamp experiments (29). Another interesting effect concerns some point-mutants. For example, replacing the kink-forming proline by alanine at position 13 (P13A) yields a hyperactive channel, which is characterized by a

experimental structures, homology modeling is the only method to create a model on the atomic level. With this method, a protein structure can be constructed by 3D aligning of the protein sequence to an appropriate 3D structure of a related protein. The iterative homology modeling cycle comprises the creation of a model, the refinement of the model, and the validation of the output structure. This cycle is repeated until there is no more improvement of the validated properties. The program package MODELLER (34) offers all these steps. It was used in this work for the creation of all initial homology models.

Since X-ray structures of other K⁺ channels are known, the construction of a homology model is possible (35). For a complete list of all constructed models and the terminology used in this work, see Appendix II.

1.3.2 Molecular Dynamics Simulation

MD simulation (36,37) was used in this work as a basic tool for generating dynamical and structural data in order to study Kcv and the impact of mutations. Many successful examples of MD simulations with macromolecular biological system have been published (e.g. 18,19,35, 38,39,40,41,42,43,44,45). The MD simulation technique is based on Newton's equations of motion:

$$\mathbf{F}_i(t) = m_i \mathbf{a}_i(t) = m_i \ddot{\mathbf{r}}_i(t) = -\nabla V_i(\mathbf{r}) = -\frac{\partial V_i(\mathbf{r})}{\partial \mathbf{r}_i} \quad (1.1)$$

where i is the particle index, \mathbf{r} the position, m the mass, \mathbf{F} the force, V the potential energy, and \mathbf{a} the acceleration. However, these equations cannot be solved analytically, but have to be integrated numerically. The discretization demands that an integration timestep is small enough to describe the fastest motion in the system, which is the vibration of hydrogen atoms. Thus, the typical time resolution of totally restraint-free MD simulations is 1 fs.

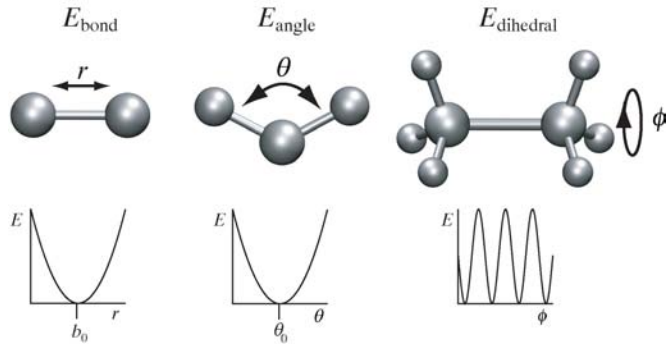
Equation 1.1 is solved numerically. The most widely used method of integrating Newton's equations of motion is the Verlet integrator (46):

$$\mathbf{r}_i(t + \delta t) = 2\mathbf{r}_i(t) - \mathbf{r}_i(t - \delta t) + \delta t^2 \mathbf{a}_i(t) \quad (1.2)$$

With this algorithm, the positions at $t + \delta t$ are calculated from the knowledge of the positions at $t - \delta t$ and the positions and accelerations at time t . All algorithms for controlling temperature and pressure of the simulation system basically modify equation 1.2 (47,48), which itself yields trajectories that conserve (approximately) the total energy.

In order to do so, potential functions (force fields) are necessary. Equation 1.1 also describes the relation between the force and the potential energy. (Semi-)Empirical potential functions have been developed over decades. They have been calibrated to experimental results and quantum mechanical calculations of small model compounds. Modern force fields are capable of

Bonded Interaction:



Non-Bonded Interaction:

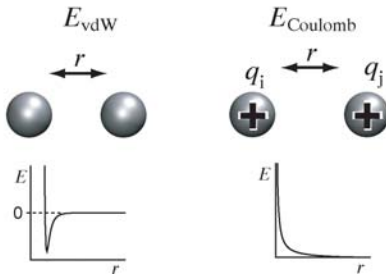


Figure 1.4: Illustration of the CHARMM potential energy function. The upper figures demonstrate the intramolecular energy terms $E_{\text{bond}}(r)$, $E_{\text{angle}}(\theta)$, and $E_{\text{dihedral}}(\phi)$. The intermolecular energy terms $E_{\text{vdW}}(r)$ and $E_{\text{Coulomb}}(r)$ (as an example for two cations) are illustrated in the lower part.

reproducing physical properties measured in experiments (observables) satisfactorily, even for large macromolecular systems (49).

In this work, the all-atom potential energy functions CHARMM22 for proteins (50) and CHARMM27 for phospholipids (51) were used for all MD calculations. Figure 1.4 illustrates the energy terms of the CHARMM force field. The value of the potential energy depends on coordinates such as the distance, r , the bond-length, b , or the dihedral angle, ϕ . It is represented as the sum of intramolecular (bonded) and intermolecular (non-bonded) energy terms:

$$V(r) = E_{\text{bonded}} + E_{\text{non-bonded}} \quad (1.3)$$

The intramolecular energy in the potential function has three components:

$$\begin{aligned} E_{\text{bonded}} &= E_{\text{bond}} + E_{\text{angle}} + E_{\text{dihedral}} \\ &= \sum_{1,2\text{pairs}} k_b(b - b_0)^2 + \sum_{\text{angles}} k_\theta(\theta - \theta_0)^2 + \sum_{1,4\text{pairs}} k_\phi(1 - \cos(n\phi)) \end{aligned} \quad (1.4)$$

The force constants, k , are related to the rigidity of the structure. The harmonic potential, E_{bond} , represents the interaction between an atom pair separated by a covalent bond (1,2-pairs). It calculates the energy of a bond as a function of its displacement from a certain bond length, b_0 . E_{angle} is also a harmonic potential and approximates the ideal bond angle potential energy, θ_0 , of three atoms. Finally, E_{dihedral} approximates the periodic torsion angle potential energy. ϕ is the dihedral angle and n is a multiplicity coefficient. All force constants and target values depend on the atom type. The force constants, k , and the target values, b_0 and θ_0 , also depend on the atom type and can be obtained by either experimental data or quantum mechanical calculations.

The intermolecular energy is a sum of two terms:

$$\begin{aligned} E_{\text{non-bonded}} &= E_{\text{vdW}} + E_{\text{Coulomb}} \\ &= \sum_{\text{non-bonded pairs}} 4\epsilon_{ij} \left[\left(\frac{\sigma_{ij}}{r_{ij}} \right)^{12} - \left(\frac{\sigma_{ij}}{r_{ij}} \right)^6 \right] + \sum_{\text{non-bonded pairs}} \frac{q_i q_j}{4\pi\epsilon_0 r_{ij}} \end{aligned} \quad (1.5)$$

The first sum, also known as the Lennard-Jones (6-12) potential, represents the interaction energy of two non-bonded atoms. The Lennard-Jones potential has a core repulsive tail of $(1/r_{ij})^{12}$, an attractive tail of $-(1/r_{ij})^6$, and a negative well depth ϵ_{ij} . The distance between the particles i and j is described by r_{ij} , while ϵ and σ are empiric parameters that depend on atom types. The Lennard-Jones potential of two atoms with different ϵ and σ can be calculated using the Lorentz-Berthelot mixing rule. In particular, ϵ_{ij} is the geometric mean of ϵ_i and ϵ_j :

$$\epsilon_{ij} = \sqrt{\epsilon_i \epsilon_j} \quad (1.6)$$

and σ_{ij} is the arithmetic mean of σ_i and σ_j :

$$\sigma_{ij} = \frac{\sigma_i + \sigma_j}{2} \quad (1.7)$$

The second sum of equation 1.5 concerns the electrostatic interaction. It is represented by a Coulomb potential, where q_i and q_j are the charges on the particles i and j and ϵ_0 is the vacuum dielectric constant. Electrostatic interactions have the longest range in this force field model. The calculation of long-range potentials is computationally expensive. A common way to handle long-range potentials is the Ewald sum (52). To save computational time, a grid-based technique called "Particle Mesh Ewald Method" (53) was used in this work to calculate the electrostatic interaction during the MD simulations.

The simulations in this work were performed with channel models in explicit membrane bilayer and solvent to incorporate the environmental effects (Figure 1.5). Throughout all simulations, the

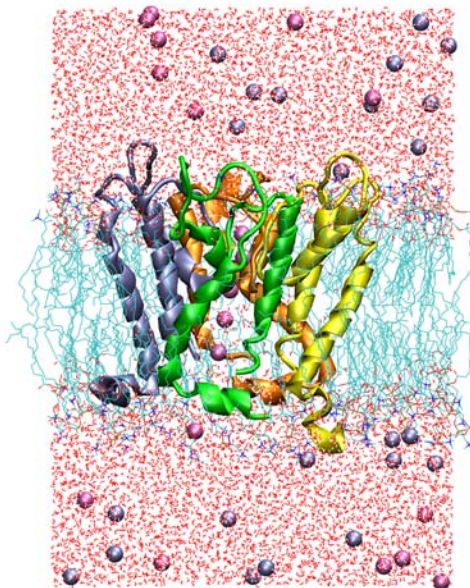


Figure 1.5: Snapshot of a typical simulation box containing a homology model of Kcv embedded in lipid-bilayer and solved in 100 mM KCl solution ($\sim 5 \cdot 10^4$ atoms). The backbone structure of the protein is represented by ribbons (each monomer is colored individually). Ions are shown as magenta (K^+) and blue (Cl^-) spheres. The lipid bilayer in the center and the surrounding water above and below the layer are drawn as lines.

TIP3P (Transferable Intermolecular Potential 3 Points) water model (54) was used. This water model is optimized for the usage with the CHARMM force fields. While MD simulations of K^+ channels are typically based on experimental X-ray structures, examples of successful simulations of homology models have been described in the literature (55,56). A typical simulation box created in this work contained $\sim 5 \cdot 10^4$ atoms. Such a box was constructed by 1) centering the channel in the box, 2) building a membrane around the protein, and 3) overlaying a solvent box with TIP3P water model and deleting water molecules and ions overlapping with the channel/lipid-complex. These tasks were performed by using academic version of CHARMM V3b1 (57).

MD simulations of macromolecular systems are generally computationally expensive. For N particles, a set of $3N$ differential equations have to be solved numerically in order to yield a trajectory that describes the positions, velocities, and accelerations of the particles as they evolve with time.

However, modern computer parks provide the computational power to overcome this task, and MD simulations performed today use a large number of parallel processors. In this work, ~ 1 ns trajectory per day were calculated with 32 IBM p575 processors for a simulation of $\sim 5 \cdot 10^4$ atoms using the NAMD molecular dynamics package (58). All production runs were done on the IBM Regatta machines at the Hochschulrechenzentrum Darmstadt and at the Forschungszentrum Jülich.

The calculation of observables by the means of MD simulations is based on statistical mechanics (59,60,61). The fundamental ergodic hypothesis states that an ensemble average

$\langle O \rangle_{\text{ensemble}}$ equals the time average $\langle O \rangle_{\text{time}}$. Since an experimental observable $O_{\text{experiment}}$ is regarded as a time average $\langle O \rangle_{\text{time}}$ it can be stated that

$$O_{\text{experiment}} = \langle O \rangle_{\text{ensemble}} = \langle O \rangle_{\text{time}} \quad (1.8)$$

$\langle O \rangle_{\text{time}}$ can be calculated directly from trajectories obtained by MD simulations (36).

1.3.3. Analytic Calculations

In this work, we introduced an annealing protocol for extracting average all-atom structures from very long trajectories. These average structures were used for further analysis by applying analytical theories. The Poisson-Boltzmann theory, the integral equation theory in form of the 3D reference interaction site model (RISM), and the normal mode analysis was used to study the K^+ channel models.

Poisson-Boltzmann (PB) Theory: In the PB equation the ionic solvent is simplified to a continuum phase. The equation describes the electrostatic potential around solutes in homogeneous ionic solutions as a function of space (62).

A possible notation of the PB equation is:

$$\nabla \cdot [\epsilon(\mathbf{r}) \nabla \phi(\mathbf{r})] - \kappa(\mathbf{r})^2 \phi(\mathbf{r}) = -4\pi\rho(\mathbf{r}) \quad (1.9)$$

where $\phi(\mathbf{r})$ is the electrostatic potential, $\rho(\mathbf{r})$ is the total atomic charge distribution in the system, i.e. the sum of fixed (protein) charge and mobile ionic charge distribution, $\epsilon(\mathbf{r})$ is the dielectric constant, and $\kappa(\mathbf{r})$ represents the ionic screening. In practice, the \mathbf{r} -dependent functions are mapped onto a 3D grid to sample the electrostatic potential of the space. A simple example is shown in (Figure 1.6), where this method was applied to the zwitterion alanine. As one would expect, a negative potential was determined for the space around the negatively charged oxygen

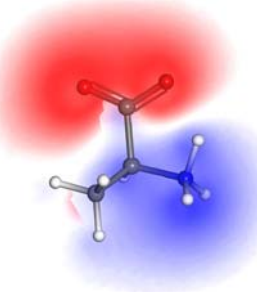


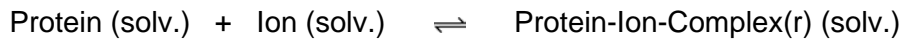
Figure 1.6: 3D distribution of the electrostatic potential of $\phi(\mathbf{r})$ of the zwitterion alanine in homogeneous water environment as calculated by applying the Poisson-Boltzmann equation onto a 3D grid. The red fog represent negative, the blue fog positive values of $\phi(\mathbf{r})$. The picture was created with MOLCAD (written by J. Brickmann and extended by M. Keil).

atoms, while for the space around the positively charged nitrogen a positive potential was calculated.

Using an extension of this method (63), the electrostatic free energy of an ion transferring from bulk to a point \mathbf{r} near the protein can be determined. The electrostatic free energy ΔG is

$$\Delta G = \frac{1}{2} \sum q_i \phi(\mathbf{r}_i) \quad (1.10)$$

where $\phi(\mathbf{r}_i)$ is the electrostatic potential from the PB equation at the position of the atomic charge q_i . For a reaction of the type



the electrostatic free energy to transfer an ion from bulk solution to a point \mathbf{r} near the protein ($\Delta\Delta G(\mathbf{r})$) can be calculated as the difference between the electrostatic free energy of the protein-ion complex (pi), the pure protein (p) and the ion (i) in bulk:

$$\Delta\Delta G(\mathbf{r}) = \Delta G_{\text{pi}}(\mathbf{r}) - \Delta G_{\text{p}} - \Delta G_{\text{i}} \quad (1.11)$$

By evaluating equation 1.11 for various \mathbf{r} along a specific (not necessarily physically meaningful) K^+ ion conduction pathway, a 1D electrostatic free energy profile of an ion transferring from bulk to a point \mathbf{r} can be calculated.

All the calculations were performed using the PBEQ module (64,65,66) which is implemented into the academic version of CHARMM V3.1b (57).

Integral Equation Theory: Another analytic method used in this work deals with the ion density distribution around proteins. This method is based on the integral equation theory in the form of the 3D-RISM (reference interaction site model) (67). With this method, it is possible to calculate the distribution of aqueous KCl solution around the protein. In reciprocal space, the 3D-RISM equations are:

$$\hat{h}_i = \sum_j \hat{c}_i \hat{\chi}_{ij} \quad (1.12)$$

where χ is the solvent susceptibility that depends on the type, temperature, and the density of the solvent, h and c are the matrices of the total and direct correlation functions, respectively. The carets denote the Fourier-transform and i and j are the solvent site indices. If $h_i(\mathbf{r})$ is given, the 3D distribution function $g_i(\mathbf{r})$ of a solvent atom for a rigid body in space can be determined by

$$g_i(\mathbf{r}) = h_i(\mathbf{r}) + 1 \quad (1.13)$$

Another relation between the correlation functions in addition to the RISM integral equation needs to be evaluated in order to calculate the correlation functions. This relation is given by the so-called "closure". In this work, the Kovalenko-Hirata (KH) closure (68) was used:

$$h_i(\mathbf{r}) = \begin{cases} \exp(d_i(\mathbf{r})) - 1 & \text{if } d_i(\mathbf{r}) < 0 \\ d_i(\mathbf{r}) & \text{else} \end{cases} \quad (1.14)$$

$$d_i(\mathbf{r}) = -\beta u_i(\mathbf{r}) + h_i(\mathbf{r}) - c_i(\mathbf{r})$$

where $u_i(\mathbf{r})$ is the interaction potential between solute molecule and the solvent site i , $\beta = (k_B T)^{-1}$, k_B is the Boltzmann constant and T is the temperature.

Additionally, we used a second order variant of the KH closure, termed KH-2 (69):

$$h_i(\mathbf{r}) = \begin{cases} \exp(d_i(\mathbf{r})) - 1 & \text{if } d_i(\mathbf{r}) < 0 \\ d_i(\mathbf{r}) + d_i^2(\mathbf{r})/2 & \text{else} \end{cases} \quad (1.15)$$

$$d_i(\mathbf{r}) = -\beta u_i(\mathbf{r}) + h_i(\mathbf{r}) - c_i(\mathbf{r})$$

The non-linear 3D-RISM-Closure equation system can only be solved iteratively (70).

The relative ion density $g_{\text{ion}}(\mathbf{r})$ calculated with method is related to the ion free energy surface, W , of ion transport, also known as the "potential of mean force" (PMF):

$$W(\mathbf{r}) = -kT \ln g_{\text{ion}}(\mathbf{r}) \quad (1.16)$$

Thus, large relative densities can be interpreted as attractive areas in space for certain ion species. Relative ion densities determined with this method provide a more detailed picture of the ion distribution in space than the Poisson-Boltzmann method does. Small fragments of a K^+ channel have been studies with a simpler 1D version of this method (71,72), so this is the first time it was used to characterize the 3D ion free energy surface of a full-size K^+ channel.

All 3D-RISM calculations were performed by a local Fortran-code developed by T. Kloss and S. M. Kast.

Normal Mode Analysis: Long-range and large-timescale cooperative motion remains beyond the reach of MD simulation. Normal-mode analysis (NMA) is an analytic approach for exploring such long-range and large-scale dynamics (73). All NMA calculations in this work were done with NOMAD (74). The algorithm used by NOMAD realizes the so-called Elastic Network Model (75) to calculate normal modes. The usefulness of this approach to study the interconversion of K^+ channels between two forms has already been demonstrated (76,77).

1.4 Objectives and Outline

The objective of this work was the computational investigation of structural, thermodynamic, and dynamical features of Kcv, a viral K⁺ channel. In particular, the impact of mutations of the N-terminal region on the function (24,26,29,30) was examined by computational means. This work focuses on the Kcv wild type (24), some dysfunctional truncation mutants (26,29), and the hyperactive point mutant P13A (29). In absence of appropriate structural data of Kcv, theoretical models of Kcv and some mutants were studied in a fully solvated lipid environment by the means of 3D modeling, MD simulations, and analytic theory. The methods applied allowed the exploration of features on the atomic level. The dynamics were resolved with a resolution of 2 fs, and the upper time scale limit was ~ 100 ns.

A major part of this work is based on the assumption that there is a functional analogy between similar protein domains of all K⁺ channels. The introduction of this hypothesis in this work was motivated by the fact that all known K⁺ channels share the same topology, as it has been proven by the X-ray structures of six different K⁺ channels (7,8,9,10,11,12). It is reasonable to assume that analogous topology reflects, at least, coarse functional analogy. Such a functional analogy is supposed to be independent from the specific protein sequence, except for a number of pivotal or key residues that need to be identified. Model building can be based on this knowledge: In our case, we chose two independent approaches to model Kcv, one based on a truncated and appropriately mutated variant of KirBac1.1 (10) which shares several key residues with Kcv. (Chapter 2) The other was based on a homology model of Kcv which takes into account a number of experimental results from NMR spectroscopy and electrophysiology (Chapters 3-5). The advantage of an analog system compared to a homology model is the fact that the experimental structure is presumably closer to the native conformation than a homology model. The evaluation of the functional analogy hypothesis is another objective of this work: if both independent strategies yield basically the same structural and mechanistic insight, modeling artifacts can be ruled out; microscopic key features of the Kcv system have been understood, even in the absence of an X-ray structure.

In Chapter 2, three KirBac1.1 models were explored, including models analogous to the Kcv wild type, to a truncation mutant that lacks basic residues in the N-terminal slide helix, and to the Kcv point mutant P13A. The results comprise the dynamics of the K⁺ ions and pivotal salt bridges, average structures created by a novel simulated annealing protocol, and the exploration of structural properties by the application of Poisson-Boltzmann and 3D-RISM theory.

Chapter 3 deals with the homology modeling (34) of Kcv wild-type. The homology models were based on the KirBac1.1 X-ray structure. The question of the ionization state of a bilayer-exposed titrable residue was tackled and the dynamics of the K⁺ ions across the models was examined. The models were simulated and the novel simulated annealing protocol introduced in Chapter 2 was applied. Finally, the most reasonable model was identified.

Chapter 4 deals with the study of some dysfunctional Kcv truncation mutants. Three models were derived from the most reasonable Kcv wild type model introduced in Chapter 3 by truncating 8 and 14 N-terminal amino acids, respectively. Average structures were obtained and structural

and dynamical properties were determined using the same techniques as before. To investigate the possible reason for dysfunction, the results were compared to those presented in Chapter 2.

The results of the homology modeling procedure and MD simulation of the point mutant P13A are presented in Chapter 5. The efforts taken to create the model are summarized in this chapter as well as the specific problems related to that model. Besides structural and dynamical analysis, results of normal-mode calculations that hint to a motion possibly related to a common gating mechanism are presented.

A comparative conclusion of the results of all studies is given in Chapter 6.

Reference

1. Korn, S. J. and J. G. Trapani. 2005. Potassium channels. *IEEE Trans Nanobioscience*. 4:21-33.
2. Hille, B. 2001. Ion Channels of Excitable Membranes. Sinauer Associates Inc. Sunderland, MA.
3. Parsegian, A. 1969. Energy of an ion crossing a low dielectric membrane: Solution to four relevant electrostatic problems. *Nature*. 221:844-846.
4. Roux, B. 2005. Ion conduction and selectivity in K^+ channels. *Annu. Rev. Biophys. Biomol. Struct.* 34:153-171.
5. Neher, E., B. Sakmann. 1976. Single-channel currents recorded from membrane of denervated frog muscle muscle fibres. *Nature*. 260:799-802.
6. Neher, E., B. Sakmann, J. H. Steinbach. 1978. The extracellular patch clamp: a method for resolving currents through individual open channels in biological membranes. *Pflugers Arch.* 375:219-228.
7. Doyle, D. A., J. C. Cabral, R. A. Pfuetzner, A. Kuo, J. M. Gulbis, S. L. Cohen, B. T. Chain, and R. MacKinnon. 1998. The structure of the potassium channel: molecular basis of K^+ conduction and selectivity. *Science*. 280:69-77.
8. Jiang, Y., A. Lee, J. Chen, M. Cadene, B. T. Chait, and R. MacKinnon. 2002. Crystal structure and mechanism of a calcium-gated potassium channel. *Nature*. 417:515-522.
9. Jiang, Y., A. Lee, J. Chen, V. Ruta, M. Cadene, B. T. Chait, and R. MacKinnon. 2003. X-ray structure of a voltage-dependent K^+ channel. *Nature*. 423:33-41.
10. Kuo, A., J. M Gulbis, J. F. Antcliff, T. Rahman, E. D. Lowe, J. Zimmer, J. Cuthbertson, F. M. Ashcroft, T. Ezaki, and D. A. Doyle. 2003. Crystal structure of the potassium channel KirBac1.1 in the closed state. *Science*. 300:1922-1926.
11. Long, S. B., E. B. Campbell, and R. MacKinnon. 2005. Crystal structure of a mammalian voltage-dependent Shaker family K^+ channel. *Science*. 309:897-903.
12. Shi, N., Y. Sheng, A. Alam, L. Chen, and Y. Jiang. 2006. Atomic structure of a Na^+ and K^+ conducting channel. *Nature*. 23:427-429.
13. Heginbotham, L., T. Abramson, and R. A. MacKinnon. 1992. Functional connection between the pores of distantly related ion channels as revealed by mutant K^+ channels. *Science*. 258:1152-1155.
14. Uozumi, N., T. Nakamura, J. I. Schroeder, and S. Muto. 1998. Determination of transmembrane topology of an inward-rectifying potassium channel from *Arabidopsis thaliana* based on functional expression in *Escherichia coli*. *Proc. Natl. Acad. Sci. USA*. 95:9773-9778.
15. Shih, T. M., and A. L. Goldin. 1997. Topology of the Shaker potassium channel probed with hydrophilic epitope insertions. *J. Cell Biol.* 136:1037-1045.
16. Goldstein, S. A., L. A. Price, D. N. Rosenthal, and M. H. Pausch. 1996. ORK1, a potassium-selective leak channel with two pore domains cloned from *Drosophila melanogaster* by expression in *Saccharomyces cerevisiae*. *Proc. Natl. Acad. Sci. USA*. 93:13256-13261.
17. Ketchum, K. A., W. J. Joiner, A. J. Sellers, L. K. Kaczmarek, and S. A. Goldstein. 1995. A new family of outwardly rectifying potassium channel proteins with two pore domains in tandem. *Nature*. 376:690-95
18. Domene, C., and M. S. P. Sansom. 2003. Potassium channel, ions, and water: simulation studies based on the high resolution X-ray structure of KcsA. *Biophys. J.* 85:2787-2800.
19. Biggin, P. C., G. R. Smith, I. Shrivastava, S. Choe, and M. S. P. Sansom. 2001. Potassium and

-
- sodium ions in a potassium channel studied by molecular dynamics simulations. *Biochim. Biophys. Acta.* 1510:1-9.
20. Jiang, Y., A. Lee, J. Chen, M. Cadene, B. T. Chait B. T., and R. MacKinnon. 2002. The open pore conformation of potassium channels. *Nature.* 417:523-526.
21. Van Etten, J. L., R. H. Meints, D. Kuczmarski, D. E. Burbank, and K. Lee. 1982. Viruses of symbiotic Chlorella-like algae isolated from Paramecium bursaria and *Hydra viridis*. *Proc. Natl. Acad. Sci. USA.* 79:3867-3871.
22. Van Etten, J.L., M. V. Graves, D. G. Müller, W. Boland, N. Delaroque. 2002. Phycodnaviridae - large DNA algal viruses. *Arch. Virol.* 147:1479-1516.
23. Yamada T., H. Onimatsu, and J. L. Van Etten. 2006. Chlorella viruses. *Adv. Virus. Res.* 66:293-336
24. Plugge B., S. Gazzarrini, M. Nelson, R. Cerana, J. L. Van Etten, C. Derst, D. DiFrancesco, A. Moroni, and G. Thiel. 2000. A potassium channel protein encoded by chlorella virus PBCV-1. *Science.* 287:1641-1644.
25. Gazzarrini, S., M. Kang, J. L. Van Etten, S. Tayefeh, S. M. Kast, D. DiFrancesco, G. Thiel, and A. Moroni. 2004. Long-distance interactions within the potassium channel pore are revealed by molecular diversity of viral proteins. *J. Biol. Chem.* 279:28443-28449.
26. Moroni, A., C. Visconti, V. Sangiorgio, C. Pagliuca, T. Meckel, F. Horvath, S. Gazzarrini, P. Valbuzzi, J. L. Van Etten, D. DiFrancesco, and G. Thiel. 2002. The short N-terminus is required for functional expression of the virus-encoded miniature K⁺ channel Kcv. *FEBS Lett.* 530:65-69.
27. Gazzarrini, S., M. Severino, M. Lombardi, M. Morandi, D. DiFrancesco, J. L. Van Etten, G. Thiel, and A. Moroni. 2003. The viral potassium channel Kcv: structural and functional features. *FEBS Lett.* 552:12-16.
28. Pagliuca, C., T. A. Goetze, R. Wagner, G. Thiel, A. Moroni, and D. Parcej. 2007. Molecular properties of Kcv, a virus encoded K⁺ channel. *Biochemistry.* 46:1079-1090.
29. Hertel, B. 2005. Struktur-Funktions-Beziehung in dem minimalen viralen K⁺ Kanal Kcv: Funktionelle Rolle des N-Terminus bei der Regulation von Kanalaktivität. PhD-Thesis. Technische Universität Darmstadt.
30. Hertel B., S. Tayefeh, M. Mehmel, S. M. Kast, J. L. Van Etten, A. Moroni, and G. Thiel. 2006. Elongation of outer transmembrane domain alters function of miniature K⁺ channel Kcv. 2006. *J. Membr. Biol.* 210:21-29.
31. Roux, B. 2002. Theoretical and computational models of ion channels. *Curr. Opin. Struct. Biol.* 12:182-189.
32. Liu, H.-L. and J.-P. Hsu. 2005. Recent developments in structural proteomics for protein structure determination. *Proteomics.* 5:2056-2068.
33. Goldsmith-Fischman, S. and B. Honig. 2003. Structural genomics: computational methods for structure analysis. *Protein Sci.* 12:1813-1821.
34. Sali A. and T. L. Blundell. 1993. Comparative protein modelling by satisfaction of spatial restraints. *J. Mol. Biol.* 234:779-815.
35. Sansom, M. S. P., I. H. Shrivastava, J. N. Bright, J. Tate, C. E. Capener, and P. C Biggin. 2002. Potassium channels: structures, models, simulations. *Biochim. Biophys. Acta.* 1565:294-307.
36. Allen, M. P., D. J. Tildesley. 1987. Computer simulation of liquids. Clarendon Press, Oxford.
37. Haberlandt, R., S. Fritzsch, G. Peinel, and K. Heinzinger. Molekulardynamik. 1995. Viewer, Wiesbaden.
38. Roux, B., T. Allen, S. Berneche, and W. Im. 2004. Theoretical and computational models of biological ion channels. *Q. Rev Biophys.* 37:15-103.
39. Beckstein, O., P. C. Biggin, P. Bond, J. N. Bright, C. Domene, A. Grottesi, J. Holyoake, and M. S. P. Sansom. 2003. Ion channel gating: insights via molecular simulations. *FEBS Lett.* 555:85-90.
40. Tieleman, P. D. 2006. Computer simulations of transport through membranes: passive diffusion, pores, channels and transporters. *Clin. Exp. Pharmacol. P.* 33;893-903.
41. Faraldo-Gomez , J. D., G. R. Smith, and M. S. P. Sansom. Setting up and optimization of membrane protein simulations. *Eur Biophys J.* 2002. 31:217-227.
42. Capener, C. E., I. H. Shrivastava, K. M. Ranatunga, L. R. Forrest, G. R. Smith, and M. S. P. Sansom. 2000. Homology modeling and molecular dynamics simulation studies of an inward rectifier potassium channel. *Biophys. J.* 78:2929-2942.
43. Charlotte, C. E., H. J. Hyun, Y. Arinaminpathy, and M. S. P. Sansom. 2002. Ion channels:

-
- structural bioinformatics and modelling. *Hum. Mol. Genet.* 11:2425-2433.
44. Haider, S., A. Grottesi, B. A. Hall, F. M. Ashcroft, and M. S. P. Sansom. 2005. Conformational dynamics of the ligand-binding domain of inward rectifier K channels as revealed by molecular dynamics simulations: toward an understanding of Kir channel gating. *Biophys. J.* 88:3310-3320.
45. Yu, K., W. Fu, H. Liu, X. Luo, K. X. Chen, J. Ding, J. Shen, and H. Jiang. 2004. Computational simulations of interactions of scorpion toxins with the voltage-gated potassium ion channel. *Biophys. J.* 86:3542-3555.
46. Verlet, L. 1967. Computer 'experiments' on classical fluids. II. Equilibrium correlation functions. *Phys. Rev.* 165:201-214.
47. Tu, K., D. J. Tobias, and M. L. Klein. 1995. Constant pressure and temperature molecular dynamics simulation of a fully hydrated liquid crystal phase dipalmitoylphosphatidylcholine bilayer. *Biophys. J.* 69:2558-2562.
48. Feller, S. E., Y. Zhang, R. W. Pastor, and B. R. Brooks. 1995. Constant pressure molecular dynamics simulation: the Langevin piston method. *J. Chem. Phys.* 103:4613-4621.
49. Kandt, C., Ash, W. L., and P. Tieleman. 2006. Setting up and running molecular dynamics simulations of membrane proteins. *Methods.* 41:475-88.
50. MacKerell Jr. A. D., D. Bashford, M. Bellott, R. L. Dunbrack, J. D. Evanseck, M. J. Field, S. Fischer, J. Gao, H. Guo, S. Ha, D. Joseph-McCarthy, L. Kuchnir, K. Kuczera, F. T. K. Lau, C. Mattos, S. Michnick, T. Ngo, D. T. Nguyen, B. Prodhom, W. E. Reiher, B. Roux, M. Schlenkrich, J. C. Smith, R. Stote, J. Straub, M. Watanabe, J. Wiorkiewicz-Kuczera, D. Yin, and M. Karplus. 1998. All-atom empirical potential for molecular modelling and dynamics Studies of proteins. *J. Phys. Chem. B* 102:3586-3616.
51. Schlenkrich, M., J. Brickmann, A. D. MacKerell Jr., and M. Karplus. 1996. An empirical potential energy function for phospholipids: criteria for parameter optimization and applications. In Biological Membranes: A Molecular Perspective from Computation and Experiment. K. M. Merz and B. Roux, editors. Birkhäuser, Boston. 31-81.
52. Ewald, P. 1921. Die Berechnung optischer und elektrostatischer Gitterpotentiale. *Ann. Phys.* 64:253-287.
53. Essmann, U., L. Perera, M. L. Berkowitz, T. Darden, H. Lee, and L. G. Pedersen. 1995. A smooth particle mesh Ewald method. *J. Chem. Phys.* 103:8577-8593.
54. Jorgensen, W. L., J. Chandrasekhar, and J. D. Madura. 1983. Comparison of simple potential functions for simulating liquid water. *J. Chem. Phys.* 79:926-935.
55. Capener, C. E., I. H. Shrivastava, K. M. Ranatunga, L. R. Forrest, G. R. Smith, and M. S. P. Sansom. 2000. Homology modeling and molecular dynamic simulation studies of an inward rectifier potassium channel. *Biophys. J.* 28:2929-2942.
56. Charlotte, C. E., H. J. Hyun, Y. Arinaminpathy, and M. S. P. Sansom. 2002. Ion channels: structural bioinformatics and modelling. *Hum. Mol. Genet.* 11:2425-2433.
57. Brooks, B. R., R. E. Bruccoleri, B. D. Olafson, D. J. States, S. Swaminathan, and M. Karplus. 1983. CHARMM: a program for macromolecular energy, minimization, and dynamics calculations. *J. Comput. Chem.* 4:187-217.
58. Kale, L., R. Skeel, M. Bhandarkar, R. Brunner, A. Gursoy, N. Krawetz, J. Phillips, A. Shinozaki, K. Varadarajan, and K. Schulten. 1999. NAMD2: greater scalability for parallel molecular dynamics. *J. Comput. Phys.* 151:283-312.
59. Hill, T. L. 1956. Statistical mechanics. McGraw-Hill, New York.
60. McQuarrie, D. 1976. Statistical Mechanics. Harper and Row, New York.
61. Chandler, D. 1987. Introduction to modern statistical mechanics. Oxford University Press, New York.
62. Honig B., and A. Nicholls. 1995. Classical electrostatics in biology and chemistry. *Science* 268:1144-1149.
63. Jogini, V., and B. Roux. 2005. Electrostatics of the intracellular vestibule of K⁺ channels. *J. Mol. Biol.* 354:272-288.
64. Nina, M., D. Beglov, and B. Roux. 1997. Atomic Radii for Continuum Electrostatics Calculations based on Molecular Dynamics Free Energy Simulations. *J. Phys. Chem. B.* 101:5239-5248.
65. Im, W., D. Beglov, and B. Roux. 1998. Continuum solvation model: Electrostatic forces from numerical solutions to the Poisson-Boltzmann equation, *Comput. Phys. Commun.* 111:59-75.

-
66. Roux, B. 1997. The influence of the membrane potential on the free energy of an intrinsic protein. *Biophys. J.* **73**:2980-2989.
 67. Kovalenko, A., and F. Hirata. 1998. Three-dimensional density profiles of water in contact with a solute of arbitrary shape: a RISM approach. *Chem. Phys. Lett.* **290**:237-244.
 68. Kovalenko, A., and F. Hirata. 1999. Potential of mean force between two molecular ions in a polar molecular solvent: a study by the three-dimensional reference interaction site model. *J. Phys. Chem. B* **103**:7942-7957.
 69. Omelyan, I., A. Kovalenko, and F. Hirata. 2004. Microscopic description of a liquid-vapor interface by an inhomogeneous integral equation theory. *Chem. Phys. Lett.* **397**:368-373.
 70. Hirata, F. 2003. Molecular Theory of Solvation. Kluwer Academic Publishers, Dordrecht.
 71. Cui, Q. Z., and V. H. Smith. 2002. K^+/Na^+ selectivity of KcsA potassium channel analyzed by reference interaction site model (RISM) integral equation theory. *Chem. Phys. Lett.* **365**:110-116.
 72. Cui, Q. Z., and V. H. Smith. 2005. Analysis of K^+/Na^+ selectivity of KcsA potassium channel with reference interaction site model theory. *Molec. Phys.* **103**:191-201.
 73. Brooks, B., and M. Karplus. 1983. Harmonic dynamics of proteins: normal modes and fluctuations in bovine pancreatic trypsin inhibitor. *Proc. Natl. Acad. Sci. USA.* **80**:6571-6757.
 74. Lindahl E., C. Azuara, P. Koehl, and M. Delarue. 2006. NOMAD-Ref: visualization, deformation and refinement of macromolecular structures based on all-atom normal mode analysis. *Nucleic Acids Res.* **34**:W52-W56.
 75. Tirion, M. M. 1996. Large Amplitude Elastic Motions in Proteins from a Single-Parameter, Atomic Analysis. *Phys. Rev. Lett.* **77**:1905-1908.
 76. Shen, Y., Y. Kong, and J. Ma. 2002. Intrinsic flexibility and gating mechanism of the potassium channel KcsA. *Proc. Natl. Acad. Sci. USA.* **99**:1949-1953.
 77. Srivastava, I. H., and I. Bahar. 2006. Common Mechanism of Pore Opening Shared by Five Different Potassium Channels. *Biophys. J.* **90**:3929-3940.

Chapter 2

Molecular Dynamics Simulation of the Cytosolic Mouth in Kcv-type Potassium Channels

Sascha Tayefeh^{*,†}, Thomas Kloss^{*}, Gerhard Thiel,[†] Brigitte Hertel,[†] Anna Moroni,[‡] and Stefan M. Kast^{*}

^{*}Eduard Zintl-Institut für Anorganische und Physikalische Chemie, [†]Institut für Botanik, Technische Universität Darmstadt, Germany; and [‡]Dipartimento di Biologia, CNR-IBF & INFM: Consiglio Nazionale della Ricerca-Istituto di Biofisica e Istituto Nazionale Fisica della Material, Unità di Milano Università, Milan, Italy

KEYWORDS Viral Potassium Channels, Kcv, KirBac1.1, Gating, Molecular Dynamics Simulations, Simulated Annealing, Poisson-Boltzmann Theory, CHARMM

Abstract

The functional effect of mutations near the intracellular mouth of the short viral Kcv potassium channel was studied by molecular dynamics simulations. As model system we used the analogously mutated and truncated KirBac1.1, a channel with known crystal structure that shares genuine local sequence motifs with Kcv. By a novel simulated annealing methodology for structural averaging, information about the structure and dynamics of the intracellular mouth was extracted and complemented by Poisson-Boltzmann and 3D-RISM (reference interaction site model) integral equation theory for the determination of the K^+ free energy surface. Besides the wild-type analog of Kcv with its experimental reference activity (truncated KirBac1.1), two variants were studied: a deletion mutant where the N-terminus is further truncated by eight amino acids showing inactivity in the Kcv reference system, and a point mutant where the kink-forming proline at position 13 is substituted by alanine, resulting in hyperactivity. The computations reveal that the change of activity is closely related to a hydrophilic intracellular constriction formed by the C-terminal residues of the monomers. Hyperactivity of the point mutant is correlated with both sterical and electrostatic factors, while inactivity of the deletion mutant is related to a loss of specific salt-bridge patterns between C- and N-terminus at the constriction and to the consequences for ion passage barriers, as revealed by integral equation theory. The cytosolic gate, however, is probably formed by the N-terminal segment up to the proline kink and not by the constriction. The results are compared with design principles found for other channels.

Introduction

Kcv, a viral potassium channel from the *Paramecium bursaria* chlorella virus (PBCV-1), represents the shortest sequence of a functional channel known to date (1). As a minimal working

model this K⁺ channel protein can be considered close to being prototypical in order to understand basic channel design principles and to gain insight into fundamental transport mechanisms (2,3). With a monomer length of only 94 amino acids this protein comprises basically just the pore region of all K⁺ channels. Kcv exhibits high topological similarity with other channels, including the selectivity filter signature sequence TXXTXGY/FG (4), a pore helix, and two transmembrane domains (TM1/TM2). These most likely correspond to outer domain TM1 and inner, cavity-forming domain TM2. Kcv is characterized by a short C-terminal TM2 inner helix and the absence of downstream cytosolic domains as well as an extraordinarily short N-terminus upstream of TM1. Homology modeling based on the crystal structure of the bacterial KirBac1.1 channel (5) indicates that the N-terminal part is equivalent to the "slide" helix. In both channels this domain is connected with a kink-forming proline to TM1 (6).

Despite the short sequence Kcv shares many functional characteristics with longer channels, including sensitivity to common K⁺ channel blockers and the ability to exhibit voltage-dependent gating. The question therefore arises as to the location and function of the gate(s) in the Kcv system in comparison with other K⁺ channels. This will allow insight into the generality of gating mechanisms. Currently there is evidence for two gates in K⁺ channels: many experimental and computational studies on channels with known crystal structures support the presence of a hydrophobic gate at the tight cytoplasmic constriction formed by the TM2 helix bundles, see e.g. (7,8,9,10,11,12,13,14). There is also strong evidence for the selectivity filter directly acting as a gate (14,15,16,17). The situation is most likely far more complex as suggested by the presence of couplings between the intracellular and extracellular gates (18): there is evidence as to the existence of open yet inactive pore states involving both gates. In contrast, recent computational work using elastic network models does not reveal such coupling (19). Instead, local concerted motion of both transmembrane segments associated with inner gate opening/closing transitions is apparently uncorrelated with the selectivity filter dynamics. This is found as a common scheme among known K⁺ channel structures. It is, however, questionable whether a purely harmonic network model would reveal such a cooperative behavior.

In this context, a further interesting feature of the small Kcv structure is that channel gating is influenced by structural elements far away from either the potential selectivity filter gate or the cytoplasmic end of TM2. A comparison of Kcv with orthologs from other chlorovirus isolates has shown that an amino acid exchange in the outer transmembrane domain (TM1) is sufficient to inverse the voltage dependence of the channel; a mutation V19F within TM1 of the Kcv channel from virus MA-1D shifts the channel from a mild inward rectifier into an outward rectifier (6). These features cannot be explained based upon structural features alone.

Although the C-termini in Kcv are presumably too short to exhibit bundle crossing as a signature for the inner gate found in other channels, the cytosolic side adjacent to the intracellular mouth is yet involved in Kcv gating. This has been demonstrated by electrophysiological experiments on mutants: replacing Pro13 by alanine (KcvP13A) in the N-terminus yields a hyperactive channel, which is characterized by a gain of a time and voltage dependent component (20). A possible explanation considers that the increased hydrophobic length of TM1 in KcvP13A

leads to a change of helix orientation in the lipid environment which, as a consequence, could affect gating. Complete truncation of the "slide helix" in Kcv results in channel inactivation (21). Progressive truncation of the N-terminus revealed that inactivation occurs if nine or more amino acids are removed (Kcv Δ N9). Very weak activity is found for Kcv Δ N8, whereas longer slide helices preserve channel functionality (22). In the context of the aforementioned model on the orientation of TM1 the latter data were interpreted in such a way that the cytoplasmic N-terminus requires a sufficient length for anchoring and positioning of TM1 in the membrane. This hypothesis requires further microscopic scrutiny.

Insight into structural, thermodynamic, and dynamical features of the intracellular mouth region of Kcv wild-type and mutants on the atomic level would therefore mean a major step forward in testing current hypotheses of mechanistic generality of gating transitions in K⁺ channels. The crystal structure of Kcv is, however, not known up till now, so all structure-function relationships established so far were based on multiple alignment and homology models. In this work, we used molecular dynamics (MD) simulations of model channels in a fully solvated lipid environment as a basic tool for generating structural and dynamical data in order to understand the wild-type structure of Kcv and the effects of mutations. Atomistic MD simulation is a well established computational tool in the area of potassium channel studies, see e.g. (10,11,14,23,24,25,26,27,28). These are typically based upon the experimental crystal structures of the target proteins, although many examples of successful simulations of homology models have been described in the literature, see, e.g., (29,30,31,32). As an alternative, one can directly study analogous model systems with known crystal structure that share essential sequence motifs with the target protein. In this case the simulation will be more stable and the resulting ensemble averages more reliable; the results are to a lesser degree confounded by uncertainties about the underlying structure as compared to pure homology models. The results can be interpreted under the hypothesis of functional analogy between model and target system. Since the sequence similarity of Kcv with other structurally known channels is quite low, we decided to proceed with such an approach at the present stage: the KirBac1.1 structure was truncated to match the shorter Kcv protein variants described above. KirBac1.1 was chosen because it contains the pivotal proline residue forming the onset of the slide helix in analogy with Kcv. Furthermore, mutations were inserted at equivalent positions to mimic the experimental alterations in Kcv. The resulting chimeras are termed KB-KcvWT, KB-KcvP13A, and KB-Kcv Δ N8. KB-Kcv Δ N8 shares with the totally inactive Kcv Δ N9 the feature that all positively charged amino acids in the N-terminus (arginine in Kcv vs. corresponding lysine in KirBac1.1) are deleted, which will be of special importance.

In addition to the biological questions we were particularly interested in the application of methods commonly employed in structural biology to our simulation results. These include interpretation of local structural features, motifs, and sterical permeation constraints as well as the use of Poisson-Boltzmann (PB) theory for characterizing the electrostatic ion passage free energy surface (33). To this end a substantial part of the present work was devoted to the development of a novel annealing procedure for extracting average all-atom structures from very long trajectories.

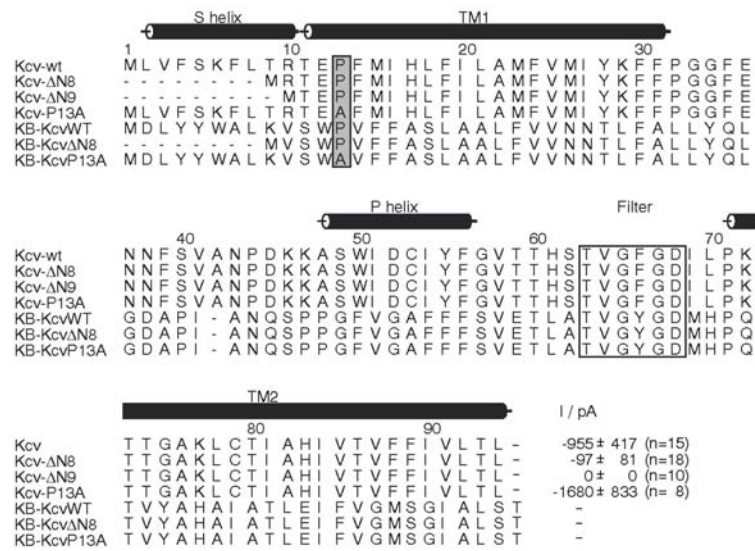


Figure 2.1: Sequence and secondary structure of KcvWT and mutants with their KirBac1.1 analogs. The filter and the position of Pro13 are marked by boxes (abbreviations: "s" = "slide", "p" = "pore", "TM" = "transmembrane domain"). The mean steady state currents of HEK293 cells expressing a chimera of KcvWT or mutant channels were measured as in (6) at -160 mV; the currents exceeding the mean current of mock transfected cells are given (20,22).

The tetrameric symmetry is fully taken into account making it possible to present the results of extensive MD simulations of the three model systems in a very compact way.

Furthermore, integral equation theory in the form of the three-dimensional reference interaction site model (3D-RISM) (34,35) was applied to the symmetrized structures, yielding insight into potassium density distributions around the tetrameric channels and into its spatial dependence on the mutation state. Large density at a given point in space is directly related to negative values of the potential of mean force accompanying single ion transport from the bulk to this region in the mean field of the environment. In the past, the site-averaging 1D-RISM theory has been applied to small fragments of the KcsA filter region (36,37). To the best of our knowledge, this is the first time that 3D-RISM theory has been used for characterizing the ion free energy surface of a full-size potassium-selective channel.

Methods

Modeling Wild-Type and Mutants: Among the available X-ray structures of K^+ channels (KcsA (38), MthK (39), KvAP (40), KirBac1.1 (5), Kv1.2 (41), and, discovered only after we started with the present work, NaK (42)) we chose KirBac1.1 (PDB code 1P7B) as the prototype systems for building Kcv-analog channel models because of the pivotal proline position that marks the start of the KirBac1.1 slide helix corresponding to Pro13 in Kcv. Sequence alignment in order to localize a suitable C-terminal truncation of the KirBac1.1 sequence has been performed along the lines of

our earlier work (6), taking into account suggestion given in (43). The final alignment is shown in Figure 2.1.

Atomic models of wild-type (KB-KcvWT) and deletion mutant (KB-Kcv Δ N8) chimeras were produced with the academic version of CHARMM V3b1 (44). For KB-KcvWT and KB-Kcv Δ N8 residues 1-49 and 1-57, respectively, as well as 142-309 were removed, leaving proteins of 94 and 86 amino acids per subunit. In all cases the resulting N-terminal residue was mutated into methionine. For the point mutant analogue (KB-KcvP13A), the expected change of local fold geometry due to replacing the kink-forming proline by alanine was taken into account by using Modeller V8.1 (45) in order to anneal into an optimal structure. The optimization in the field of knowledge-based potential derived from crystal structure statistics satisfies additionally spatial restraints of the template structure KB-KcvWT. In order to prevent both, distortion of the sensitive filter region and displacement of the K⁺ ions provided by the crystal structure, those positions were rigidly constrained during the annealing process.

Finally, hydrogen atoms were attached using CHARMM's "HBUILD" facility, followed by all-atom energy minimization by steepest descent and Newton-Raphson methods. The wild-type analogue coordinates were shifted with respect to the center of mass, the mutants were superimposed onto this structure in order to maintain comparable conditions for subsequent membrane insertion. Titratable residues were kept at their standard protonation state. The C-terminal threonines were deprotonated, the N-terminal methionines were protonated. Some discussion in the literature concerns the protonation state of Glu106 in KirBac1.1 that corresponds to Glu71 in KcsA and Glu58 in our wild-type chimera (16,46). In our model we decided not to bias the simulation towards a specific template K⁺ channel structure, so glutamate was kept in its deprotonated standard state during simulations. We have checked the influence of the protonation state on the electrostatic free energy surface in the central cavity (see below).

Molecular Dynamics Simulations: All simulations were performed with the NAMD 2.5 molecular dynamics program (47) using all-atom potential energy functions CHARMM22 for proteins (48) and CHARMM27 for phospholipids (49). The TIP3P water model (50) and KCl as electrolyte were used. Lennard-Jones parameters of the ions were $\epsilon = 0.087/0.15$ kcal mol⁻¹ and $R_{\min}/2 = 1.76375/2.27$ Å for K⁺/Cl⁻ (51). Bonds between heavy atoms and hydrogen were kept fixed using the SHAKE algorithm (52). Throughout, a time step of 2 fs was applied, Lennard-Jones interactions were switched smoothly to zero over a distance between 10–12 Å, electrostatics were treated by the particle mesh Ewald algorithm (53) with a Fourier grid of 72 x 72 x 96 points corresponding to ca. 1 Å resolution. Constant temperature conditions were realized at 330 K by a Langevin thermostat (coupling constant 5 ps⁻¹, not applied to hydrogen), constant pressure was set to 1 atm by applying the Langevin piston algorithm (54,55) with an oscillation period of 200 fs and damping time scale of 100 fs.

The complete simulation system composed of tetrameric protein, lipid, and aqueous KCl solution was assembled following closely the protocol developed and provided by Roux and

coworkers (24,51,56). In short, first a protein-membrane system is built and minimized using a set of pre-equilibrated lipid molecules, in parallel a water box is equilibrated; second the two subsystems are merged, minimized, and pre-equilibrated followed by insertion of ions satisfying a given average concentration and overall charge neutrality.

In our special case the distance between the terminal residues of the longest transmembrane domain TM1 along the z axis (the membrane normal) is around 34 Å. Thus DMPC has been chosen to build the bilayer since the thickness of a DMPC bilayer is of similar dimensions. For every model the cross-sectional area in the xy plane was calculated. The maximum area occupied by the protein models was determined for either of the monolayers and subtracted from the box area. According to the discussion in (24), a cross-sectional area of 59 Å² per DMPC molecule was assumed to be a reasonable value. The approximate number of lipid molecules required for either side was calculated. This number was used as a starting point and adapted where necessary to the specific needs of every system. Several values were tested in a number of attempts by short MD runs. Using too many lipid molecules stalls the building procedure whereas too few lipids would allow too many water molecules to penetrate the membrane. Stable results were obtained for 62/68/69 DMPC molecules on the intracellular side and 54 throughout on the extracellular side for KB-KcvWT/KB-KcvΔN8/KB-KcvP13A, respectively. The total number of atoms was 48561/48869/49026 at a concentration of ca. 100 mM KCl. Thus, all systems contained 33 potassium, 17 chloride ions, and 9701/9765/9586 water molecules, respectively. The initial dimensions of the orthorombic simulation cell were 92 Å along the z axis and 72 Å along in the xy plane.

In addition to the harmonic restraints that were gradually removed during the building procedure, we applied strong restraints (force constant 10 kcal mol⁻¹ Å⁻²) to the filter residues (TVGYGD) and to the K⁺ ions in the filter to prevent distortion of this sensitive region during all of equilibration and most of the production time. Only at the end of the construction, a very short restraint-free *NpT* run of 20 ps was performed in order to allow the filter region to accommodate before re-restraining. According to the electrolyte concentration we have placed two restrained K⁺ ions on binding positions S1 and S3 using the terminology defined in (26) and two restrained water molecules on S0 and S2 in the filter. In total, trajectories of 45 ns were produced for each model. Filter restraint were applied during the first 30 ns and lifted for the remaining 15 ns in order to probe stability. For the structural averaging procedure to be described below only the last 21 ns of the rigid filter runs were used. Trajectory data was stored every 1 ps.

Symmetrizing Structural Averaging by Simulated Annealing: One of our main goals for assessing differences between wild-type and mutants was to condense the information of very long trajectories into meaningful all-atom average structures. Simple averages are unsuitable over longer times since for instance rotatable groups could collapse into single sites and cause a loss of backbone integrity. The key idea realized in this work was to use average distances measured over the trajectories as target values for a simulated annealing procedure on the isolated tetramer. This

is equivalent to minimization in the mean-field of the environment that is effectively encoded by the harmonic restraint distances. Rotational symmetry can additionally be imposed during annealing in order to allow for subsequent analysis of simulation data by computational means that have been applied in the past to crystal structures only.

The procedure is summarized as follows: (i) heavy atom distances are averaged over the production run taking into account topologically equivalent sites within the subunits. Inter-subunit distances are calculated and averaged separately for neighboring and opposite pairs. (ii) For defining restraints, all $C\alpha$ pair distances are considered; for all other heavy atom pairs only those within a target cutoff distance of 11 Å are taken into account. (iii) Restraint force constants of 10 kcal mol⁻¹ Å⁻² between $C\alpha$ - $C\alpha$ pairs and of 0.1 kcal mol⁻¹ Å⁻² for all others are assigned, weighted by the inverse fluctuation of the target distances measured in Å. (iv) Starting with the crystal structure-like initial models of the chimeras, the isolated tetrameric proteins are optimized first within the CHARMM force field augmented by the restraints (including heavy filter restraints with force constant of 1000 kcal mol⁻¹ Å⁻²) by 100 steps steepest descent and 50 steps adopted-basis Newton-Raphson minimization. (v) The global minimum of the model is approached by a symmetrizing simulated annealing procedure using Langevin dynamics with a friction constant of 10 ps⁻¹ and a time step of 1 fs within CHARMM.

The latter part is defined by a temperature schedule comprising the following steps: (va) starting with the temperature T_0 , T is kept constant over a period Δt . (vb) T is quenched linearly to $T_1 = T_0 - 200$ K over Δt . (vc) T is kept constant at T_1 over Δt , followed by symmetrization. (vd) T is increased instantaneously to $T_2 = T_1 + 100$ K. Steps (va)-(vd) are repeated by setting $T_0 := T_2$ and increasing Δt by a factor of 1.1 until a target temperature of 0 K or below is reached. In this case a final MD minimization at 0 K over Δt is performed. After step (vc) in each cycle, symmetrization is achieved by first computing average structures over the last constant temperature window and superposition of three monomers onto one with respect to filter atoms and hetero atoms, followed by averaging all topologically equivalent atoms and re-superposition of the resulting average monomer structure onto the original asymmetric tetramer of this cycle step.

Beside other parameters we have optimized independently and then kept fixed, two quantities influence the performance of the annealing protocol: initial temperature T_0 and interval Δt . We have tried a variety of combinations in the range 250 – 1500 K and 200 – 1000 fs. Best results in terms of minimal RMS (root mean square) deviations (RMSD) between target and optimized distances measured for the final models were obtained with $T_0 = 750$ K and $\Delta t = 200$ fs. This parameter set leads to total RMSDs of 0.458/0.423/0.587 Å for all restraint distances in KB-KcvWT/KB-KcvΔN8/KB-KcvP13A, respectively and was used throughout in the following. The RMSD of all $C\alpha$ pairs in the rigid filter simulation of wild-type and mutants is additionally depicted in the top part of Figure 2.2, emphasizing the performance of the approach.

Structural and Thermodynamic Evaluation: Besides standard techniques for evaluating simulation results like the computation of RMS fluctuations (RMSF) and RMS deviations of the structures as

they evolve from the initial state, we also used HOLE analysis (57) for analyzing the pore diameter, Poisson-Boltzmann theory (58) for accessing the electrostatic free energy surface of K^+ entering the channel from the bulk solution, as well as 3D-RISM integral equation theory (34,35) for a realistic view on potassium density distributions. The RMSD calculations were carried out with the RMSDTT v1.9.2.2 plugin (59) for VMD v1.8.3 (60). HOLE, PB, and 3D-RISM analysis were applied to the symmetrized average structures. Averaging procedures like the one described above are dangerous if gating events in the form of global conformational changes had occurred during the simulation time scale. These are inaccessible to unbiased MD simulation with present-day resources and did not happen in our models. As we will show below, our simulation model corresponds to the open state of the channel, warranting the evaluation of averaged structures.

When interpreting purely structural information one must, however, not over-interpret rigid structure results since sterical barriers may disappear easily due to short-scale dynamics (33). In contrast, electrostatic fields are of wider range, vary less steeply, and are less sensitive to short-scale dynamics. Both measures together yield a sensible picture of barriers and de-/stabilizing forces accompanying ion transport between bulk solvent and the channel pore. The integral equation approach covers basically both components within a single methodology. Though the theory is approximate, the underlying molecular models of solute (the channel) and solvent (aqueous KCl solution) are identical with those used in the simulations. In this way, we are able to characterize the scenario in a much more realistic way, beyond the capabilities of more simplified HOLE and PB approaches, but with comparable computational effort.

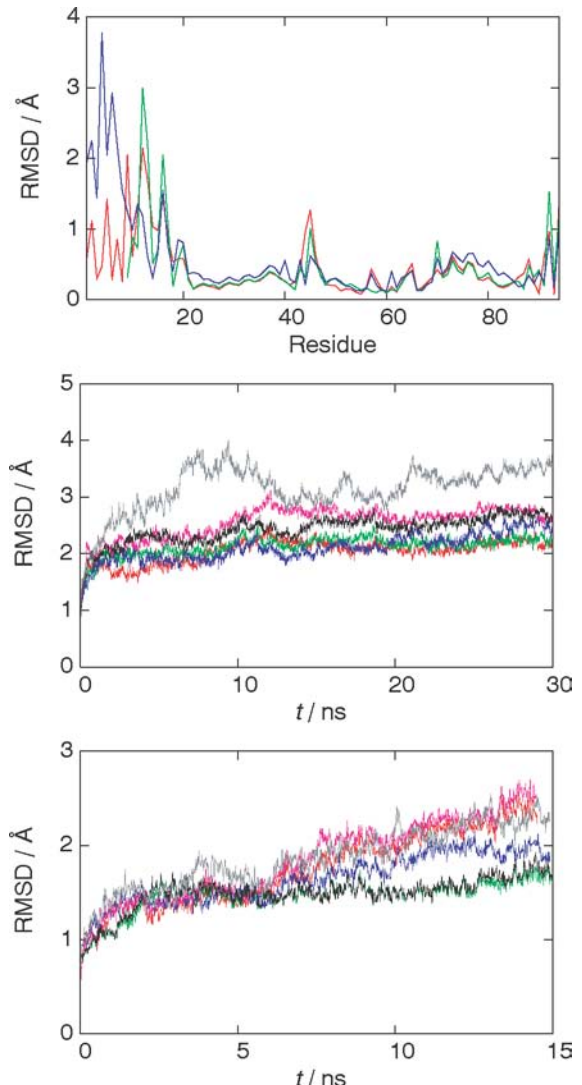


Figure 2.2: RMS deviation between globally optimized and target backbone $\text{C}\alpha$ pair distances obtained from the symmetrizing simulated annealing procedure (top); backbone RMSD time series of the structures: rigid filter runs (middle) and subsequent fully relaxed simulations (bottom, time was reset to zero). Red/magenta (excluding N-terminus/full protein): KB-KcvWT, black/green: KB-Kcv Δ N8, gray/blue: KB-KcvP13A.

Our PB treatment for a given channel geometry follows closely the procedures outlined earlier by Roux and co-workers (33), particularly Ref. (61). As a result we obtain the electrostatic free energy change accompanying K^+ transport from the bulk to a point in the pore along the reaction coordinate defined to be the z axis connecting the filter ions and the center of the cavity which is set to $z = 0$. The membrane is described as planar slab with a height of 25 Å. The interior of the protein is confined by the van-der-Waals radii of its atoms (62) using a probe radius of 1.4 Å. A cylinder with radius 12 Å representing the solvent-filled pore was cut out from the membrane slab. The relative dielectric constant of the aqueous solution and the cylinder was set to 80 whereas a value of 2 was assigned to the hydrocarbon core of the membrane as well as to the protein interior. PB calculations with the built-in PBEQ module (63) of CHARMM were performed in two stages, first with a cubic grid of 140^3 points and an initial grid spacing of 1 Å, and afterwards focusing around the main region with half of the grid spacing. Periodic boundary conditions were applied in the membrane xy plane. The two K^+ ions in the filter were kept fixed while a third K^+ was placed in intervals of 0.5 Å along the reaction coordinate for computing the transfer free energy under varying ionic strength conditions.

The solution to 3D-RISM theory requires two steps: firstly, the determination of the pure solvent susceptibility, and, secondly, the computation of the 3D density distribution of the respective solvent around the channel. In this second stage the fully solvated tetrameric protein only was taken into account, excluding the membrane. The KCl/TIP3P susceptibility was determined by solving the dielectrically consistent 1D-RISM equations (64,65) on a logarithmically spaced grid of 512 points ranging from $5.98 \cdot 10^{-3}$ Å to 164.02 Å using a variant of the modified inversion of iterative subspace (MDIIS) method (66). Small Lennard-Jones parameters ($\sigma_H = 0.4$ Å, $\epsilon_H = 0.046$ kcal mol⁻¹) were attributed to the hydrogen sites of TIP3P in order to avoid numerical singularities. Temperature was set to 298.15 K, electrolyte concentration to 1 M corresponding to number densities for water of 0.032367 Å⁻¹ and for KCl of 0.000602 Å⁻¹ (67). The relative dielectric constant of the solvent was taken as 68.5 (68). The 3D-RISM equations were solved within the partially linearized Kovalenko-Hirata (KH) closure approximation (69) on a cubic grid of 128x128x128 points with a 0.6 Å spacing by the MDIIS technique (66). Long-range electrostatics was treated by Ewald summation (69), taking into account conducting boundary conditions. No fixed potassium sites were present; the protonation states of the proteins were identical with the MD simulations models. All integral equation computations were performed using a computer code developed in our laboratory. The density distributions were visualized by the MOLCAD program (70).

Results

Phenomenology of the Simulations: Besides monitoring total energy, density profiles, etc. which all indicated progress toward equilibrium which is practically reached with respect to these observables after a few ns, we report here only results of the backbone RMSD as a measure of structural drift from the initial models (see Figure 2.2, middle and bottom part). While the

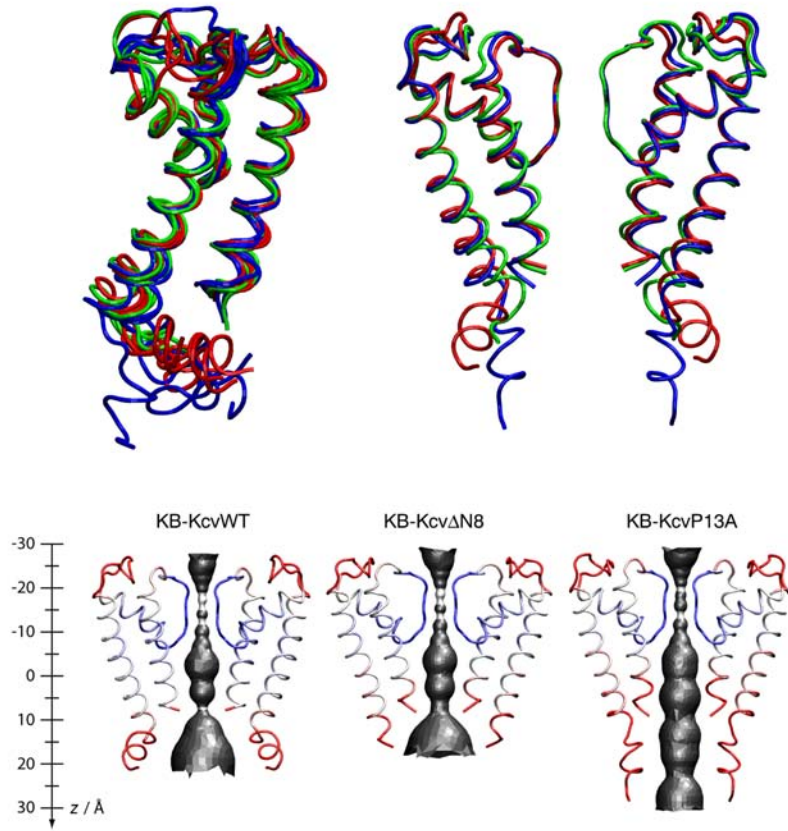


Figure 2.3: Superposed backbone structures from simple averaging over the final 7.6 ns of the rigid filter runs (top, left); superposition of structures from the symmetrizing simulated annealing procedure (top, right; only two subunits are shown for clarity); red: KB-KcvWT, green: KB-Kcv Δ N8, blue: KB-KcvP13A. HOLE analysis and backbone atomic *B* factors (blue: $< 10 \text{ \AA}^2$, red: $> 20 \text{ \AA}^2$), mapped onto symmetrized structures (bottom).

simulations with rigid filter restraints ("rigid filter simulations") appear fairly stable, relaxing the filter has a strong effect, as expected (16,71): ions move rapidly into another configuration, from S1/S3 to S2/S3 in the terminology defined in (26), which in turn leads to substantial filter distortion; this progressively extends to other regions of the protein. We consequently used for long-time structural averaging only the rigid filter runs. This is justified because of the apparent low mobility of the filter and the locality of associated transitions (19,72). By dissecting the RMSD further into the N-terminal slide helix and into other regions' contributions, it becomes clear that particularly the N-terminus undergoes larger amplitude motion, as shown in Figure 2.2, middle and bottom: While the RMSD time series appears reasonably stable for the backbone atoms excluding the slide helix, somewhat stronger deviations are observed for the full sequence. The flexibility is also reflected in Figure 2.2, top in terms of the RMSD values obtained for the symmetrized structures, which are largest in the N-terminal part.

Simple structural averages over the last 7.6 ns of the rigid filter simulations are shown in the upper part of Figure 2.3. The most relevant structural features are the following:

(a) It is evident from the comparative structures that the P13A mutant has a TM1 segment which is much more flexible than in the two other channels. This leads to an increased asymmetry among the monomers within the tetramer. The effect of the mutation on TM1 flexibility is, however, rather local and mostly confined to the inner mouth of the channel. All models agree structurally quite well for any region except the slide helices. The same statement holds for the fully relaxed simulation results, so we do not suffer from artifacts related to the rigid filter geometry.

(b) The slide helix attached to TM1 does not exhibit significant contact with the surrounding membrane head groups. This is in marked contrast to recent computational results concerning the KirBac1.1 gating mechanism (73) where it was shown that varying contact patterns between aromatic residues in the slide helix and the lipid phase accompany the gating transition.

(c) In line with our earlier results (6), TM2 is too short to exhibit bundle crossing in order to realize the canonical closed state of the channel. Furthermore, in contrast to earlier observations concerning the gating mechanisms of known channel structures (11) we cannot identify any significant change of TM2 upon mutation or during the simulations. This suggests that the measured stochastic opening and closing (74) as well as the differences in channel activity between WT and mutant Kcv channels is not caused by motion of the inner TM domain.

(d) The simulations revealed the presence of four stable intra-monomer K^+ binding sites, located between Glu58 and Asp67 in each monomer (numbering according to Figure 2.1, note the alignment gap in the KirBac1.1 sequence near position 41). This complements the discussion about the protonation state of the respective glutamate (see above in subsection "Modeling wild-type and mutants") since apparently a positive charge (being either a proton or a K^+ ion) is required at this position.

While the structural observations already suggest that the cytosolic side of the pore is open, we also have dynamical support for this view. We have observed spontaneous ion transitions from the bulk into the central cavity, although we constructed the cavity initially to be ion-free. To the best of our knowledge this is the first observation of this kind of dynamics (see Figure 2.4). Over the whole of the trajectories (constrained and unconstrained), KB-KcvWT behaves markedly different as compared to the mutants: almost immediately after the start of the simulations a first K^+ ion entered the cavity and stayed at a position close to the filter. Other ions frequently entered and exited; on average two ions occupied the cavity. Ion transport through the intracellular mouth is accompanied by coordination and subsequent release by the C-terminal carboxyl groups. In the case of the P13A mutant the cavity appears to be less favorable for cation stabilization: only after the filter restraints had been lifted, a single ion moved into the cavity. For KB-Kcv Δ N8 we observed a similar stabilization for the first ion that passed the mouth and immediately moved close to the filter. A second one, however, got expelled after some time, whereas another cation got basically trapped between the C-terminal carboxyl groups by tight coordination after 300 ps simulation time. This state remained stable over the rest of the trajectory, blocking further ion entrance or exit. We have therefore the first indication that the deletion mutant forms an open yet

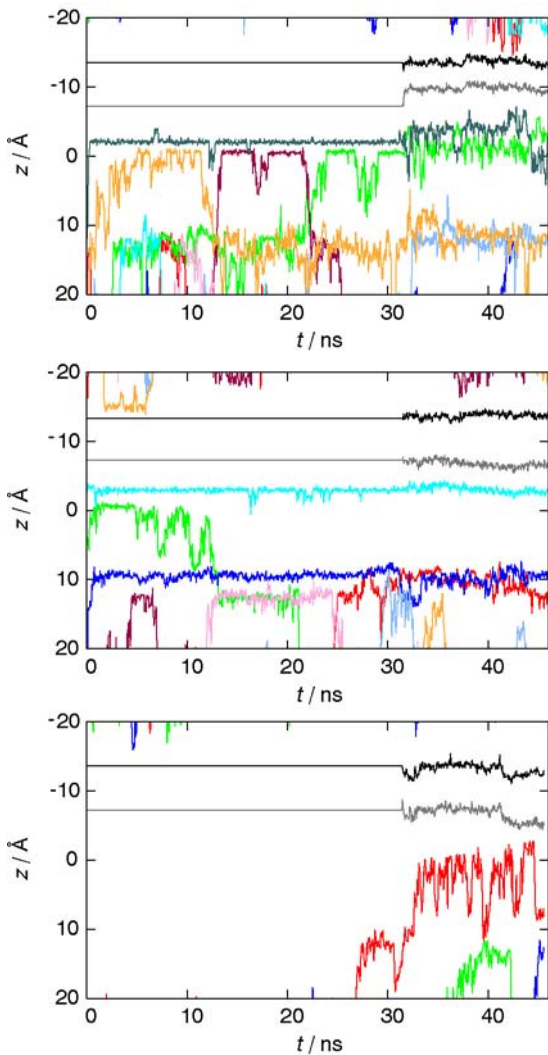


Figure 2.4: z coordinates (along the channel axis corresponding to Figure 3) of potassium ions entering and exiting the cavity from the intracellular side (top: KB-KcvWT, middle: KB-Kcv Δ N8, bottom: KB-KcvP13A).

helix/membrane contacts; the orientation of TM1 in the membrane is not significantly affected. Overall, we see confirmation for the highly localized effect of the mutations at the inner part of the protein. The increased N-terminal flexibility has a counterpart in the corresponding C-termini in KB-KcvP13A. Quite evidently, the inner constriction (defined as the smallest diameter found by HOLE analysis) is substantially enlarged in KB-KcvP13A; in contrast, wild-type and deletion mutant show only insignificant differences.

An interesting result of the present data is that TM2, despite of its short length, forms a constriction by the C-terminal amino acids. The diameter can become very small, comparable with the size of the K^+ ion. The estimated size of the inner constriction suggests that it could obstruct passage of ions. Nonetheless, the open character of the inner mouth and the local flexibility of

inactive pore state. Later on we will show that all dynamical features that have been observed correspond well with thermodynamic and structural observables in order to explain the differences in conductivity.

Symmetrized Average Structures: A more detailed picture of the effects of the mutations on structure/function correlates is obtained by analyzing the symmetrized average structures from the simulated annealing procedure. Figure 2.3 depicts in the upper right part the superposition of the resulting structures of the three variants onto each other and in the lower part the geometries together with color-coded local backbone atomic B factors computed over the final 4.5 ns of rigid filter production runs, and accessible free volume from HOLE analysis. In this representation the effect of the P13A mutation becomes more clearly visible: there is a tendency toward helix elongation of TM1 caused by removing the kink-forming proline; this is in line with earlier results (6). But unlike speculated earlier (6) this helix elongation does not lead to more pronounced

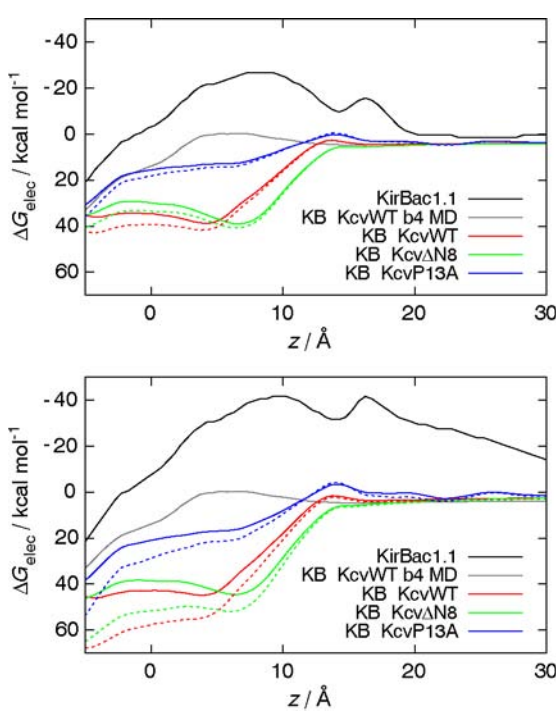


Figure 2.5: Electrostatic transfer free energy profile for K^+ along the channel z axis (red: KB-KcvWT, green: KB-Kcv Δ N8, blue: KB-KcvP13A, black: original KirBac1.1/PDB code 1P7B, grey: truncated KirBac1.1 corresponding to the initial KB-KcvWT model before simulation). Solid lines: protonated Glu58 (wild-type, corresponding to Glu106 in KirBac1.1), dashed: deprotonated Glu58. Top: Ionic strength 100 mM, bottom: 0.

with our findings for KB-KcvP13A: the barrier to inward current (i.e. from the cavity into the cytosol) in the mutant decreases in comparison to KB-KcvWT. In the Kcv reference system this corresponds to a measurable increase of inward current (6). Interestingly, the electrostatic free energy surface of the deletion mutant does not exhibit substantial differences compared to the wild-type. Worth noting is that changing the protonation state of Glu58 does not alter the relative trends rendering this position uncritical, neither does increasing the ionic strength from a situation without ionic screening to 100 mM. So from both, a sterical and an electrostatic perspective all three channels produce an open, conductive conformation; however the P13A mutant results in an even higher conductance state compared to wild-type and deletion mutant. The latter two do not differ much in their sterical and electrostatic properties. It is therefore reasonable to attribute the experimentally measured larger stationary currents in the KcvP13A channel to both sterical and electrostatic factors. The small activity/total inactivity of Kcv Δ N8/9 on the other hand must have a different origin.

TM2 preclude the assumption that this hydrophilic constriction is identical with the inner gate in this channel.

The global situation around the N-terminal constriction becomes clearer when we take results from Poisson-Boltzmann theory into account. Figure 2.5 shows free energy data for the three variants with two different protonation states of Glu58. Also included are the curves for the initial wild-type model (a truncated KirBac1.1 pore) before simulation as well as for the native KirBac1.1 geometry from X-ray crystallography, both for an ionic strength of 0 and 100 mM. Comparison of native and truncated KirBac1.1 reveals that mere truncation already has drastic effect on the free energy surface, making the cavity overall favorable for cation binding. Accordingly, the electrostatic barriers to K^+ entry from the cytosol are very small for all our chimeras, indicating again the open state for any variant under scrutiny. In line with findings for other channels (61), less favorable transfer free energy within the cavity corresponds to a higher conductance state. This is indeed consistent

Salt Bridge Patterns: A remarkable result is found in the context of the structure around the inner mouth which emphasizes the importance of the symmetrizing annealing approach: Figure 2.6 shows the average configuration of positive residues in the N-terminal slide helix, i.e. Lys9 (WT/P13A) and the terminal methionine, and negative C-terminal Thr94. The C-terminal carboxyl function forms a salt bridge with Lys9 predominantly within the same monomer in the wild-type case, and predominantly between neighboring monomers in KB-KcvP13A. For KB-Kcv Δ N8 no such positively charged partner for the C-terminal threonine is permanently available, giving rise to a change of local permeability of the inner mouth constriction. In the reference system, the totally inactive Kcv Δ N9, an equivalent positively charged arginine is lost.

These features are not an artifact of the annealing procedure, but are also directly reflected by the dynamics, as illustrated with distance time series over the entire rigid filter runs in Figure 2.7: The data show that a salt bridge is formed if the distance between amino N and carboxyl C locks in below 5 Å. Such states are frequently observed for wild-type and P13A mutant between Lys9 and Thr94. The other available positive residue, N-terminal methionine, temporarily locks into a salt bridge configuration with threonine in the cases of P13A and Δ N8, but not so in the case of the wild-type channel. We observe frequent flips between intra- and inter-monomer configurations for P13A, and also, to a lesser extent, for the wild-type. In the deletion mutant the Thr94 carboxyl group is free to find other partners, such as strongly coordinating K⁺ ions. Such a configuration blocks the passage of further ions through the constriction. This feature corresponds with the finding that the electrostatic barrier at the constriction is smallest for KB-Kcv Δ N8 among the variants, indicating local net stabilization for K⁺ relative to the other mutants. The presence of GFP attached to the C-terminus of channels studied in the corresponding electrophysiological experiments does not disqualify the interpretation suggested here since the linker (sequence EFCSSRYRGPGIHRPVAT) contains a negative group just as the first residue attached to threonine. The present salt bridges in the vicinity of the inner mouth constriction are not unique to KB-Kcv, but have an analogy in the recently resolved X-ray structure of the NaK channel (42): structural analysis reveals such motifs between different subunits (Glu23 near the slide helix kink and Arg10 in the N-terminal slide helix) as well as within the same monomer (Glu23 and Lys97 in the C-terminal region). It will certainly be fruitful to study other channels in order to characterize the general role of similar salt bridges in structure function relationships of ion channels.

The similarity between KB-KcvWT and KB-Kcv Δ N8 leaves only the change in salt bridge patterns and the resulting potassium block as a reasonable explanation for the apparent inactivity of the Kcv reference system. Apparently, the transport mechanism through the constriction is characterized by a delicate balance between cation coordination and salt bridge flipping. This mechanism is similar for wild-type and point mutant, and is disrupted for the deletion mutant due to missing salt bridges. Therefore, the presence of positively charged residues in the N-terminus appears to be a design principle for Kcv-type - and probably other - channels. It is tempting to speculate that the inner constriction resembles a "turnstile" which, together with the cavity,

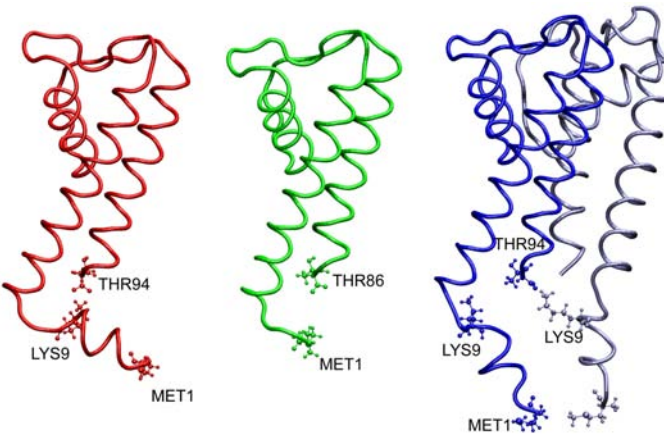


Figure 2.6: Salt bridge patterns observed in symmetrized average structures (red: KB-KcvWT, green: KB-Kcv Δ N8, blue: KB-KcvP13A).

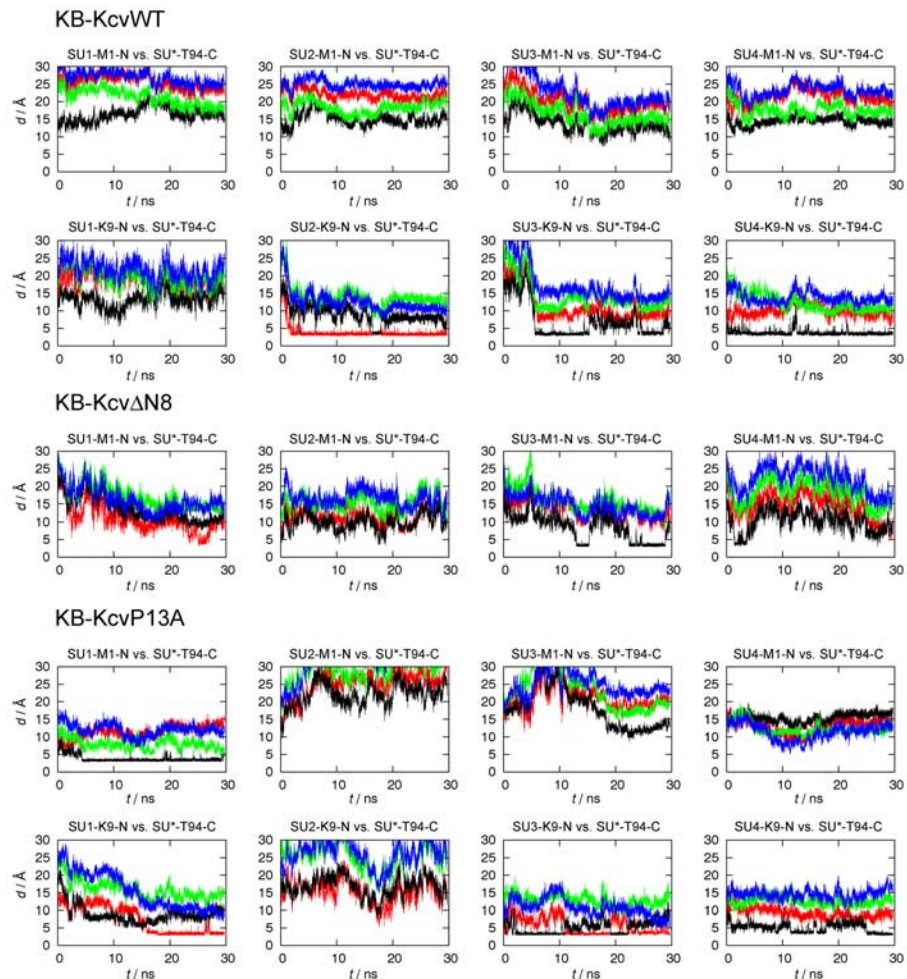


Figure 2.7: Salt bridge constituent time series for distances between amino N of positive residues and carboxyl C. The header of each plot encodes the residue index for the respective atoms (example: SU1-K9-N = SubUnit1, residue Lys9, amino Nitrogen). Every plot shows the evolution for a specific atom versus its counterpart in all four subunits (indicated by the wildcard SU*). Black: atoms belong to the same monomer; colored: atoms belong to different monomers.

functions as a local buffer device that guarantees an almost constant flux of ions under varying local concentrations near the membrane-cytosol interface.

The similarity of KB-KcvWT and KB-KcvP13A is equally remarkable since it offers the basis for the localization of the presumed inner gate in Kcv-type channels: the higher conductance character of P13A in the open inner-mouth state is adequately explained by sterical and electrostatic factors. Therefore, the different gating kinetics, if they are related to an inner gate, must be caused by the N-terminal sequence up to the kink at Pro13. The N-terminus itself probably represents a gate. We cannot rule out the possibility that the effect of mutations is transmitted to the filter region. However, a simple vibrational coupling mechanism appears to be unlikely (19), and we have not found any other dynamical evidence.

Integral Equation Theory: The results from 3D-RISM theory illustrate and summarize the preceding discussions in a compact way. They furthermore elucidate the origin of the apparent potassium blockage found for the deletion mutant. Potassium densities around the fully solvated channel proteins are shown in Figure 2.8. The extracellular side of the filter is characterized by large high density regions which correspond to extended funnel-like free energy basins responsible for pulling bulk potassium into the filter region. This motif is, as expected, found for all variants. Integral equation theory is capable of locating the distinct K^+ filter positions as well as the K^+ binding sites between Glu58 and Asp67 in each monomer. Large density is also found within the cavities of wild-type and deletion mutant, and, to slightly lesser extent particularly near the mouth, in the P13A variant. All these data agree quite well with the sterical/electrostatic picture developed above.

RISM theory, in contrast to Poisson-Boltzmann analysis, allows a deeper view into the consequences of missing salt bridges: KB-Kcv Δ N8 shows a substantial increase of potassium density right behind the constriction on the cytosolic side which has no analogy in the other variants. This free energy basin is the thermodynamic origin of the tight K^+ coordination leading to substantial escape barriers that are not found by purely electrostatic approaches. In contrast to the filter region where large barriers are effectively reduced by concerted single-file motion, such a mechanism appears to be impossible if only a single coordination partner like the C-terminal carboxyl function is present.

The integral equation approach is obviously quite powerful for characterizing the single-ion free energy surface of channels. On the other hand, the results indicate that our simulation time was indeed long enough to sample essential properties of the variants: Most dynamical features detected by direct inspection of the trajectories can be related to the density distributions. It will certainly be fruitful to use this technique for further ion channel studies.

Discussion

Based upon the hypothesis of structural and functional analogy between Kcv mutants and our three KirBac1.1 mutant models, our results allow the identification of key features of the channel protein that characterize the role of the N-terminus for channel function:

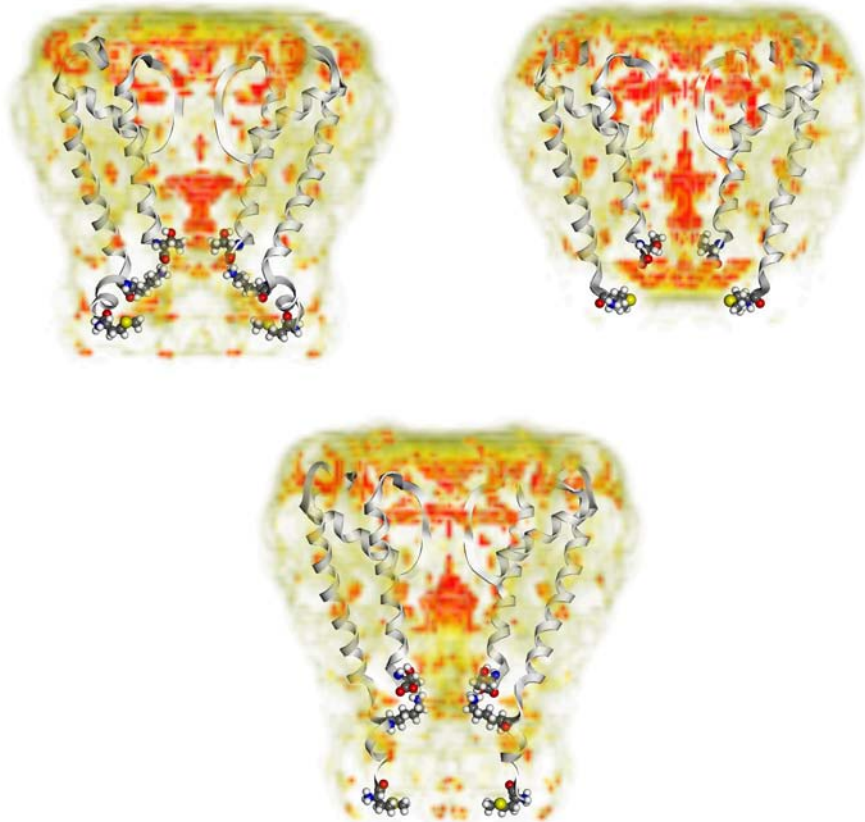


Figure 2.8: Color-coded potassium density distribution from 3D-RISM-KH theory around fully solvated WT and mutant channel structures in 1 M KCl solution (top: KB-KcvWT, middle: KB-Kcv Δ N8, bottom: KB-KcvP13A). Density increases from transparent (bulk value and below) over grey and yellow to red. C- and N-terminal amino acids as well as Lys9 are explicitly depicted.

(a) The effect of mutations is highly localized. Although this may be related to the fixed filter geometry applied in the production simulations, the procedure is justified by the results of the network model analysis by Shrivastava and Bahar (19) and by inspection of fully relaxed simulations. All observables agree with the assumption that the cytoplasmic side of the channel is open in the present simulations, regardless of the effect of any mutation, as evidenced by spontaneous ion transition events into the cavity from the cytosolic side. Structurally and energetically, the deletion mutant is equally open, but appears to be in an inactivated state (see also (c)).

(b) The intracellular mouth is defined by a hydrophilic constriction formed by the C-terminal amino acids, in contrast to other known K^+ channel structures where the inner gate is characterized by a hydrophobic constriction via bundle crossing of transmembrane segments. The carboxyl functions flip frequently between an orientation towards the channel axis when an ion is actually passing the constriction, and a salt bridge with positively charged residues in the N-terminus, if available. Similar salt bridge patterns are observed in the recently resolved structure of the NaK channel (42). The inner constriction presumably operates like a "turnstile" guaranteeing an almost

constant ion flux in conjunction with the cavity.

(c) The function of the inner constriction, which is not the gate itself (see below), is directly related to the presence of these salt bridges. Deleting positive groups leads to channel inactivation. This is related to a change of the role of carboxyl groups that block the passage of further cations by coordinating tightly with a potassium ion in the absence of a salt bridge partner. Neither sterical nor purely electrostatic factors seem to be responsible for the apparent inactivation. Integral equation theory is capable of characterizing the situation fully. The presence of positively charged residues in the N-terminus appears to be a design principle for potassium channels characterized by short C-termini or by the presence of negative charges at relevant positions.

(d) We did not observe a significant change of the transmembrane domains with respect to their orientation or bending as a result of mutations. The N-terminal slide helices are very flexible and do not exhibit significant contact with the lipid environment.

(e) The localized effect of the N-terminal P13A mutation leads to both sterical and electrostatic factors favoring ion permeability into and out of the cavity. This is compatible with the observation that the analogous mutation causes an increase of steady-state current in Kcv (20). From the similarity between wild-type and P13A mutant in the constriction area we can conclude that the inner gate, if it exists, is not directly located at the region of smallest sterical pore diameter. On the other hand, as long as we accept the functional analogy between Kcv and the simulated chimeras, the different time-dependent current component of the P13A mutant can only be understood if the N-terminus itself acts as a cytosolic gate. Alternatively but unlikely the effect of mutations could be transmitted to the filter region.

In summary, Kcv possesses, compared to other known potassium channels, very genuine but also a number of certain common structural elements. The role of all these elements for the open pore state was partially understood in the present work. For a complete microscopic dynamical picture of channel function and gating kinetics, however, we need to understand the structure of the closed state, the cytosolic gating mechanism, its regulation and coupling to the filter gate from an atomic perspective. The "functional analogy" hypothesis needs further examination by cross-checking the results for KB-Kcv with simulations of atomistic Kcv models. Work into this direction is currently in progress.

Acknowledgement

Computer time was provided on IBM Regatta systems at the Hochschulrechenzentrum Darmstadt and at the Forschungszentrum Jülich. We thank J. Brickmann and the MOLCAD GmbH for providing the MOLCAD visualization program.

Reference

1. Plugge, B., S. Gazzarrini, M. Nelson, R. Cerana, J. L. Van Etten, C. Derst, D. DiFrancesco, A. Moroni, and G. Thiel. 2000. A potassium channel protein encoded by chlorella virus PBCV-1, *Science* 287: 1641-1644.
2. Gazzarrini, S., M. Severino, M. Lombardi, M. Morandi, D. DiFrancesco, J. L. Van Etten, G. Thiel,

-
- and A. Moroni. 2003. The viral potassium channel Kcv: structural and functional features. *FEBS Lett.* 552:12-16.
3. Kang, M., M. Graves, M. Mehmel, A. Moroni, S. Gazzarrini, G. Thiel, J. R. Gurnon, and J. L. Van Etten. 2004. Genetic diversity in chlorella viruses flanking Kcv, a gene that encodes a potassium ion channel protein. *Virology* 326:150-159.
 4. Heginbotham, L., T. Abramson, and R. MacKinnon. 1992. A functional connection between the pores of distantly related ion channels as revealed by mutant K⁺ channels. *Science*. 258:1152-1155.
 5. Kuo, A., J. M Gulbis, J. F. Antcliff, T. Rahman, E. D. Lowe, J. Zimmer, J. Cuthbertson, F. M. Ashcroft, T. Ezaki, and D. A. Doyle. 2003. Crystal structure of the potassium channel KirBac1.1 in the closed state. *Science*. 300:1922-1926.
 6. Gazzarrini, S., M. Kang, J. L. Van Etten, S. Tayefeh, S. M. Kast, D. DiFrancesco, G. Thiel, and A. Moroni. 2004. Long-distance interactions within the potassium channel pore are revealed by molecular diversity of viral proteins. *J. Biol. Chem.* 279:28443-28449.
 7. Doyle, D. A. 2004. Structural changes during ion channel gating. *Trends Neurosci.* 27:298-302.
 8. Doyle, D. A. 2004. Structural themes in ion channels. *Eur. Biophys. J.* 33:175-179.
 9. Perozo, E., D. M. Cortes, and L. G. Cuello. 1999. Structural rearrangements underlying K⁺-channel activation gating. *Science*. 285:73-78.
 10. Beckstein, O., P. C. Biggin, P. Bond, J. N. Bright, C. Domene, A. Grottesi, J. Holyoake, and M. S. P. Sansom. 2003. Ion channel gating: insights via molecular simulations. *FEBS Lett.* 555:85-90.
 11. Grottesi, A., C. Domene, B. Hall, and M. S. P. Sansom. 2005. Conformational dynamics of M2 helices in KirBac channels: Helix flexibility in relation to gating via molecular dynamics simulations. *Biochemistry*. 44:14586-14594.
 12. Kuo, A., C. Domene, L. N. Johnson, D. A. Doyle, and C. Venien-Bryan. 2005. Two different conformational states of the KirBac3.1 potassium channel revealed by electron crystallography. *Structure*. 13:1463-1472.
 13. Robertson, J. L., and B. Roux. 2005. One channel: open and closed. *Structure*. 13:1398-1400.
 14. Roux, B. 2005. Ion conduction and selectivity in K⁺ channels. *Annu. Rev. Biophys. Biomol. Struct.* 34:153-171.
 15. Bichet, D., Y. Lin, C. A. Ibarra, C. S. Huang, B. A. Yi, Y. N. Jan, and L. Y Jan. 2004. Evolving potassium channels by means of yeast selection reveals structural elements important for selectivity. *Proc. Natl. Acad. Sci. U.S.A.* 101:4441-4446.
 16. Domene, C., A. Grottesi, M. S. P. and Sansom. 2004. Filter Flexibility and Distortion in a Bacterial Inward Rectifier K⁺ Channel: Simulation Studies of KirBac1.1. *Biophys. J.* 87:256-267.
 17. VanDongen, A. M. J. 2004. K channel gating by an affinity switching selectivity filter. *Proc. Natl. Acad. Sci. U.S.A.* 101:3248-3252.
 18. Corsero-Morales, J. F., L. G. Cuello, Y. Zhao, V. Jogini, D. M. Cortes, B. Roux, and E. Perozo. 2006. *Nature Struct. Mol. Biol.* 13:311-318.
 19. Shrivastava, I. H., and I. Bahar. 2006. Common mechanism of pore opening shared by five different potassium channels. *Biophys. J.* 90:3929-3940.
 20. Hertel, B., S. Tayefeh, M. Mehmel, S. M. Kast, J. L. Van Etten, A. Moroni, and G. Thiel. 2006. Elongation of outer transmembrane domain alters function of miniature K⁺ channel Kcv. *J. Membrane Biol.* 210:1-9.
 21. Moroni, A., C. Visconti, V. Sangiorgio, C. Pagliuca, T. Meckel, F. Horvath, S. Gazzarrini, P. Valbuzzi, J. L. Van Etten, D. DiFrancesco, and G. Thiel. 2002. The short N-terminus is required for functional expression of the virus-encoded miniature K(+) channel Kcv. *FEBS Lett.* 530:65-69.
 22. Hertel, B. 2005. Struktur-Funktions-Beziehung in dem minimalen viralen K⁺-Kanal Kcv: Funktionelle Rolle des N-Terminus bei der Regulation von Kanalaktivität, PhD thesis. Technische Universität Darmstadt, Darmstadt, Germany.
 23. Sansom, M. S. P., I. H. Shrivastava, J. N. Bright, J. Tate, C. E. Capener, and P. C. Biggin. 2002. Potassium channels: structures, models, simulations. *Biochim. Biophys. Acta*. 1565:294-307.
 24. Woolf, T. B., and B. Roux. 1994. Molecular dynamics simulation of the gramicidin channel in a phospholipid bilayer. *Proc. Natl. Acad. Sci. U.S.A.* 91:11631-11635.
 25. Woolf, T. B., and B. Roux. 1996. Structure, energetics, and dynamics of lipid-protein interactions: A molecular dynamics study of the gramicidin A channel in a DMPC bilayer. *Protein Struct. Funct. Genet.* 23:92-112.

-
26. Berneche, S., and B. Roux. 2000. Molecular dynamics of the KcsA K^+ channel in a bilayer membrane. *Biophys. J.* 78:2900-2917.
27. Allen, T. W., S. Kuyucak, and S. H. Chung. 1999. Molecular dynamics study of the KcsA potassium channel. *Biophys J.* 77:2502-2516.
28. Roux, B., T. Allen, S. Berneche, and W. Im. 2004. Theoretical and computational models of biological ion channels. *Quart. Rev. Biophys.* 37:15-103.
29. Capener, C. E., I. H. Shrivastava, K. M. Ranatunga, L. R. Forrest, G. R. Smith, and M. S. P. Sansom. 2000. Homology modeling and molecular dynamic simulation studies of an inward rectifier potassium channel. *Biophys. J.* 28:2929-2942.
30. Capener, C. E., H. J. Kim, Y. Arinaminpathy, and M. S. P. Sansom. 2002. Ion channels: structural bioinformatics and modelling. *Hum. Mol. Genet.* 11:2425-2433.
31. Haider, S., A. Grottesi, B. A. Hall, F. M. Ashcroft, and M. S. P. Sansom. 2005. Conformational dynamics of the ligand-binding domain of inward rectifier K channels as revealed by molecular dynamics simulations: toward an understanding of Kir channel gating. *Biophys. J.* 88:3310-3320.
32. Wu, K., W. Fu, H. Liu, X. Luo, K. X. Chen, J. Ding, J. Shen, and H. Jiang. 2004. Computational simulations of interactions of scorpion toxins with the voltage-gated potassium ion channel. *Biophys. J.* 86:3542-3555.
33. Roux, B., S. Berneche, and W. Im. 2000. Ion channels, permeation, and electrostatics: insight into the function of KcsA. *Biochemistry.* 39:13295-13306.
34. Beglov, D., B. and Roux. 1997. An integral equation to describe the solvation of polar molecules in liquid water. *J. Phys. Chem. B.* 101:7821-7826.
35. Kovalenko, A., and F. Hirata. 1998. Three-dimensional density profiles of water in contact with a solute of arbitrary shape: a RISM approach. *Chem. Phys. Lett.* 290:237-244.
36. Cui, Q. Z., and V. H. Smith. 2002. K^+/Na^+ selectivity of KcsA potassium channel analyzed by reference interaction site model (RISM) integral equation theory, *Chem. Phys. Lett.* 365:110-116.
37. Cui, Q. Z., and V. H. Smith. 2005. Analysis of K^+/Na^+ selectivity of KcsA potassium channel with reference interaction site model theory. *Molec. Phys.* 103:191-201.
38. Doyle, D. A., J. C. Cabral, R. A. Pfuetzner, A. Kuo, J. M. Gulbis, S. L. Cohen, B. T. Chain, and R. MacKinnon. 1998. The structure of the potassium channel: molecular basis of K^+ conduction and selectivity. *Science.* 280:69-77.
39. Jiang, Y., A. Lee, J. Chen, M. Cadene, B. T. Chait, and R. MacKinnon. 2002. Crystal structure and mechanism of a calcium-gated potassium channel. *Nature.* 417:515-522.
40. Jiang, Y., A. Lee, J. Chen, V. Ruta, M. Cadene, B. T. Chait, and R. MacKinnon. 2003. X-ray structure of a voltage-dependent K^+ channel. *Nature.* 423:33-41.
41. Long, S. B., E. B. Campbell, and R. MacKinnon. 2005. Crystal structure of a mammalian voltage-dependent Shaker family K^+ channel. *Science.* 309:897-903.
42. Shi, N., Y. Sheng, A. Alam, L. Chen, and Y. Jiang. 2006. Atomic structure of a Na^+ and K^+ conducting channel. *Nature.* 23:427-429.
43. Durell, S. R., and H. R. Guy. 1999. Structural models of the KtrB, TrkH, and Trk1,2 symporters based on the structure of the KcsA K^+ channel. *Biophys. J.* 77:789-807.
44. Brooks, B. R., R. E. Brucolieri, B. D. Olafson, D. J. States, S. Swaminathan, and M. Karplus. 1983. CHARMM: a program for macromolecular energy, minimization, and dynamics calculations. *J. Comput. Chem.* 4. 187-217.
45. Sali A., and T. L. Blundell. 1993. Comparative protein modelling by satisfaction of spatial restraints. *J. Mol. Biol.* 234:779-815.
46. Berneche, S., and B. Roux. 2002. The ionization state and the conformation of Glu-71 in the KcsA K^+ channel. *Biophys. J.* 82:772-780.
47. Kale, L., R. Skeel, M. Bhandarkar, R. Brunner, A. Gursoy, N. Krawetz, J. Phillips, A. Shinozaki, K. Varadarajan, and K. Schulten. 1999. NAMD2: greater scalability for parallel molecular dynamics. *J. Comput. Phys.* 151:283–312.
48. MacKerell Jr., A. D., D. Bashford, M. Bellott, R. L. Dunbrack, J. D. Evanseck, M. J. Field, S. Fischer, J. Gao, H. Guo, S. Ha, D. Joseph-McCarthy, L. Kuchnir, K. Kuczera, F. T. K. Lau, C. Mattos, S. Michnick, T. Ngo, D. T. Nguyen, B. Prodhom, W. E. Reiher, B. Roux, M. Schlenkrich, J. C. Smith, R. Stote, J. Straub, M. Watanabe, J. Wiorkiewicz-Kuczera, D. Yin, and M. Karplus.

-
1998. All-atom empirical potential for molecular modelling and dynamics Studies of proteins. *J. Phys. Chem. B.* 102:3586-3616.
49. Schlenkrich, M., J. Brickmann, A. D. MacKerell Jr., and M. Karplus. 1996. An empirical potential energy function for phospholipids: criteria for parameter optimization and applications. In Biological Membranes: A Molecular Perspective from Computation and Experiment. K. M. Merz and B. Roux, editors. Birkhäuser, Boston. 31-81.
50. Jorgensen, W. L., J. Chandrasekhar, and J. D. Madura. 1983. Comparison of simple potential functions for simulating liquid water. *J. Chem. Phys.* 79:926-935.
51. Roux, B. 2006. <http://thallium.bsd.uchicago.edu/RouxLab/>.
52. Ryckaert, K. P., G. Cicotti, and H. J. C. Berendsen. 1977. Numerical integration of the Cartesian equation of motions of a system with constraints: molecular dynamics of *n*-alkanes. *J. Comp. Chem.* 23:327-341.
53. Essmann, U., L. Perera, M. L. Berkowitz, T. Darden, H. Lee, and L. H. Pedersen. 1995. A smooth particle mesh Ewald method. *J. Chem. Phys.* 103:8577-8593.
54. Tu, K., D. J. Tobias, and M. L. Klein. 1995. Constant pressure and temperature molecular dynamics simulation of a fully hydrated liquid crystal phase dipalmitoylphosphatidylcholine bilayer. *Biophys. J.* 69:2558-2562.
55. Feller, S. E., Y. Zhang, R. W. Pastor, and B. R. Brooks. 1995. Constant pressure molecular dynamics simulation: the Langevin piston method. *J. Chem. Phys.* 103:4613-4621.
56. Bernèche, S., M. Nina, and B. Roux. 1998. Molecular dynamics simulation of melittin in a dimyristoylphosphatidylcholine bilayer membrane. *Biophys. J.* 75:1603-1618.
57. Smart, O. S., J. G. Neduvvelil, X. Wang, B. A. Wallace, and M. S. P. Sansom. 1996. HOLE: a program for the analysis of the pore dimensions of ion channel structural models. *J. Mol. Graph.* 14:354-360.
58. Honig, B., K. Sharp, and A. S. Yang. 1993. Macroscopic models of aqueous solutions: biological and chemical applications. *J. Phys. Chem.* 97:1101-1109.
59. Weill Medical College of Cornell University, Department of Physiology and Biophysics. 2005. RMSDTT: RMSD Trajectory Tool, <http://physiology.med.cornell.edu/faculty/hweinstein/vmdplugins/rmsdtt/>.
60. Humphrey, W., A. Dalke, and K. Schulten. 1996. VMD - visual molecular dynamics, *J. Molec. Graphics*. 14:33-38.
61. Jogini, V., and B. Roux. 2005. Electrostatics of the intracellular vestibule of K⁺ channels. *J. Mol. Biol.* 353:272-288.
62. Nina, M., D. Beglov, and B. Roux. 1997. Atomic radii for continuum electrostatics calculations based on molecular dynamics free energy simulations. *J. Phys. Chem. B* 1001:5239-5248.
63. Im, W., D. Beglov, and B. Roux. 1998. Continuum solvation model: computation of electrostatic forces from numerical solutions to the Poisson-Boltzmann equation. *Comp. Phys. Commun.* 111:59-75.
64. Perkyns, J., and B. M. Pettitt. 1992. A site-site theory for finite concentration saline solutions. *J. Chem. Phys.* 97:7656-7666.
65. Kovalenko, A., and F. Hirata. 2000. Potentials of mean force of simple ions in ambient aqueous solution. I. Three-dimensional reference interaction site model approach. *J. Chem. Phys.* 112:10391-10402.
66. Kovalenko, A., S. Ten-No, and F. Hirata. 1999. Solution of three-dimensional reference interaction site model and hypernetted chain equations for simple point charge water by modified method of direct inversion in iterative subspace. *J. Comput. Chem.* 20:928-936.
67. Laliberte, M., and W. E. Cooper. 2004. Model for calculating the density of aqueous electrolyte solutions. *J. Chem. Eng. Data* 49:1141-1151.
68. Hasted, J. B., D. M. Ritson, and C. H. Collie. 1948. Dielectric properties of aqueous ionic solutions. Parts I and II. *J. Chem. Phys.* 16:1-21.
69. Kovalenko, A., and F. Hirata. 1999. Potential of mean force between two molecular ions in a polar molecular solvent: a study by the three-dimensional reference interaction site model. *J. Phys. Chem. B* 103:7942-7957.
70. Brickmann, J., T. Goetze, W. Heiden, G. Moeckel, S. Reiling, H. Vollhardt, and C.-D. Zachmann. 1995. Interactive visualization of molecular scenarios with MOLCAD/SYBYL. In Data

- Visualisation in Molecular Science: Tools for Insight and Innovation. J. E. Bowie, editor. Addison-Wesley, Reading, MA. 83-97.
71. Grottesi, A., C. Domene, S. Haider, and M. S. P. Sansom. 2005. Molecular dynamics simulation approaches to K channels: conformational flexibility and physiological function. *IEEE Transactions on Nanobioscience* 4:112-119.
72. Shrivastava, I. H., and M. S. P. Sansom. 2000. Simulations of ion permeation through a K channel: molecular dynamics of KcsA in a phosphor-lipid bilayer. *Biophys. J.* 78:557-570.
73. Domene, C., S. Vemparala, M. L. Klein, C. Venien-Bryan, and D. A. Doyle. 2006. Role of aromatic localization in the gating process of a potassium channel. *Biophys. J.* 90:L01-L03.
74. Pagliuca, C., T. A. Goetze, R. Wagner, G. Thiel, A. Moroni, and D. Parcej. 2007. Molecular properties of Kcv, a viral-encoded K⁺ channel. *Biochemistry*. 46:1079-1090.

Chapter 3

Model Development for the Viral Kcv Potassium Channel

Sascha Tayefeh,^{*,†} Thomas Kloss,^{*} Michael Kreim,^{*,†} Manuela Gebhardt,[†] Dirk Baumeister,[†] Brigitte Hertel,[†] (Schwalbe group),^{||} (Weber group),[§] Anna Moroni,[‡] Gerhard Thiel,[†] and Stefan M. Kast^{*1}

^{*}Eduard Zintl-Institut für Anorganische und Physikalische Chemie, [†]Institut für Botanik, Technische Universität Darmstadt, Germany, ([§]Universität Frankfurt, [§]Freie Universität Berlin,) and Dipartimento di Biologia, CNR-IBF & INFM: Consiglio Nazionale delle Ricerche-Istituto di Biofisica e Istituto Nazionale Fisica della Material, Unità di Milano Università, Milan, Italy

KEYWORDS Viral Potassium Channels, Kcv, NMR/EPR, Homology Modeling, Molecular Dynamics Simulations, 3D-RISM Integral Equation Theory

Abstract

A computational model for the open state of the short viral Kcv potassium channel has been created and tested based on homology modeling and extensive molecular dynamics simulation in a membrane environment. Particular attention was paid to the structure of the highly flexible N-terminal region and to the protonation state of membrane-exposed lysine residues. Data from various experimental sources, NMR/EPR spectroscopy and electrophysiology, as well as results from 3D-RISM integral equation theory have been taken into account in order to select the most reasonable model among possible variants. By application of an external field the final model exhibits spontaneous ion transitions across the complete pore. This happens without abnormally large driving potential and without the need to place ions artificially at certain key positions along the transition path. The transport mechanism through the filter region corresponds to the classic view of single-file motion which, in our case, is coupled to frequent exchange of ions between the innermost filter position and the cavity.

Introduction

Kcv, a viral potassium channel from *Paramecium bursaria* chlorella virus (PBCV-1) represents the shortest functional channel with only 94 amino acids (aas) per monomer known to date (1,2). The topology of Kcv comprises two transmembrane domains (TM1/TM2), the signature sequence TVGFGD, the N-terminal "slide" (s-)helix, a short pore (p-)helix, and two turrets linking TM1 with the p-helix and TM2 with the filter, respectively. Electrophysiological studies have shown that Kcv shares many functional characteristics with longer channels, such as the sensitivity to K⁺

channel blockers and voltage-dependent gating. Kcv is therefore an ideal model system for studying structure-function relationships in order to understand basic transport mechanisms.

From a microscopic perspective, availability of an atomistic Kcv channel model to be used in molecular dynamics (MD) simulation studies would be highly desirable. Most MD simulations performed thus far were based on X-ray structures, e.g. (3,4,5,6,7), although numerous examples are documented in the literature where homology models have been used for simulation, e.g. (8,9,10,11,12), and other theoretical studies (13,14,15). The Kcv crystal structure has not been determined yet. The particular problem of homology models for Kcv is related to the low sequence identity of around 10% compared to channels with available structure. We have therefore quite recently developed the hypothesis of "functional analogy" between channels (16), that extends the functional principle of conserved regions like the filter signature TXGXGD (17) to other pivotal sequence components whereas other sequence regions are poorly conserved (18). In (16) we used KirBac1.1 as "functional analog" to Kcv since a kink-forming proline is found in both cases that marks the transition between TM segment and s-helix. Furthermore, the N-terminal s-helix contains a comparable pattern of charged residues. Since successive truncation of the Kcv N-terminus leads to a loss of function when a positive residue is cut off we have therefore constructed a KirBac1.1-Kcv chimera model ("KB-Kcv"), truncated and mutated in analogy to Kcv, and studied it by extensive MD simulations and a number of novel analysis techniques. Consequences of mutations as measured by electrophysiology could be correlated quite well with properties of analogous KB-Kcv mutants.

In order to test the functional analogy hypothesis, we proceed in this work by using the complementary approach, the construction of an appropriate Kcv homology model. Due to the low sequence identity with other channels, fully automated procedures are not likely to work well. Sequence alignment has to consider pivotal positions as discussed above, so we use the KirBac1.1 structure (19) as template. We take into account all available structural experimental data, in this case from NMR/EPR study of the isolated N-terminus, a 16-residue peptide in aqueous solution (H. Schwalbe, S. Weber, personal communications). The corresponding conformation is merged with the homology model for the rest, and results are compared with a purely helical model of the N-terminus.

A further complication for model construction concerns a possibly charged lysine residue at position 29 that is most likely located in a membrane-exposed helix segment. Charged side chains play an important role for K^+ channel function, see e.g. (20). Although our Lys29 positioning might be a modeling artifact, the presence of a titratable residue in a membrane environment can not be ruled out. For instance, recent studies have shown that varying protonation states of titrable residues in a membrane environment have large impact on the structure of both, the membrane and the protein (21,22). The membrane-spanning S4 helix of other K^+ channels, which is a suspected voltage-sensor, contains four or more titratable residues carrying possibly positive charges (23). Furthermore, the free-energy penalty to include a lysine residue in the center of a hydrophobic segment is as low as 2.6 kcal mol⁻¹ (24); simulation studies show that the hydrogen-bonded network of water and lipid phosphates around a charged side-chain has a stabilizing effect (21). A

deprotonated lysine state, on the other hand, can be motivated by recognizing that the pK_a of a lysine residue in bulk water is 8.95, whereas pK_a shifts of up to -7 units in varying environments have been reported (25,26). Conclusive evidence about the protonation state is, however, not available.

No attempt has been made to determine the protonation state (i.e. the local pK_a value) of lysine in the given environment directly for instance by Poisson-Boltzmann or quantum-chemical methods. Conceptual problems with these calculations are not fully resolved yet (27,28). Instead, we focus on functional analysis of a number of possible variants based on simulations. We consequently tested both, the Lys29 protonation state and the N-terminus conformation (NMR vs. helical homology structure) by extensive MD simulations of four models, termed Kcv-HOM-K29_{deprot}, Kcv-HOM-K29_{prot}, Kcv-NMR-K29_{deprot}, and Kcv-NMR-K29_{prot}. As we will see, the results and particularly the stability analysis along the lines of (29) suggest that the model with helical N-terminal and deprotonated Lys29 (Kcv-HOM-K29_{deprot}) shows all signatures of a functional, "open-state" channel pore. This choice of the appropriate model will be further underpinned by sterical and 3D-RISM (reference interaction site model) integral equation theory (30,31) analysis, applied to structures obtained by a simulated annealing protocol, similar to our methodology described in (16). Experimental evidence for the Lys29 protonation state and location in a helix is furthermore found by electrophysiological results for a number of Lys29 mutants. As a final quality check, it is ultimately shown that the Kcv-HOM-K29_{deprot} model, when subjected to an external voltage in nonequilibrium MD simulations, exhibits reproducible single-file potassium ion transitions.

Methods

Sequence alignment and structure prediction: Since automatic multiple alignment with ClustalX (32) of Kcv with sequences of channels with known X-ray structure and a set of related sequences identified by PSI-BLAST (33) yielded no reasonable results, we proceeded by analyzing the structural properties manually. Information about the secondary structure was obtained from the structural prediction programs PROF (34), TMPRED/TMBASE (35), and TMHMM (36). Kcv consists of the pore unit only. Alignment is therefore based on the identification of s-helix, TM1, turret 1, p-helix, filter, turret 2, TM2, and a cytosolic domain (CD). There are only 26 aas downstream the signaling-sequence (the selectivity-filter, residues 63-68), which is just enough to comprise a TM helix and a linker. While there is no way to determine the length of a turret *ab initio*, the minimal length of a TM helix seems to be as short as 10 aas, e.g. residue 193-203 of a chloride channel (1KPL) or residue 77-87 of an aquaporin (1H6I). For K⁺-channels, a length of 18 aas is common. Thus, we assigned the C-terminal residues 76-94 to TM2 and residues 69-75 to turret 2. The p-helix on the opposite side of the filter has to be attached to the filter, hence position 62 marks one end of the p-helix. Its length is roughly 12 aas, which means that residues 50-62 probably form the p-helix. The N-terminal residues include TM1, while an additional s-helix may be present. Proline is known to destroy helical symmetry, and the presence of such a residue *within*

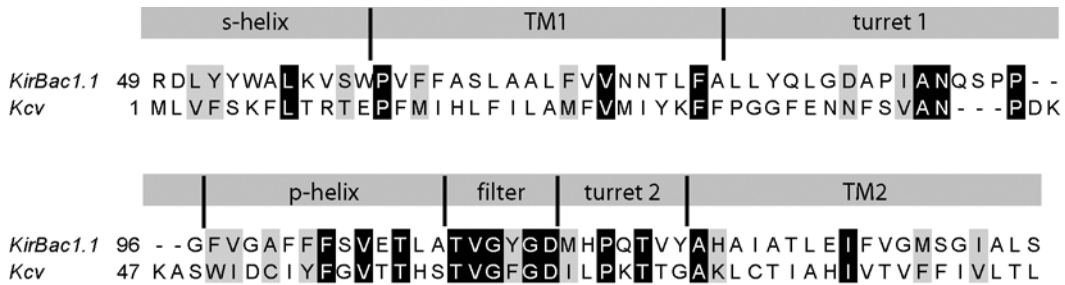


Figure 3.1: Alignment of Kcv with respect to KirBac1.1, used as input for 3D modeling. Conserved regions are highlighted (black background: identity, grey background: similarity).

a TM domain is unlikely. Proline at similar positions in MthK (37) and KirBac1.1 (19) also marks the start of the cytosolic terminus of TM1. We assigned residues 1-13 to the s-helix because it is likely that Pro13 in Kcv causes the same effect; residues 14-32 were assigned to TM1 with the typical length of 18 aas. The remaining residues 33-49 form turret 1 that links TM1 and the p-helix. All these assignments were in agreement with the results from prediction programs. In summary, we assigned for s-helix: 1-13, TM1: 14-32, turret 1: 33-49, p-helix: 50-62, filter: 63-68, turret 2: 69-75, and TM2: 76-94. The absence of a CD is in agreement with the results from the structural prediction programs. The alignment of Kcv with KirBac1.1 is shown in Figure 3.1. The regions 1-45 (s-Helix/TM1/turret 1), 46-72 (turret 1/p-helix/filter/turret 2), and 73-94 (turret 2/TM2) were aligned with ClustalX (32) independently, and the filter was aligned manually. On both sides of KirBac1.1 the N-termini were truncated by the number of residues that exceeded the length of the Kcv sequence. The aligned regions were merged and artificial gaps were removed.

3D modeling: An initial model for Kcv based on the tetrameric form of the KirBac1.1 (PDB-Code: 1P7B) X-ray template structure was created by MODELLER (38). Harmonic restraints were applied to the filter region as well as to the ions in order to prevent distortion of this sensitive region. For validation of the resulting ensemble of 100 configurations we calculated the energy, DOPE score, and the DOPE plot (39) with MODELLER, and pseudo-pair energies for all Ca-Ca pairs with PROSA II (40). PROCHECK (41) was used to evaluate the stereochemistry, e.g. by calculating Ramachandran plots (42). We chose the structure that performed best with respect to its energetic and geometric features after a number of simulated annealing refinement runs for further processing. The value of the dihedral angle formed by Arg10-Cα, Arg10-C, Thr11-N, and Thr11-Cα in the model was 179.5°, leading to an Arg10 side chain orientation hidden from the solvent. Energetic optimization using SYBYL (43) with respect to this torsion angle under the constraint of Arg10 solvent exposure yielded a value of 0° with similar energy. Missing protons were added using the academic version of CHARMM V3b1 (44) and optimized with an adopted basis Newton-Raphson minimizer for 2000 steps. The resulting geometry has a helical N-terminus and forms the basis for the models Kcv-HOM-K29_{deprot} and Kcv-HOM-K29_{prot}. For the models Kcv-NMR-K29_{deprot} and Kcv-NMR-K29_{prot} the structure of the synthetic N-terminal peptide

MLVFSKFLTRTEPFMI (see Figure 3.2) as determined by NMR/EPR spectroscopy (H. Schwalbe, S. Weber, personal communications) was merged with the original homology model by superposition of corresponding atom coordinates. MODELLER was used as described above in order to create and optimize the chimera model composed of NMR-derived N-terminus and KirBac1.1-based remaining residues. In all models Lys29 was found to be membrane-exposed. This is a direct consequence of choosing Pro13 as pivotal residue marking the transition between TM helix and N-terminus. Any other Lys29 orientation would have required the introduction of a gap between Pro13 and TM1 which is highly unlikely.

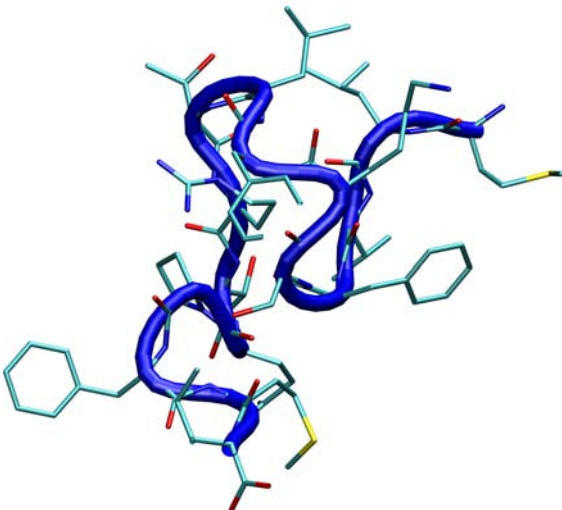


Figure 3.2: Aqueous solution structure of the isolated N-terminal peptide as obtained from NMR analysis (H. Schwalbe, personal communication).

Molecular dynamics simulations: The simulation procedures followed closely the steps used for KB-Kcv simulations performed earlier by us (16), see also (45,46). Briefly, the systems were constructed using CHARMM V3b1 with CHARMM22 potential function for proteins (47), CHARMM27 for phospholipids (48), and ion parameters from (49). All titratable residues (except for Lys29, see discussion above) were kept at their standard protonation state. The total charge was +8 for the protonated and +4 for the deprotonated models. In the latter potential function we have used CHARMM22's methylamine parameters for the lysine amino group. Simulation runs were performed with NAMD2.6 (50). Kcv-HOM-K29_{deprot} was taken as basis, translated with respect to its center of mass (located in the cavity); all other models were superposed onto the filter coordinates. The structures were embedded in DMPC membranes and KCl/TIP3P water phases of approximately 100 mM as in (16). The systems comprised 64 lipid molecules on the intracellular and 54 on the extracellular side, corresponding to a cross-sectional area of 59 Å² per DMPC molecule (46). Two K⁺ ions on filter binding sites S1 and S3 (in the terminology defined in (3)) were kept while two water molecules on S0 and S2 in the filter were created. The final ion number was 19 K⁺ throughout and 27/23 Cl⁻ for the protonated/deprotonated variants, respectively. The total number of atoms was 48707/48571/48617/48886 including 9559/9511/9529/9616 water molecules for Kcv-HOM-K29_{deprot}/Kcv-HOM-K29_{prot}/Kcv-NMR-K29_{deprot}/Kcv-NMR-K29_{prot}, respectively. The initial dimensions of the orthorhombic simulation box were 92 Å along the z axis and 72 Å in the xy plane.

Pressure was kept constant at 1 atm by the Langevin piston algorithm (51,52) with an oscillation period of 200 fs and damping constant of 100 fs. A Langevin thermostat that kept the temperature constant at 330 K was coupled to the system (coupling constant: 5 ps⁻¹). Hydrogen-

heavy atom distances were constrained using the SHAKE algorithm (53), allowing for an integration time step of 2 fs. A smooth cutoff over a distance between 10–12 Å was used to truncate the Lennard-Jones interactions. Electrostatic interactions were treated by the particle mesh Ewald algorithm (54) with a grid resolution of approx. 1 Å. Initially, simulations with harmonic restraints on the protein and the membrane were performed to allow smooth relaxation of the system. These restraints were gradually lifted. Strong restraints (force constant 10 kcal mol⁻¹ Å⁻²) were applied to the filter residues (TVGYGD) including the K⁺ ions and water molecules in the filter in order to preserve the filter-configuration, followed by a very short restraint-free *NpT* run of 20 ps at the end of the construction phase in order to allow the filter region to accommodate. The filter restraints were again applied for the initial 30 ns simulation time and removed afterwards. The total simulation time was 90.8 ns/74.4 ns/92.64 ns/43.32 ns for Kcv-HOM-K29_{deprot}/Kcv-HOM-K29_{prot}/Kcv-NMR-K29_{deprot}/Kcv-NMR-K29_{prot} systems, respectively. Two additional independent nonequilibrium simulations (Kcv-HOM-K29_{deprot}-E1 and Kcv-HOM-K29_{deprot}-E2) were performed by restarting the Kcv-HOM-K29_{deprot} trajectory after the removal of the constraints and applying a constant external electric field along the *z* axis corresponding to +100 mV over 12 ns.

Structural, thermodynamic, and dynamical evaluation: Standard techniques for evaluating simulation results like the computation of RMS fluctuations (RMSF)/thermal *B* factors and RMS deviations (RMSD) of the structures from the initial state were used for characterizing the stability of the simulations. RMSD time series calculations were carried out with the RMSDTT v1.9.2.2 plugin (55) for VMD v1.8.3 (56) for constrained and unconstrained runs, for all Cα atoms and further dissected into contributions from the s-helix only. For stability analysis in order to check and compare the homology model quality along the lines of (29) we have calculated stability measures between the initial model and the last snapshot of the unconstrained filter runs: the static RMSD between these two snapshots and the α-helicity loss, as determined by the STRIDE algorithm (57) for the complete protein, and for TM1 and TM2 separately.

Further analysis is possible with symmetrized average structures. In (16) we have outlined a procedure for extraction of such geometries from very long trajectories by a simulated annealing approach with CHARMM V3b1 in the field of average distance restraints. We followed this strategy for the rigid filter runs in this work, using the following protocol: heavy atom pairs within a cutoff of 11 Å and all Cα-Cα pair distances were averaged over the final 20 ns of the constrained trajectories. Force constant for harmonic restraints were set to 10 kcal mol⁻¹ Å⁻² for Cα-Cα pairs and to 0.25/0.25/0.10/0.15 kcal mol⁻¹ Å⁻² for all others in the Kcv-HOM-K29_{deprot}/Kcv-HOM-K29_{prot}/Kcv-NMR-K29_{deprot}/Kcv-NMR-K29_{prot} systems, respectively, all weighted by the inverse fluctuations. The values were maximized for each system separately with respect to stable annealing runs. The initial temperature was 750 K and the annealing window interval was 200 fs. Symmetrization was applied after each window as in (16).

The pore diameters of the symmetric average structures were calculated by HOLE (58). Ramachandran plot analysis has been done with PROCHECK (41). We furthermore applied 3D-

RISM integral equation theory to these structures in order to elucidate potassium and chloride ion distributions and the influence of the protonation state on these quantities. The procedure again follows closely the one outlined in (16). The solvent susceptibility was computed from the dielectrically consistent 1D-RISM equations (59,60) on a logarithmically spaced grid of 512 points ranging from $5.98 \cdot 10^{-3}$ Å to 164.02 Å using a variant of the modified inversion of iterative subspace (MDIIS) method (61). The temperature was set to 298.15 K, a 100 mM electrolyte concentration corresponding to number densities for water of 0.033236 Å^{-1} and for KCl of $0.00006022 \text{ Å}^{-1}$ (62) was used. The dielectric constant of the solvent was set to 78.4. The 3D-RISM equations were solved within the partially linearized Kovalenko-Hirata (KH) closure approximation (63) and within the second-order extension, KH-2, with parameter $\alpha = 1$ (64), on a cubic grid of 128^3 points with a 0.6 Å spacing by the MDIIS technique (61). Long-range electrostatics were treated by Ewald summation (63), taking into account conducting boundary conditions. Density distributions were integrated within the radius given by HOLE along the central channel axis, yielding a local concentration profile by dividing the number of particles within a slice of the grid by the associated slice volume.

Mutagenesis and transfection of mammalian cell lines: The Kcv gene was cloned into the BgIII and EcoRI sites of the pEGFP-N2 eukaryotic expression vector (Clontech, Palo Alto, CA) in frame with the downstream enhanced green fluorescent protein (EGFP) gene by deleting the Kcv stop codon. The point mutations K29A, K29L, K29R, K29S, K29V, K29W, and K29H were created by the QuickChange method (Stratagene, La Jolla, CA) and validated by sequencing. HEK293 cells were transfected with Kcv::EGFP and the Kcv mutants. Control cells were transfected with the empty plasmid (pEGFP-N2). The liposomal transfection reagent metafectene (Biontex Laboratories, Munich, Germany) was used to transiently transfet HEK293 cells.

Electrophysiology: After transfection, the cells were incubated at 37 °C in 5 % CO₂ for 1-2 days. The cells were dispersed by trypsin, plated at a low density on 35 mm culture dishes and allowed to settle overnight. Single cells were patch-clamped in the whole-cell configuration according to standard methods (65) using an EPC-9 patch-clamp amplifier (HEKA, Lambrecht, Germany). Data were gathered and analysed with Pulse software (HEKA). The solution that the cells were perfused with consisted of 100 mM KCl, 1.8 mM CaCl₂, 1 mM MgCl₂, and 5 mM 4-(2-hydroxyethyl)-1-piperazineethanesulfonic acid (HEPES, pH 7.4). Osmolarity was kept constant at 300 mOsmol with Choline-Cl. The pipette solution contained 130 mM D-potassium-gluconic acid, 10 mM NaCl, 5 mM HEPES, 0.1 mM guanosine triphosphate (Na salt), 0.1 µM CaCl₂, 2 mM MgCl₂, 5 mM phosphocreatine and 2 mM adenosine triphosphate (Na salt, pH 7.4).

Results and Discussion

General model features: A number of structural and topological features for our homology models, even before they were relaxed by simulations, are in agreement with X-ray structures published for other channels: (i) the characteristic topology of a K^+ channel as well as the filter geometry are preserved. Furthermore, since there is no bundle crossing of the TM2 helices, these models satisfy a proposed condition for an open state model (74). (ii) The TM domains are equipped mainly with hydrophobic residues whereas the solvent-exposed turrets and s-helices are mainly hydrophilic. (iii) The cavity is lined mainly by hydrophobic aas originating from TM2 (Phe88, Phe89, Leu92, and Leu94). In particular, the existence of one (for KcsA (66), KirBac1.1 (19), KvAP (67), and MthK (37)) or more phenylalanine residues (for NaK (68)) exposed to the cavity are typical features of K^+ channels. The overall hydrophobic cavity lining maximizes the interaction of potassium ions with water since there is hardly competition from the protein surface (69).

Model quality assessment from equilibrium simulation phenomenology: Total energy, volume, density profiles, etc. all indicate a stationary state that was reached after a few nanoseconds. As shown for the RMSD time series in Figure 3.3, all simulations with rigid filter restraints appear to be stable, since the largest part of the structural drift occurred within 3 ns. Releasing filter restraints leads, as anticipated (5,16,70), to further structural drift. Large RMSD drifts, particularly observed for Kcv-NMR-K29_{prot}, are located mainly in the highly flexible s-helices, as evidenced in the two lower panels of Figure 3.3. Notice that the protonated models (blue and green curves) show significantly less stability, particularly after release of filter restraints, as compared to deprotonated systems (red and cyan curves). This is the first indication that deprotonated Lys29 appears to be associated with more stable protein structure and a functional pore state.

More evidence for the functional deprotonated state is found by visualization of K^+ ion transition events, shown in Figure 3.4. Only the Kcv-HOM-K29_{deprot} model (top panel) is apparently capable for continuous ion transport; even in an equilibrium situation spontaneous single-file ion motion is observed after 38-39 ns (we will come back to this point later). The trajectory shows that a K^+ ion is rapidly shifted to a position near the filter as soon as it passed the intracellular mouth, as expected from the hydrophobic cavity lining. The cavity is populated on average by 2-3 ions, in line with results found for KB-Kcv wild-type in our earlier work (16). The other models, including all NMR variants, appear to rest in an inactive state. Not a single ion passage through the inner mouth is observed, even after very long simulation times.

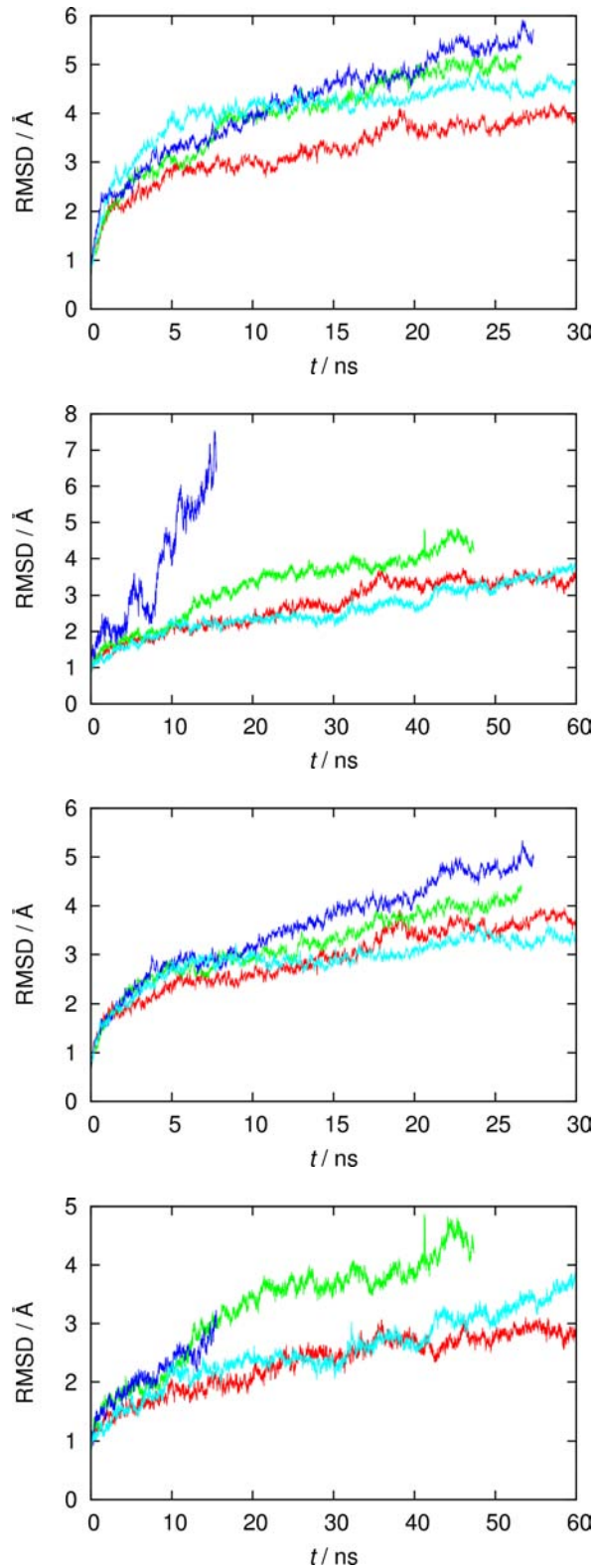


Figure 3.3: $\text{C}\alpha$ RMSD time series of the four variants (red: Kcv-HOM-K29_{deprot}, green: Kcv-HOM-K29_{prot}, cyan: Kcv-NMR-K29_{deprot}, blue: Kcv-NMR-K29_{prot}). From top to bottom: computed for all residues from rigid filter runs, subsequent fully flexible runs (time was reset to zero), computed for non s-helix residues from rigid filter, and from fully flexible runs.

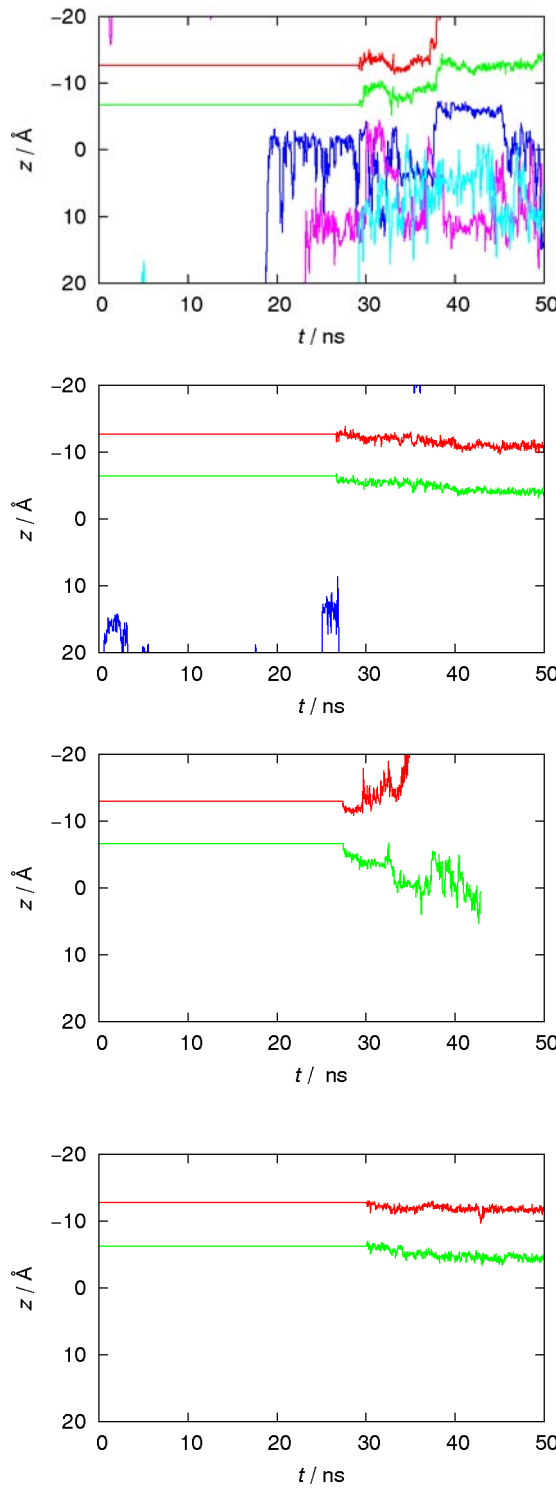


Figure 3.4: z coordinates (measured along the channel axis, intracellular mouth is located around $z = 10 \text{ \AA}$) of potassium ions over simulation time, from top to bottom: Kcv-HOM-K29_{deprot}, Kcv-HOM-K29_{prot}, Kcv-NMR-K29_{deprot}, Kcv-NMR-K29_{prot}. Only K^+ ions that rested for more than 200 ps near the protein atoms are shown.

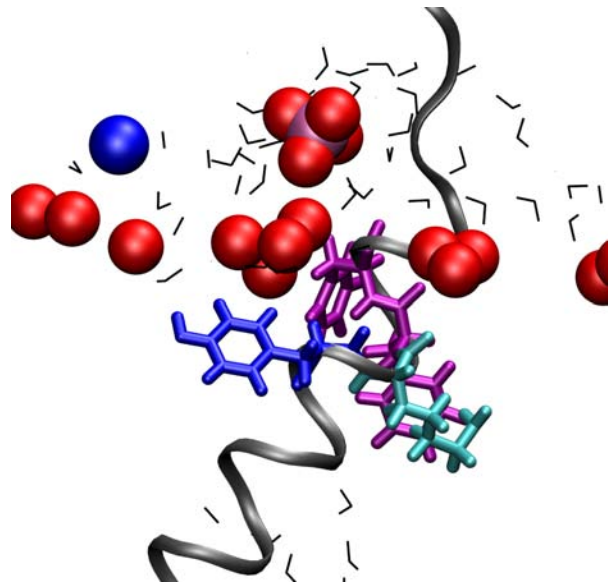


Figure 3.5: Snapshot from the Kcv-HOM-K29_{deprot} trajectory showing the conformation of residues 28-31 (YKFF) in a single TM1. Only water and lipid atoms (N: blue, P: magenta, and O: red) within a radius of 10 Å of the residues are shown. Blue sticks: Tyr28, cyan sticks: Lys29, magenta sticks: Phe30 and Phe31, grey ribbons: Kcv backbone, black lines: water.

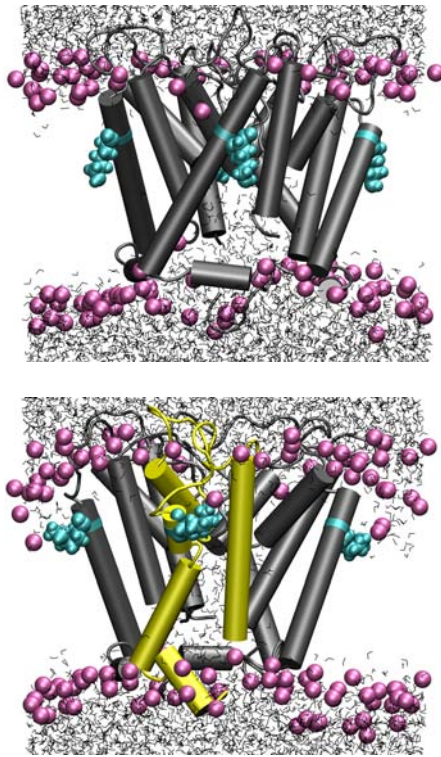


Figure 3.6: Snapshots at $t = 39$ ns (i.e. 9 ns after filter constraints were removed), Kcv-HOM-K29_{deprot} (top) and Kcv-HOM-K29_{prot} (bottom). For lipids only P atoms are shown (magenta), Lys29: cyan, water: gray tubes, cylinders: α helices as recognized by STRIDE (yellow tubes in bottom figure denote regions with largest helix loss).

	favored (%)	RMSD / Å	α -helicity loss (%)		
			total	TM1	TM2
Kcv-HOM-K29 _{deprot}	100.00	4.93	-2.33	-3.32	-9.72
Kcv-HOM-K29 _{prot}	100.00	6.50	-0.94	9.09	-13.33
Kcv-NMR-K29 _{deprot}	96.30	5.90	9.90	7.02	10.67
Kcv-NMR-K29 _{prot}	95.10	6.30	11.05	8.93	15.28
Kcv-HOM-K29 _{deprot} -E1	-	4.92	-6.67	-4.76	-14.47
Kcv-HOM-K29 _{deprot} -E2	-	6.79	0.00	-1.64	-8.45

Table 3.1: Validation of various Kcv models: percentage of residues in favored regions as obtained from Ramachandran analysis of the symmetrized average structures; C α RMSD values and α -helicity loss between the initial model and the last snapshot of the unconstrained filter simulations.

Kcv-HOM-K29_{deprot} appears to be a reasonable model also from an analysis of specific residue locations. It has been proposed that amphipathic aromatic side chains like tryptophane and tyrosine that are associated with the membrane-water interface should be located at the end of a TM domain (73). Indeed, Trp50 is located at the extracellular side, and the polar hydroxyl group of Tyr28 is in permanent contact with the lipid heads, even though it is buried in the bilayer, as shown in Figure 3.5 for Kcv-HOM-K29_{deprot}. The absence of tryptophane and tyrosine at the intracellular site is consistent with the structure of MthK (37). Furthermore, a typical salt bridge pattern is observed that resembles the situation found for our KB-Kcv model (16) and also for NaK (68): Lys6 and Arg10 both form salt bridges with the C-terminus (taking the role of Lys9 in KB-Kcv).

The effect of protonation of Lys29 becomes clearer from snapshots of the Kcv-HOM simulations, depicted in Figure 3.6. In the deprotonated state the Lys29 side chain is oriented towards the center of the lipid bilayer. Lipid head groups are barely affected; water hardly penetrates the membrane. The situation changes dramatically upon protonation: Lys29 "snorkels" (71,72) towards the extracellular side; the membrane thins out due to lipid heads getting dragged into the bilayer. This allows a significant amount of water molecules to solvate the polar Lys29 residue. Additionally, the helical structure of the TM helix gets distorted. These observations, consistent with recent simulations (22), explain the lower stability of protonated vs. deprotonated models.

There seems to be a delicate cooperation between Lys29 and its neighbors, as is also seen in Figure 3.5. Hydrophobic residues Phe30 and Phe31 are located behind Lys29, tending to interact with the hydrophobic part of the bilayer. On the other hand, Tyr28 and Lys29 penetrate similarly deep into the membrane. Tyrosine as an amphipathic aromatic residue is proposed to be located at the end of a TM (73). Although this is not the case in our model, the polar group of Tyr28 always stays in contact with the polar environment: An H-bond between the hydroxyl group of Tyr28 and an acceptor site either from water or from lipid head groups was continuously observed during the

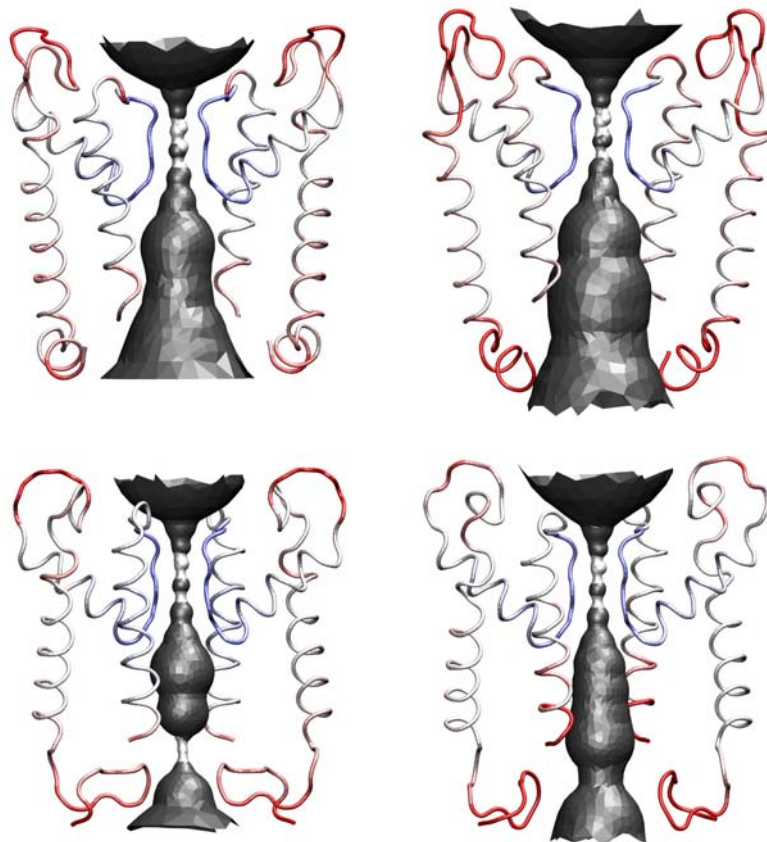


Figure 3.7: HOLE analysis and backbone atomic B factors (blue: $< 10 \text{ \AA}^2$, red: $> 20 \text{ \AA}^2$) mapped onto symmetrized average structures. Kcv-HOM-K29_{deprot} (top, left), Kcv-HOM-K29_{prot} (top, right), Kcv-NMR-K29_{deprot} (bottom, left), Kcv-NMR-K29_{prot} (bottom, right).

trajectory. The position and orientation of Tyr28 is not likely to be a modeling artifact, since tyrosine is observed at equivalent positions in the X-ray structures of KvAP (67) and MthK (37).

Table 3.1 finally summarizes stability issues in terms of α -helicity loss and static RMSD between certain snapshot structures. Both quantities are lower for deprotonated as compared to protonated models. Kcv-HOM-K29_{deprot} is the only model with no helicity loss in both TM segments. NMR models are inferior to pure homology models, as evidenced by the substantial α -helicity loss. In summary, the analyses described so far all indicate that only Kcv-HOM-K29_{deprot} represents a functional and reasonable Kcv model.

Analysis of symmetrized average structures: Figure 3.7 shows the structures of the four models as obtained from the symmetrizing annealing procedure along with the accessible volume from HOLE analysis and color-coded local B factors averaged over the final 4.5 ns of the rigid filter simulations. The intracellular mouth is formed by the s-helix, rather than by TM2, which is too short to exhibit bundle crossing of these segments, cf. (74), in line with our earlier results (16). The s-helices of full homology and NMR models are markedly different: helical structure is conserved in the former class whereas in the latter the "untangled" character of the isolated peptide

(cf. Figure 3.2) is still observed, despite the inherently large flexibility measured via thermal B factors. Another difference concerns the intracellular mouth: the mouth of the NMR models is rather closed. Particularly in the case of Kcv-NMR-K29_{prot} this static view suggests that the mouth presents a substantial sterical barrier for ions. In contrast, the intracellular mouths of both pure homology models are wide open. On the other hand, we find confirmation for the fact found earlier that an open mouth not necessarily implies permeability (16).

The open/close character of the inner mouth can directly be verified by monitoring the trajectory and does not represent an artifact from the averaging procedure. The helicity loss in the NMR model cases, summarized in Table 3.1, can also be determined visually for the symmetrized structures. It therefore appears likely that the NMR model structures should be discarded as long as functional pore states should be maintained. This does not rule out the possibility that the NMR geometry of the N-terminus plays another role for Kcv transport mechanisms.

In light of the preceding results, we analyzed only Kcv-HOM-K29_{deprot} and Kcv-HOM-K29_{prot} by 3D-RISM theory in order to address the question of the protonation state from a different perspective. Results for concentration profiles are depicted in Figure 3.8. The filter is found around $z = -15 \text{ \AA}$, the mouth at ca. $z = 10-12 \text{ \AA}$. KH and KH-2 approximation results are given in the top panel, which indicates that the profiles in the mouth region are not significantly affected by the level of theory and are therefore not an artifact of the approximation. The differences in K^+ and Cl^- concentration between deprotonated and protonated full homology models are shown in the bottom panel. It is evident that protonation of Lys29 leads to a depletion of K^+ and an enrichment of Cl^- ions in the mouth area, although the respective effect on K^+ in the filter is even larger. This corresponds with the dynamical results discussed with Figure 3.4. In summary, all computational quantities analyzed up to this point strongly favor the full homology model with deprotonated Lys29, Kcv-HOM-K29_{deprot}, as the most promising candidate for an active Kcv pore state.

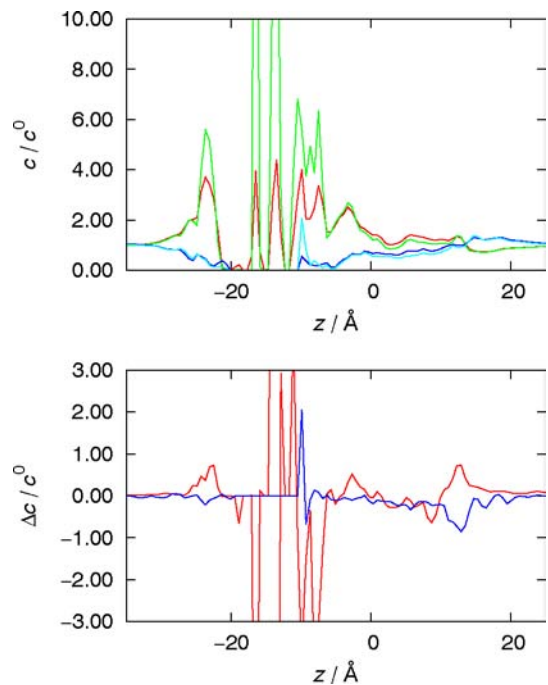


Figure 3.8: Concentration profiles along the pore axis from 3D-RISM theory for symmetrized average structures in $c^0 = 100 \text{ mM}$ KCl solution. Top: K^+ concentration within KH (red) and KH-2 (green) approximation, Cl^- concentration within KH (blue) and KH-2 (cyan) approximation, all for Kcv-HOM-K29_{deprot}. Bottom: Difference of K^+ concentrations (red) and Cl^- concentrations (blue) between Kcv-HOM-K29_{deprot} and Kcv-HOM-K29_{prot} within KH-2 approximation.

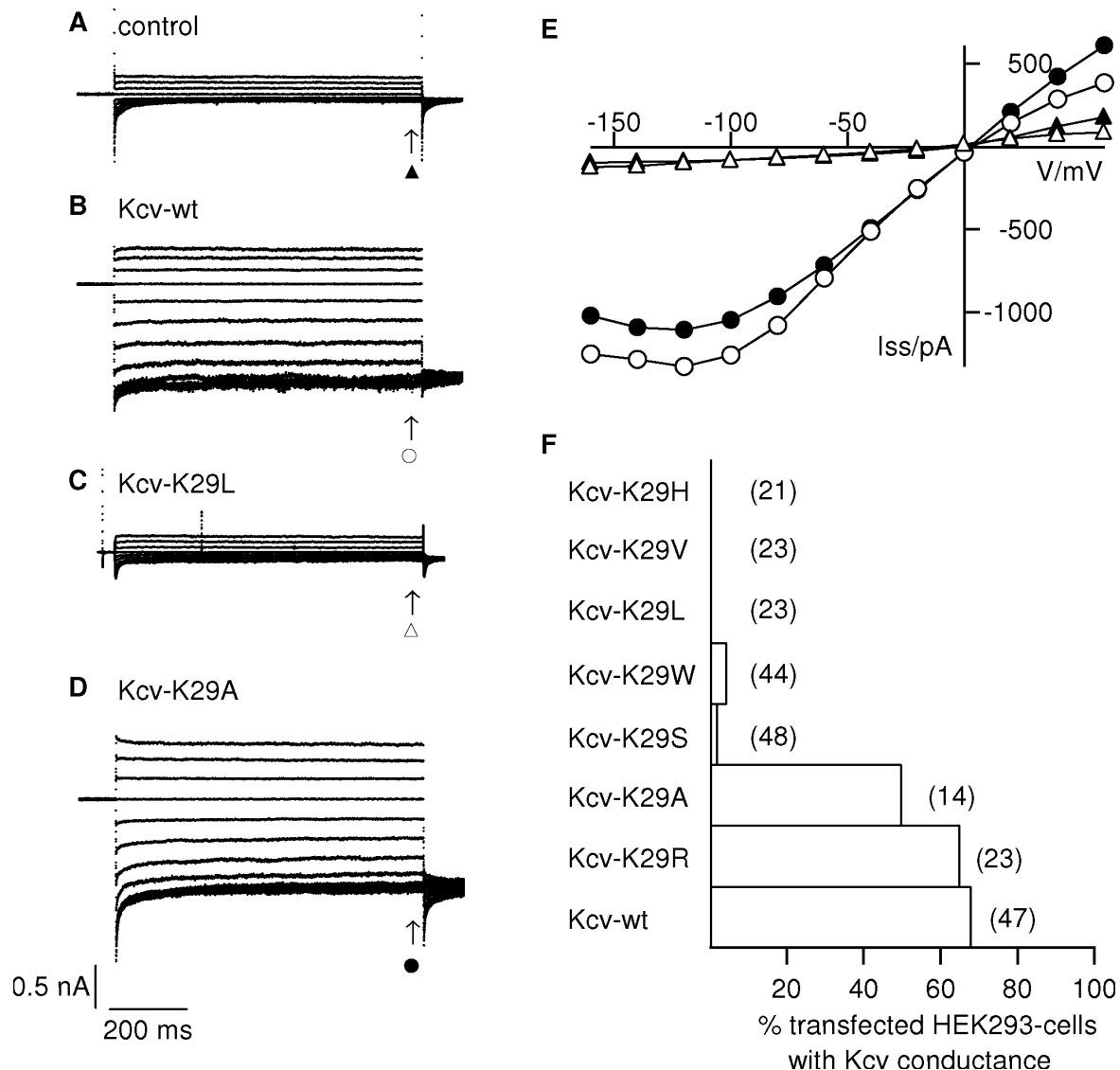


Figure 3.9: A-D: current responses of HEK293 cells transfected with GFP: control (A), KcvWT (B), Kcv-K29L (C), Kcv-K29A (D) to standard voltage protocol from holding voltage (0 mV) to test voltages between +60 mV and -160 mV. E: steady state I/V relations of currents in A-D; symbols cross-reference with symbols in A-D. (F) Percentage of transfected HEK293 cells with Kcv conductance, for KcvWT and mutants; number of recordings is indicated in brackets.

Electrophysiology: Figure 3.9 shows results from electrophysiological studies on various Lys29 mutants in order to gain more insight into the protonation state of the active system. The current responses and the corresponding *I/V* relations obtained in non transfected HEK293 cells and cells transfected with Kcv-WT are in agreement with previous measurements (2). Characteristic for Kcv currents in HEK293 cells is that the ratio of slope conductance at negative voltages (-20 mV to -60 mV) versus conductance at positive voltages (0 to +60 mV) was always > 1; in control, in non-transfected cells this ratio was significantly smaller than 1 (2). With this criterion we found that about 65% of all cells expressing the Kcv-WT gene revealed a visible Kcv type current. Also > 50% of cells expressing Kcv-K29A and Kcv-K29R were found to exhibit the same kind of Kcv-

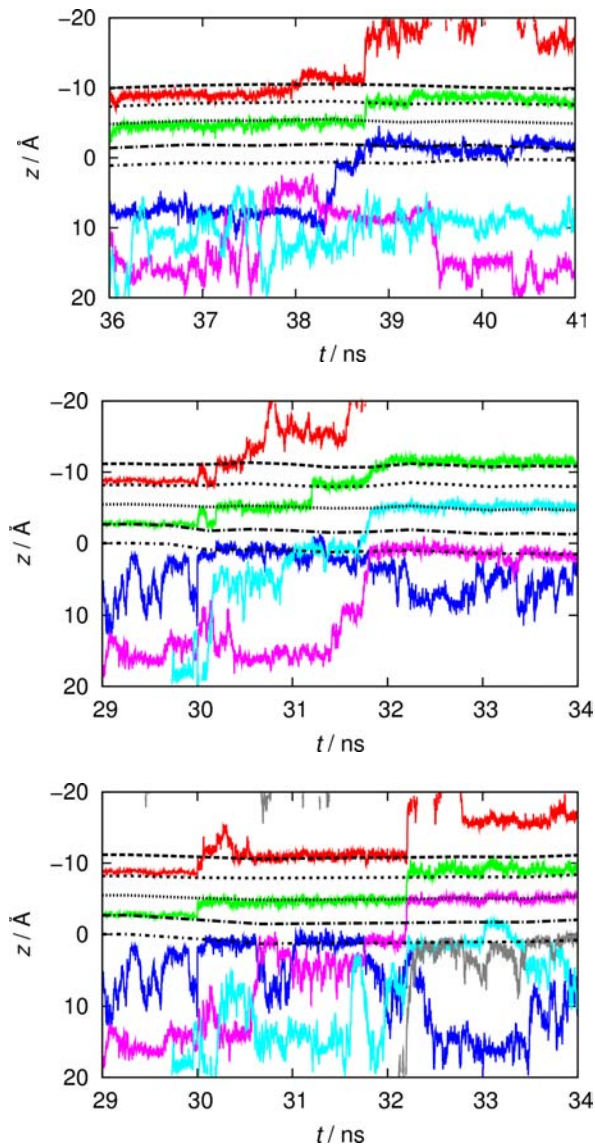


Figure 3.10: z coordinates (measured along the channel axis) of potassium ions over 6 ns simulation time for flexible filter runs of Kcv-HOM-K29deprot, from top to bottom: without external field, simulations E1 and E2 with constant external field corresponding to +100 mV voltage. Black lines show the position of binding sites S0-S4 (from top to bottom). The positions were defined as the geometric center of the oxygen rings of two adjacent filter residues (62–67).

type current (Fig 3.9, D–F). With a lower frequency, we also observed the same type of current in cells expressing either the mutant K29S or K29W (Fig 3.9, F). As far as the other mutants K29L, K29V, and K29H are concerned, no current response with the aforementioned criterion is observed. Thus, the channels either are inactive or they were not transported into the cell membrane.

The fact that the mutation of Lys29 into the non-polar residue alanine (and other non-polar amino acids) does not affect the phenotype of the Kcv conductance suggests that Lys29 in the wild type and Arg29 in the K29R mutant are not charged. The fact that arginine can replace lysine at position 29 might be an indication that the amino group indeed plays a genuine role, but it is still

very likely that arginine is deprotonated as well. Since alanine is a helix-forming residue, positioning of Lys29 in a TM segment of our model is now experimentally well-founded.

Single-file event analysis: We find K^+ ion single-file transition events for both, equilibrium and nonequilibrium trajectories of Kcv-HOM-K29_{deprot}, illustrated in Figure 3.10. Such a classic mechanism is in agreement with earlier work (3,6,12,75). This behavior serves as the ultimate quality check for the model, since it is to the best of our knowledge the first time that such a mechanism has been found for a homology model of a potassium channel. Even more interesting is the observation that ion transport through the filter is accompanied in a concerted fashion by transitions from the bulk solution into the cavity. This represents therefore the first documented case of spontaneous ion transport through the entire pore without artificially large external fields as in (6) or specific ion placements to induce the transport mechanism. In the equilibrium case (top panel of Figure 3.10), a K^+ ion enters the cavity after ca. 19 ns rigid filter simulation time. A second K^+ ion gets trapped near the intracellular mouth after around 23 ns. Immediately after lifting filter restraints, the ion at position S3 moves to position S2. Simultaneously, a third K^+ ion stays near the intracellular mouth. Less than 1 ns later, the second ion enters the cavity. For another 9 ns, these three ions randomly exchange their positions. A coordinated three- K^+ transition occurs at 38.4 ns, comprising the first K^+ ion that has entered the cavity as well as both ions in the filter. The transition event starts with one cavity ion moving to S4, and, at the same time, the ion at S1 moving to S0. For a short period (ca. 200 ps), the S0/S2/S4 configuration is formed which has been proposed to be an energetically favored (75,76,77) though rapid intermediate state (6,12). Then S4 moves to S3, the ion at S0 leaves the filter and the ion at S2 is shifted to S1 simultaneously, restoring the initial S1/S3 configuration.

A similar mechanism is observed for the two nonequilibrium trajectories, although filter transitions occur much sooner (after ca. 2 ns) and with different ion configurations as compared to the equilibrium case. Furthermore, the S0/S2/S4 configuration is longer-lived, these binding sites are always occupied right before conductance occurs (bottom panels of Figure 3.10). This is in agreement with filter-restrained simulations of Kv1.2 (6). In detail, in the first run (E1) the same S0/S2/S4 configuration as observed in the equilibrium trajectory is formed before the transition event. Ca. 1 ns after the S0 ion dissolved into the bulk, the S2 ion moves to S1. Another 0.5 ns later, it moves to S0, while the S4 ion jumps to S2 and an ion from the cavity occupies S4. Again, the S0/S2/S4 configuration is restored. In the second run (E2), the S0/S2/S4 positions are also occupied immediately after removing the restraints. During the next 2 ns two different cavity ions occupy S4 by exchanging their position twice. In contrast to the other runs, the following four events occur almost simultaneously: the S0 ion dissolves into the bulk, S2 ion moves to S1, S4 ion jumps to S2, and another ion from the cavity occupies S4. A movie of the single-file event in the second nonequilibrium trajectory is provided as supplemental material.

Concluding Remarks

All our computational and experimental analyses of the initial model and of the simulation results point to the pure homology model with deprotonated Lys29, Kcv-HOM-K29_{deprot}, as the most reasonable choice for a simulation system with an open, functional Kcv pore state. We showed that Kcv-HOM-K29_{deprot} reproduces all discussed features in agreement with experimental (2,69,73,76) and theoretical (3,5,6,22,77) data. For designing an appropriate model static structural analysis alone would not be sufficient, substantial simulation effort is essential. In our case, the ultimate model validation step was the simulation under mild nonequilibrium conditions. Single-file ion transport events, coupled to ion transitions at the inner mouth as observed in our model, are a measure for the overall quality.

Regardless of the structure of the N-terminus, taken from NMR spectroscopy or from homology modeling, protonation of Lys29 has negative impact on stability and functionality. It is important to note that apparently the protonation state of specific amino acids contributes to the presence or absence of ion transition events and therefore determines channel function. On the other hand, the NMR-based model with deprotonated Lys29 is similarly stable, though inactive. It is therefore tempting to speculate that one or both features, protonation state and N-terminal structure, might be involved in channel gating. This point requires further scrutiny. In our simulation systems, all four lysine residues were treated equivalently, although in reality all possible permutations of local protonation states could exist and modulate the pore function gradually. Analogously, from our earlier simulations of KirBac1.1-Kcv chimeras, we have inferred a possible role of the N-terminus for gating.

From a practical perspective and regardless of persisting uncertainties, Kcv-HOM-K29_{deprot} appears to be an ideal model case for studying ion transitions in K⁺ channels under conditions that are close to physiological ones or that are directly accessible in an experimental setup. This model will therefore serve as a suitable basis for future *in silico* structure-function studies.

Acknowledgement

This work was supported in part by the Deutsche Forschungsgemeinschaft (to G. T. and S. M. K.), Fonds der Chemischen Industrie and the Adolf-Messer-Stiftung (to S. M. K.), the Ministero Istruzione Università e Ricerca, Progetto Fondo per gli Investimenti della Ricerca di Base (to A. M.). Computer time was provided on IBM Regatta systems at the Hochschulrechenzentrum Darmstadt and at the Forschungszentrum Jülich. (H. S., S. W.).

Reference

-
1. Gazzarrini, S., M. Severino, M. Lombardi, M. Morandi, D. DiFrancesco, J. L. Van Etten, G. Thiel, and A. Moroni. 2003. The viral potassium channel Kcv: structural and functional features. *FEBS Lett.* 552:12-16.
 2. Plugge, B., S. Gazzarrini, M. Nelson, R. Cerana, J. L. Van Etten, C. Derst, D. DiFrancesco, A. Moroni, and G. Thiel. 2000. A potassium channel protein encoded by chlorella virus PBCV-1. *Science*. 287:1641-1644.
 3. Berneche, S., and B. Roux. 2000. Molecular dynamics of the KcsA K⁺ channel in a bilayer

-
- membrane. *Biophys. J.* 78:2900-2917.
4. Allen T. W., S. Kuyucak, and S. H. Chung. 1999. Molecular dynamics study of the KcsA potassium channel. *Biophys. J.* 77:2502-2516
 5. Domene, C., A. Grottesi, and M. S. P. Sansom. 2004. Filter flexibility and distortion in a bacterial inward rectifier K⁺ channel: Simulation studies of KirBac1.1. *Biophys. J.* 87:256-267.
 6. Fatemeh, K.A., Tajkhorshid W., and K. Schulten. 2006. Dynamics of K⁺ ion conduction through Kv1.2. *Biophys J.* 91: L72-L74.
 7. Capener C. E., P. Proks, F. M. Ashcroft, and M. S. P. Sansom. 2003. Filter flexibility in a mammalian K⁺ channel: models and simulations of Kir6.2 mutants. *Biophys. J.* 84:2345-2356.
 8. Capener, C. E., I. H. Srivastava, K. M. Ranatunga, L. R. Forrest, G. R. Smith, and M. S. P. Sansom. 2000. Homology modeling and molecular dynamics simulation studies of an inward rectifier potassium channel. *Biophys. J.* 78:2929-2942.
 9. Charlotte, C. E., H. J. Hyun, Y. Arinaminpathy, and M. S. P. Sansom. 2002. Ion channels: structural bioinformatics and modelling. *Hum. Mol. Genet.* 11:2425-2433.
 10. Haider, S., A. Grottesi, B. A. Hall, F. M. Ashcroft, and M. S. P. Sansom. 2005. Conformational dynamics of the ligand-binding domain of inward rectifier K channels as revealed by molecular dynamics simulations: toward an understanding of Kir channel gating. *Biophys. J.* 88:3310-3320.
 11. Yu, K., W. Fu, H. Liu, X. Luo, K. X. Chen, J. Ding, J. Shen, and H. Jiang. 2004. Computational simulations of interactions of scorpion toxins with the voltage-gated potassium ion channel. *Biophys. J.* 86:3542-3555.
 12. Sansom, M. S. P., I. H. Srivastava, J. N. Bright, J. Tate, C. E. Capener, and P. C Biggin. 2002. Potassium channels: structures, models, simulations. *Biochim. Biophys. Acta.* 1565:294-307.
 13. Bichet, D., M. Grabe, Y. N. Jan, and L. Y. Jan. 2006. Electrostatic interactions in the channel cavity as an important determinant of potassium channel selectivity. *Proc. Natl. Acad. Sci. USA.* 103:14355-14360.
 14. Grabe, M., D. Bichet, X. Qian, Y. N. Jan, and L. Y. Jan. 2006. K⁺ channel selectivity depends on kinetic as well as thermodynamic factors. *Proc. Natl. Acad. Sci. USA.* 103: 14361-14366.
 15. Hertel, B., S. Tayefeh, M. Mehmel, S. M. Kast, J. Van Etten, A. Moroni, and G. Thiel. 2006. Elongation of outer transmembrane domain alters function of miniature K⁺ channel Kcv. *J. Membrane Biol.* 210:1-9.
 16. Tayefeh, S., T. Kloss, G. Thiel, B. Hertel, A. Moroni, and S. M. Kast. 2007. Molecular Dynamics Simulation of the Cytosolic Mouth in Kcv-type Potassium Channels. *Biochemistry.* 46:4826-4839.
 17. Heginbotham, L., T. Abramson, and R. MacKinnon. 1992. A functional connection between the pores of distantly related ion channels as revealed by mutant K⁺ channels. *Science.* 258:1152-1155.
 18. Durell S. R., Y. Hao, and H. R. Guy. 1998. Structural models of the transmembrane region of voltage-gated and other K⁺ channels in open, closed, and inactivated conformations. *J. Struct. Biol.* 121:263-284.
 19. Kuo, A., J. M. Gulbis, J. F. Antcliff, T. Rahman, E. D. Lowe, J. Zimmer, J. Cuthbertson, F. M. Ashcroft, T. Ezaki, and D. A. Doyle. 2003. Crystal structure of the potassium channel KirBac1.1 in the closed state. *Science.* 300:1922-1926.
 20. Schulte U., and B. Fakler. 2000. Gating of inward-rectifier K⁺ channels by intracellular pH. *Eur. J. Biochem.* 267:5837-5841.
 21. Freites J. A., J. T. Douglas, G. von Heijne, and S. H. White. 2005. Interface connections of a transmembrane voltage sensor. *Proc. Natl. Acad. Sci. USA.* 102:15059-15064.
 22. Dorairaj S., and T. W. Allen. 2007. On the thermodynamic stability of a charged arginine side chain in a transmembrane helix. *Proc. Natl. Acad. Sci. USA.* 104:4943-4948.
 23. Long S. B., E. B. Campbell, and R. MacKinnon. 2005. Voltage sensor of Kv1.2: structural basis of electromechanical coupling. *Science.* 309:903-908
 24. Hessa T., H. Kim, K. Bihlmaier, C. Lundin, J. Boekel, H. Andersson, I. M. Nilsson, S. H. White, and G. von Heijne. 2005. Recognition of transmembrane helices by the endoplasmic reticulum translocon. *Nature* 433:377-381.
 25. Schutz, C. N., and A. Warshel. 2001. What are the dielectric "constants" of proteins and how to validate electrostatic models? *Proteins.* 44:400-417.
 26. Cymes, G. D., Y. Ni, and C. Grosman. 2005. Probing ion-channel pores one proton at a time. *Nature.* 438:975-980.

-
27. Warshel, A., S. T. Russell, and A. K. Churg. 1984. Macroscopic models for studies of electrostatic interactions in proteins: limitations and applicability. *Proc. Natl. Acad. Sci. USA.* 81:4785-4789.
28. Mehler E. L., M. Fuxreiter, I. Simon, and E. B. Garcia-Moreno. 2002. The role of hydrophobic microenvironments in modulating pKa shifts in proteins. *Proteins.* 48:283-292.
29. Holyoake, J., V. Caulfeild, S. A. Baldwin, and M. S. P Sansom. 2006. Modeling, docking, and simulation of the major facilitator superfamily. *Biophys. J.* 91:L84-L86.
30. Beglov, D., and B. Roux. 1997. An integral equation to describe the solvation of polar molecules in liquid water. *J. Phys. Chem. B* 101:7821-7826.
31. Kovalenko, A., F. and Hirata. 1998. Three-dimensional density profiles of water in contact with a solute of arbitrary shape: a RISM approach. *Chem. Phys. Lett.* 290:237-244.
32. Thompson, J. D., T. J. Gibson, F. Plewniak, F. Jeanmougin, and D. G. Higgins. 1997. The ClustalX windows interface: flexible strategies for multiple sequence alignment aided by quality analysis tools. *Nucleic Acids Res.* 24:4876-4882.
33. Altschul, S. F., T. L. Madden, A. A. Schäffer, J. Zhang, Z. Zhang, W. Miller, and D. J. Lipman. 1997. Gapped BLAST and PSI-BLAST: a new generation of protein database search programs. *Nucleic Acids Res.* 25:3389-3402.
34. Rost, B. 2001. Protein Secondary Structure Prediction Continues to Rise. *J. Struct. Biol.* 134:204-218.
35. Hofmann K., and W. Stoffel. 1993. TMbase - A database of membrane spanning proteins segments. *Biol. Chem. Hoppe-Seyler.* 374:166-170.
36. Sonnhammer E. L. L, G. von Heijne, and A. Krogh. 1998. A hidden Markov model for predicting transmembrane helices in protein sequences. In Proceedings of the Sixth International Conference on Intelligent Systems for Molecular Biology. J. Glasgow, T. Littlejohn, F. Major, R. Lathrop, D. Sankoff, and C. Sensen, editors. AAAI Press Menlo Park, CA. 175-182.
37. Jiang, Y., A. Lee, J. Chen, M. Cadene, B. T. Chait, and R. MacKinnon. 2002. Crystal structure and mechanism of a calcium-gated potassium channel. *Nature.* 417:515-522.
38. Martí-Renom M. A., A. Stuart, A. Fiser, R. Sánchez, F. Melo, and A. Sali. 2000. Comparative protein structure modeling of genes and genomes. *Annu. Rev. Biophys. Biomol. Struct.* 29:291-325.
39. Eramian D., S. Min-yi, D. Devos, F. Melo, A. Sali, and M. A. Martí-Renom. 2006. A composite score for predicting errors in protein structure models. *Protein Sci.* 15:1653-1666.
40. Sippl, M. J. 1993. Recognition of errors in three-dimensional structures of proteins. *Proteins.* 17:355-362.
41. Laskowski, R. A., MacArthur, M. W., Moss, D. S., and J. M. Thornton. 1993. PROCHECK: A program to check the stereochemical quality of protein structures. *J. Appl. Cryst.* 26:283-291.
42. Law, R. J., C. Capener, M. Baaden, P. J. Bond, J. Campbell, G. Patargias, Y. Arinaminpathy, and M. S.P. Sansom. 2005. Membrane protein structure quality in molecular dynamics simulation. *J. Mol. Graph. Model.* 24:157-165.
43. SYBYL (Tripos Inc., St. Louis, MO)
44. Brooks, B. R., R. E. Brucoleri, B. D. Olafson, D. J. States, S. Swaminathan, and M. Karplus. 1983. CHARMM: a program for macromolecular energy, minimization, and dynamics calculations. *J. Comput. Chem.* 4:187-217.
45. Berneche, S., M. Nina, and B. Roux. 1998. Molecular dynamics simulation of melittin in a dimyristoylphosphatidylcholine bilayer membrane. *Biophys. J.* 75:1603-1618.
46. Woolf, T. B., and B. Roux. 1994. Molecular dynamics simulation of the gramicidin channel in a phospholipid bilayer. *Proc. Natl. Acad. Sci. USA.* 91:11631-11635.
47. MacKerell Jr., A. D., D. Bashford, M. Bellott, R. L. Dunbrack, J. D. Evanseck, M. J. Field, S. Fischer, J. Gao, H. Guo, S. Ha, D. Joseph-McCarthy, L. Kuchnir, K. Kuczera, F. T. K. Lau, C. Mattos, S. Michnick, T. Ngo, D. T. Nguyen, B. Prodhom, W. E. Reiher, B. Roux, M. Schlenkrich, J. C. Smith, R. Stote, J. Straub, M. Watanabe, J. Wiorkiewicz-Kuczera, D. Yin, and M. Karplus. 1998. All-atom empirical potential for molecular modelling and dynamics Studies of proteins. *J. Phys. Chem. B.* 102:3586-3616.
48. Schlenkrich, M., J. Brickmann, A. D. MacKerell Jr., and M. Karplus. 1996. An empirical potential energy function for phospholipids: criteria for parameter optimization and applications. In Biological Membranes: A Molecular Perspective from Computation and Experiment. K. M. Merz and B. Roux, editors. Birkhäuser, Boston. 31-81.

-
49. Roux Lab Home Page. 2006. <http://thallium.bsd.uchicago.edu/RouxLab/>.
50. Kale, L., R. Skeel, M. Bhandarkar, R. Brunner, A. Gursoy, N. Krawetz, J. Phillips, A. Shinozaki, K. Varadarajan, and K. Schulten. 1999. NAMD2: greater scalability for parallel molecular dynamics. *J. Comput. Phys.* 151:283-312.
51. Tu, K., D. J. Tobias, and M. L. Klein. 1995. Constant pressure and temperature molecular dynamics simulation of a fully hydrated liquid crystal phase dipalmitoylphosphatidylcholine bilayer. *Biophys. J.* 69:2558-2562.
52. Feller, S. E., Y. Zhang, R. W. Pastor, and B. R. Brooks. 1995. Constant pressure molecular dynamics simulation: the Langevin piston method. *J. Chem. Phys.* 103:4613-4621.
53. Ryckaert, J.-P., G. Ciccotti, and H. J. C. Berendsen. 1977. Numerical integration of the Cartesian equation of motions of a system with constraints: molecular dynamics of *n*-alkanes. *J. Comp. Chem.* 23:327-341.
54. Essmann, U., L. Perera, M. L. Berkowitz, T. Darden, H. Lee, and L. G. Pedersen. 1995. A smooth particle mesh Ewald method. *J. Chem. Phys.* 103:8577-8593.
55. Weill Medical College of Cornell University, Department of Physiology and Biophysics. RMSDTT: RMSD Trajectory Tool. 2005. <http://physiology.med.cornell.edu/faculty/hweinstein/vmdplugins/rmsdtt/>
56. Humphrey, W., Dalke, A. and K. Schulten. 1996. VMD - Visual molecular dynamics. *J. Molec. Graphics.* 14:33-38.
57. Frishman, D., and P. Argos. 1995. Knowledge-based protein secondary structure assignment. *Proteins.* 23:566-579.
58. Smart, O. S., J. G. Neduvvelil, X. Wang, B. A. Wallace, and M. S. P. Sansom. 1996. HOLE: a program for the analysis of the pore dimensions of ion channel structural models. *J. Mol. Graph.* 14:354-360.
59. Perkyns, J., and B. M. Pettitt. 1992. A site-site theory for finite concentration saline solutions *J. Chem. Phys.* 97:7656-7666.
60. Kovalenko, A., F., and Hirata. 2000. Potentials of mean force of simple ions in ambient aqueous solution. I. Three-dimensional reference interaction site model approach. *J. Chem. Phys.* 112:10391-10402.
61. Kovalenko, A. S. Ten-No, and F. Hirata. 1999. Solution of three-dimensional reference interaction site model and hypernetted chain equations for simple point charge water by modified method of direct inversion in iterative subspace. *J. Comput. Chem.* 20:928-936.
62. Laliberté, M., and W. E. Cooper. 2004. Model for calculating the density of aqueous electrolyte solutions. *J. Chem. Eng. Data.* 49:1141-1151.
63. Kovalenko, A., and F. Hirata. 1999. Potential of mean force between two molecular ions in a polar molecular solvent: a study by the three-dimensional reference interaction site model. *J. Phys. Chem. B* 103:7942-7957.
64. Omelyan, I., A. Kovalenko, and F. Hirata. 2004. Microscopic description of a liquid-vapor interface by an inhomogeneous integral equation theory. *Chem. Phys. Lett.* 397:368-373.
65. Hamill, O. P., A. Marty, E. Neher, B. Sakmann, and F. Sigworth. 1981. Improved patch-clamp techniques for high-resolution current recording from cells and cell-free membrane patches. *Pfluegers Arch.* 391:85-100.
66. Doyle, D. A., J. M. Cabral, R. A. Pfuetzner, A. Kuo, J. M. Gulbis, S. L. Cohen, B. T. Chain, and R. MacKinnon. 1998. The structure of the potassium channel: Molecular basis of K⁺ conduction and selectivity. *Science.* 280:69-77.
67. Jiang, Y., A. Lee, J. Chen, V. Ruta, M. Cadene, B. T. Chait, and R. MacKinnon. 2003. X-ray structure of a voltage-dependent K⁺ channel. *Nature.* 423:33-41
68. Shi, N., Y. Sheng, A. Alam, L. Chen, and Y. Jiang. 2006. Atomic structure of a Na⁺ and K⁺ conducting channel. *Nature.* 440:427-429.
69. Zhou, Y., J. H. Morais-Cabral, A. Kaufman, and R. MacKinnon. 2001. Chemistry of ion coordination and hydration revealed by a K⁺ channel-fab complex at 2.0 Å resolution. *Nature.* 414:43-48.
70. Grottesi, A., C. Domene, S. Haider, and M. S. P. Sansom. 2005. Molecular dynamics simulation approaches to K channels: Conformational flexibility and physiological function. *Ieee T Nanobiosci* 4:112-119.

-
71. Killian, J. A. and G. von Heijne. 2000. How proteins adapt to a membrane-water interface. *Trends Biochem Sci.* 25:429-434.
 72. Strandberg, E. and J. A. Killian. 2003. Snorkeling of lysine side chains in transmembrane helices: how easy can it get? *FEBS Lett.* 544:69-73.
 73. Nyholm, T. K. M., S. Ozdirekcan, and J. A. Killian. 2007. How protein transmembrane segments sense the lipid environment. *Biochemistry.* 46:1457-1465.
 74. Jiang, Y., A. Lee, J. Chen, M. Cadene, B. T. Chait B. T., and R. MacKinnon. 2002. The open pore conformation of potassium channels. *Nature.* 417:523-526.
 75. Berneche, S., and B. Roux. 2001. Energetics of ion conduction through the K⁺ channel. *Nature.* 414:73-77.
 76. Morais-Cabral, J. H., Y Zhou, and R. MacKinnon. 2001. Energetic optimization of ion conduction rate by the K⁺ selectivity filter. *Nature.* 414:37-42.
 77. Berneche, S., and B. Roux. 2003. A microscopic view of ion conduction through the K⁺ channel. *Proc. Natl. Acad. Sci. USA.* 100:8644-8648.

Chapter 4

The Dysfunctional Truncation Mutants

This chapter deals with the investigation of two N-terminal truncation mutants. The first one is Kcv Δ N8, a truncation mutant with very low activity (1). The other one is Kcv Δ N14, a totally dysfunctional mutant (2).

The truncation models were used as starting structures for the 102 ns/99 ns MD simulation of Kcv Δ N8/Kcv Δ N14 in a bilayer/solvent system using the same conditions and parameters as described in Chapter 3. Only exceptions are mentioned in the following. The lipid number was 64 on the intracellular and 54 on the extracellular side. 19 K $^+$ and 19 Cl $^-$ were added to the bulk. The total number of atoms was 48805/48683 including 9663/9761 water-molecules for the Kcv Δ N8/Kcv Δ N14-system.

The average structures generated by the simulated annealing protocol (Chapter 2 and 3) were calculated using a restraint force constant of 10 kcal mol $^{-1}$ Å $^{-2}$ between C α -C α pairs, and between all other atom-pairs this value was set to 0.20 kcal mol $^{-1}$ Å $^{-2}$ and 0.25 kcal mol $^{-1}$ Å $^{-2}$ in case of the Kcv Δ N8 and the Kcv Δ N14-system, respectively. All force constants were weighted by the inverse fluctuation of the target distances.

The alignments used for 3D-modelling is shown in Figure 4.1. The loss of basic residues in the N-Terminus correlates with the loss of conductivity in electrophysiological experiments (1,2).

Figure 4.2 shows the accessible free volume of the models (bold lines) compared to the known K $^+$ channel X-ray structures (thin dashed lines). The intracellular constriction is located at z ~ 10 - 20 Å. The conformation is equivalent to the "open" state of K $^+$ channel X-ray structures (3,4,5) and stands in marked contrast to the "closed" state (6,7,8). Both, the active KcvWT and the dysfunctional truncation models, lack a sterical barrier for K $^+$ ions at the intracellular constriction.

This is consistent with the HOLE results from the analogous KirBac1.1 truncation model (Chapter 2).

	s-helix	TM1			turret 1
		p-helix	filter	turret 2	TM2
KirBac1.1	49 RDL YYWALKVSWPVFFASL AALFVNNNTLFALLYQLGDAPIANQSPP--				
KcvWT	1 MLVFSKFLTRTEPFM IHLF I LAMFVMIYKFPFGGFENNFSVAN---PDK				
Kcv Δ N8	1 - - - - -MRTEPFM IHLF I LAMFVMIYKFPFGGFENNFSVAN---PDK				
Kcv Δ N14	1 - - - - - - - - - M IHLF I LAMFVMIYKFPFGGFENNFSVAN---PDK				

Figure 4.1: Alignment of KirBac1.1 vs. Kcv variations as derived from manual deduction. s-helix = slide-helix; TM1/TM2 = transmembrane domain 1/2; p-helix = pore helix; filter = highly conserved selectivity filter; turret 1/2 = loop 1/2. Conserved regions are highlighted (black background: identity, grey background: similarity).

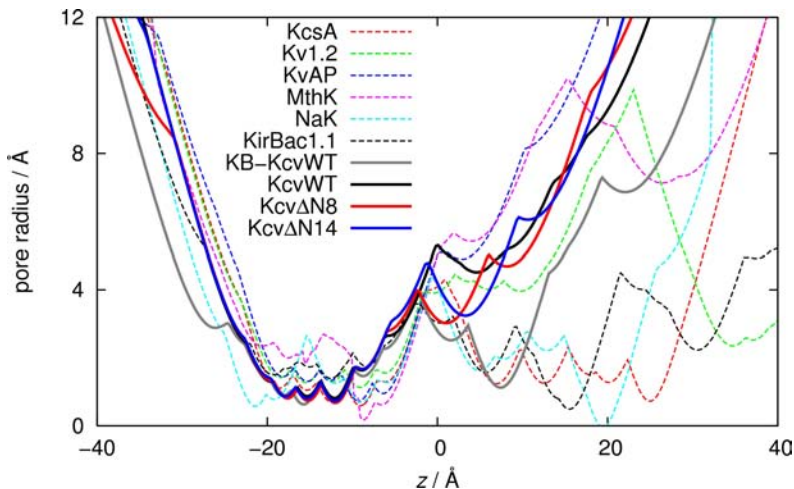


Figure 4.2: Channel pore radii versus position along the channel axis. The intracellular mouth is located at $z \sim 10\text{--}20 \text{ \AA}$. The Kcv-models are plotted with bold lines (red: KcvWT, green: KcvΔN8, blue: KcvΔN14). For comparison, the radii of K^+ channels from X-ray structure analysis are plotted with thin and dashed lines. (red: KcsA, green: Kv1.2, blue: KvAP, magenta: MthK, cyan: NaK, and black: KirBac1.1).

Although K^+ ions were free to enter the cavity (Figure 4.3, plots), a full transition cycle as described in Chapter 3 for the trajectory of KcvWT was not observed. Instead, a “ K^+ blockage” emerged at the intracellular constriction, which is most pronounced in the KcvΔN14 simulation. Such a blockage was also observed in the trajectory of the KB-KcvΔN8 model and is discussed in Chapter 2.

The results of the 3D-RISM analysis of the final models elucidate the origin of the K^+ blockage (Figure 4.3, pictures). Compared to KcvWT, the K^+ density at the intracellular mouth is higher in the truncation mutants. This result is consistent with the 3D-RISM analysis of the KB-KcvΔN8 model, and the salt-bridge pattern of both channels are also equivalent (Figure 4.3).

In summary, the increased interaction between K^+ ions and the C-terminus as a consequence of differing salt bridge patterns is the only difference between the KcvWT and the truncation mutants. Thus, it is concluded that the strong coordination between K^+ ions and the C-termini is the main cause for the dysfunction of these truncation mutants. Since the salt-bridge patterns and their role of these homology models are similar to the patterns and their role of the analogous KB-Kcv models, it is evident that the functional analogy hypothesis works.

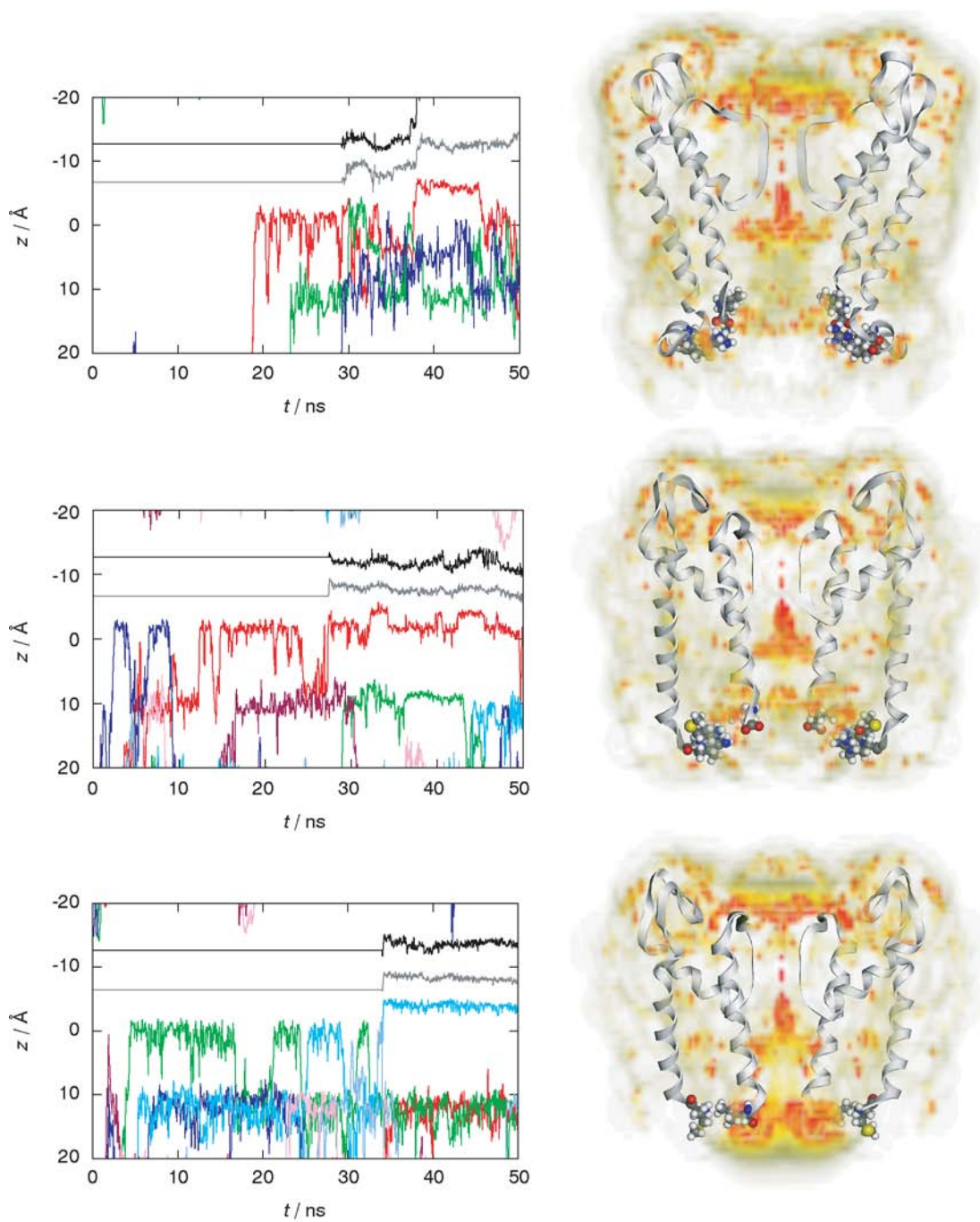


Figure 4.3: PLOTS: Locations on the pore axis (z) of K^+ ions during the simulation of KcvWT (top), Kcv Δ N8 (middle) and Kcv Δ N14 (bottom). Only K^+ ions that rested more than 200 ps near the protein are shown. Each color codes for an individual ion. PICTURES: Color-coded K^+ density distribution from 3D-RISM-KH theory around fully solvated WT and mutant channel structures in 1 M KCl solution (same order as plots). Density increases from transparent (bulk value and below) over gray and yellow to red. Crucial amino-acids contributing to the salt-bridge pattern at the intracellular side are explicitly depicted.

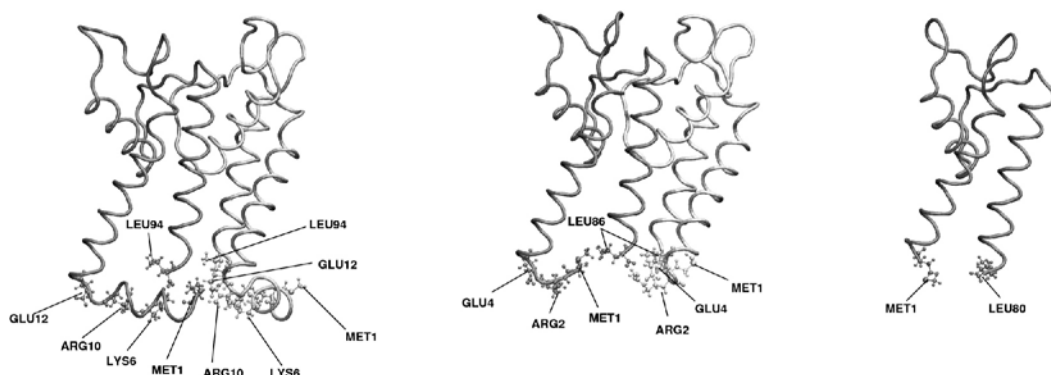


Figure 4.4: Salt-bridge pattern at the cytosolic site of KcvWT (left), Kcv Δ N8 (center), and Kcv Δ N14 (right). The backbone structures of the Kcv models were obtained from simulated annealing with atom-distances averaged from trajectories used as restraints. For clearance, only the smallest asymmetric subunit is shown. A dimer is shown in case of KcvWT and Kcv Δ N8, because the salt-bridges comprised residues from two subunits. In case of Kcv Δ N14 salt-bridges were observed only within the same monomer.

Reference

1. Hertel, B. 2005. Struktur-Funktions-Beziehung in dem minimalen viralen K^+ Kanal Kcv: Funktionelle Rolle des N-terminus bei der Regulation von Kanalaktivität. PhD-Thesis. Technische Universität Darmstadt.
2. Moroni, A., C. Visconti, V. Sangiorgio, C. Pagliuca, T. Meckel, F. Horvath, S. Gazzarrini, P. Valbuzzi, J. L. Van Etten, D. DiFrancesco, and G. Thiel. 2002. The short N-terminus is required for functional expression of the virus-encoded miniature K^+ channel Kcv. *FEBS Lett.* 530:65-69.
3. Long, S. B., E. B. Campbell, and R. MacKinnon. 2005. Crystal structure of a mammalian voltage-dependent Shaker family K^+ channel. *Science*. 309:897-903.
4. Jiang, Y., A. Lee, J. Chen, M. Cadene, B. T. Chait, and R. MacKinnon. 2002. Crystal structure and mechanism of a calcium-gated potassium channel. *Nature*. 417:515-522.
5. Jiang, Y., A. Lee, J. Chen, V. Ruta, M. Cadene, B. T. Chait, and R. MacKinnon. 2003. X-ray structure of a voltage-dependent K^+ channel. *Nature*. 423:33-41.
6. Doyle, D. A., J. M. Cabral, R. A. Pfuetzner, A. Kuo, J. M. Gulbis, S. L. Cohen, B. T. Chain, and R. MacKinnon. 1998. The structure of the potassium channel: Molecular basis of K^+ conduction and selectivity. *Science*. 280:69-77.
7. Kuo, A., J. M. Gulbis, J. F. Antcliff, T. Rahman, E. D. Lowe, J. Zimmer, J. Cuthbertson, F. M. Ashcroft, T. Ezaki, and D. A. Doyle. 2003. Crystal structure of the potassium channel KirBac1.1 in the closed state. *Science*. 300:1922-1926.
8. Shi, N., Y. Sheng, A. Alam, L. Chen, and Y. Jiang. 2006. Atomic structure of a Na^+ and K^+ conducting channel. *Nature*. 440:427-429.

Chapter 5

Structure and Dynamics of the KcvP13A mutant model

To complete the studies on the P13A mutant of Kcv, a homology model (hereafter referred to as “KcvP13A”) was created and simulated. The initial homology model was derived from ModellerV8.1 using the coordinates of the previously created initial KcvWT model (Chapter 3) as template. The annealed and evaluated point mutant homology model of KcvP13A was subject to MD simulation in explicit bilayer and solvent.

The conditions and parameters of the MD simulation and the analysis protocol were equivalent to those used before, so only differences are mentioned here. A KCl concentration of 100 mM was imposed by adding 19 K^+ and 23 Cl^- ions to 9531 TIP3 water molecules. The lipid molecule number was 64 on the intracellular side and 54 on the extracellular side. The total number of simulated atoms was 48961. The initial rigid filter simulation run was extended to ~ 97 ns to verify the stability of the protein structure. A 20 ns restraint-free simulation run was started using the coordinates and velocities at $t = 30$ ns. Average structures were obtained by applying the simulated annealing protocol introduced in Chapter 2. In addition to a symmetrized structure, a non-symmetrized structure was obtained by skipping the symmetrization step of the annealing procedure. The distances used as harmonic restraints were averaged over the final 80 ns of the rigid filter trajectory. The force constant between $\text{C}\alpha\text{--C}\alpha$ pairs was set to 10 $\text{kcal mol}^{-1} \text{\AA}^{-2}$, and those between all other atom-pairs was set to 0.3 $\text{kcal mol}^{-1} \text{\AA}^{-2}$. All force constants were weighted by the inverse fluctuation of the target distances.

K^+ ion dynamics

In contrast to KcvWT and KB-KcvWT, multiple ion transition events did not occur. Instead, one single ion transition event from the cytosolic site into the cavity was observed (Figure 5.1). This is

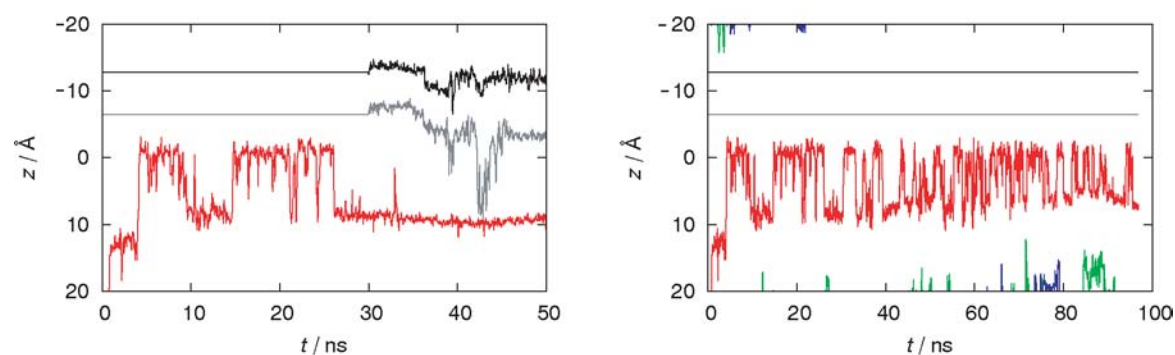


Figure 5.1: z coordinates of K^+ ions. Only K^+ ions that reside more than 1 ns within the cavity or filter region are depicted. The filter region is located between $\sim -5 \text{ \AA}$ and -15 \AA . The time series plotted in the figure to the left provides 30 ns of the rigid filter simulation, followed by a restraint-free run that was started from the last snapshot at $t = 30$ ns. The figure to the right shows the complete 97 ns of the extended rigid filter run. The initial 30 ns are redundant.

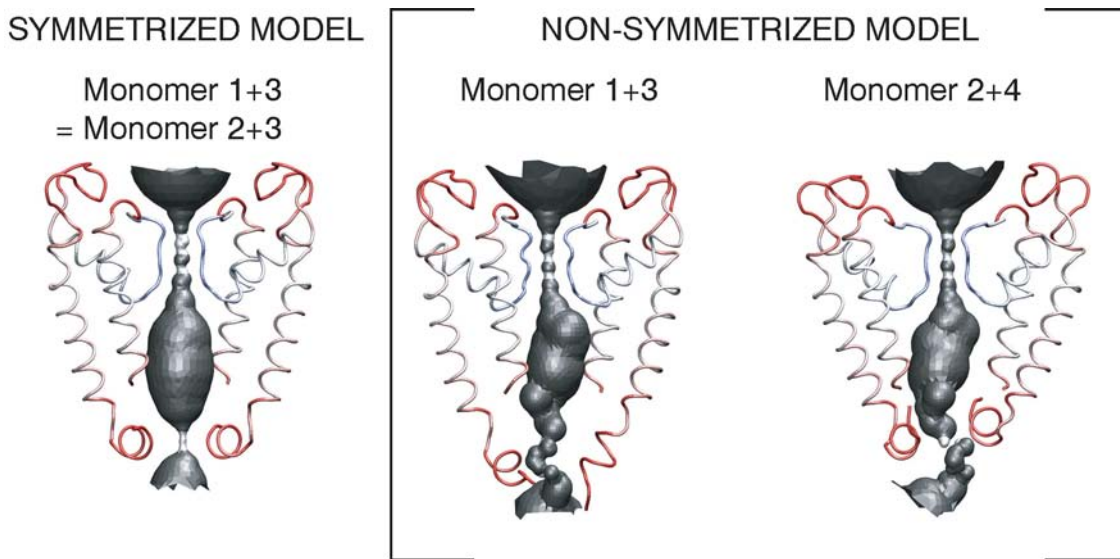


Figure 5.2: KcvP13A average structures (For clarity, only two of four monomers are shown). The symmetrized model is shown left. The center and the right picture show two alternate opposite monomers of the non-symmetrized model. The color codes for the backbone atomic B factors (blue: $< 10 \text{ \AA}^2$, red: $> 20 \text{ \AA}^2$). HOLE analysis is included in form of grey cylinder in the center of the models.

similar to K^+ dynamics in the KB-KcvP13A simulation. A K^+ blockage as observed in the trajectories of the knock-out mutants Kcv Δ N8, Kcv Δ N14, and KB-Kcv Δ N9 was not found.

Average Structures

Figure 5.2 shows two monomers per model together with the color-coded backbone atomic B factors averaged over the final 4.5 ns of rigid filter runs. The picture to the left shows the symmetrized model. The pictures in the center and to the right show two opposite monomers of the non-symmetrized model. Furthermore, the accessible free volume from HOLE analysis is included.

In the symmetrized structure, the kink of the initial homology model is preserved. This is equivalent to the wild type models KcvWT and KB-KcvWT, but not to the analogous P13A model KB-KcvP13A. The elongation of TM1 as observed in the latter model and predicted in (1) did not occur. However, such an elongation was also observed in the MD simulation, thus, the validity of this model is in doubt.

The non-symmetrized model provides some clarity. Only two opposite monomers preserve the kink, while the TM1 of the two remaining monomers tend to elongate. This mirror-symmetric model comes closer to the protein configuration as observed in the MD simulation.

All models appear to be in closed conformation, since the intracellular mouth is too small to allow the passage of K^+ ions.



Figure 5.3: KcvWT: Visualization of the slowest mode from normal-mode analysis as observed from the cystosolic site. The s-helix is colored red. The direction of motion is indicated by red arrows. Elongated conformations: left and right; intermediate conformation: center.

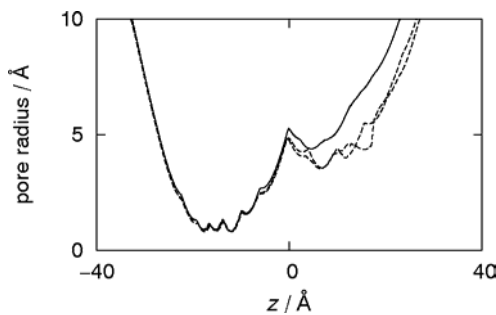


Figure 5.4: KcvWT pore-radius as a function of the z -coordinate of the fluctuation conformations. Solid line: Intermediate conformation; dashed lines: elongated conformations. Location of the selectivity filter: $-5 \text{ \AA} < z < -15 \text{ \AA}$. Location of the intracellular mouth: $10 \text{ \AA} < z < 20 \text{ \AA}$. Since the amplitude is scalable, the absolute difference must not be overestimated. However, the trend is meaningful.

Cooperated Large-Scale Motions

Cooperated large-scale motions like gating caused by protein folding remain beyond the reach of current MD simulation. However, a computational approach for exploring such large-scale dynamics in proteins is normal-mode analysis (NMA) (2). Normal modes from a simple elastic network model with small eigenvalues, so-called "slow" modes, can be interpreted as relevant for the gating process of K^+ channels. This has been shown for the available X-ray structures quite recently (3,4). Such models are in a sense limited since they cannot for instance yield information about coupling between filter and mouth region, or large-scale conformational motion that visits multiple energetic basins.

NOMAD (5) with its built-in elastic network model was used to apply all-atom NMA to KcvWT (Chapter 3), because this model was determined as the most relevant one. The results were compared to the structure of the non-symmetrized KcvP13A model. Figure 5.3 visualizes the slowest mode of the intermediate conformation (center) and both elongation conformations (left and right) of KcvWT. The concerted motion is mirror-symmetric, with two opposite helices moving to and from the center. The s-helices are subject to the largest motion and define the intracellular constriction. Since the amplitude is scalable, the absolute difference must not be overestimated. However, the tendency is meaningful.

Additional information concerning the intracellular mouth were obtained from HOLE analysis. Figure 5.4 depicts the pore-radius of the different conformations as a function of the z coordinate. In all cases, the filter-region turns out to be the most severely restrained element of the structure. This is consistent with the restraint-free simulation run, where the fluctuation of the filter region was small. This is also consistent with the NMA of various K^+ channel X-ray structures (3). The relevance of the lowest mode becomes clear by comparing the intracellular constriction of the different conformations located between $z = 10 \text{ \AA}$ and $z = 20 \text{ \AA}$. The pore of the intermediate conformation (solid line) is larger compared to both elongated conformations (dashed lines), which indicates that this mode is possibly related to the gating mechanism of Kcv.

It is remarkable that the non-symmetrized P13A structure resembles closely the elongated geometry of the slowest WT mode. Since the N-terminus of KB-Kcv and Kcv is suspected to be involved in the gating mechanism (Chapters 2 and 3) one can speculate that a closed inner gate state for the P13A model was found. Creating an open, functional P13A conformation would require much longer simulation time or an initial structure that is already close to the desired state. The open state could be structurally similar to the transition state of the slowest normal mode (see Figure 5.5). Given the available data, the reason for the hyperactivity of the native KcvP13A system can therefore not be conclusively determined yet. In light of the results for KB-KcvP13A more work is required in order to develop a common interpretation.

Reference

1. Hertel B., S. Tayefeh, M. Mehmel, S. M. Kast, J. L. Van Etten, A. Moroni, and G. Thiel. 2006. Elongation of outer transmembrane domain alters function of miniature K^+ channel Kcv. 2006. *J. Membr. Biol.* 210:21-29.
2. Brooks, B., and M. Karplus. 1983. Harmonic dynamics of proteins: normal modes and fluctuations in bovine pancreatic trypsin inhibitor. *Proc. Natl. Acad. Sci. USA.* 80:6571-6757.
3. Shrivastava, I. H., and I. Bahar. 2006. Common Mechanism of Pore Opening Shared by Five Different Potassium Channels. *Biophys. J.* 90:3929-3940.
4. Shen, Y., Y. Kong, and J. Ma. 2002. Intrinsic flexibility and gating mechanism of the potassium channel KcsA. *Proc. Natl. Acad. Sci. USA.* 99:1949-1953.
5. Lindahl E., C. Azuara, P. Koehl, and M. Delarue. 2006. NOMAD-Ref: visualization, deformation and refinement of macromolecular structures based on all-atom normal mode analysis. *Nucleic Acids Res.* 34:W52-W56.

Chapter 6

General Conclusion

Basic functional properties and the impact of mutations on the structure and the function of the K^+ channel Kcv with the focus on the essential N-terminal region (1,2,3) were investigated by computational means. Plausible atomistic models for the characterization of features of Kcv wild-type, some dysfunctional truncation mutants, and the hyperactive point mutant P13A were constructed. Two routes towards model development were pursued: one was based on a "functional analog", which was a truncated and mutated KirBac1.1 system, and the other was based on homology modeling. For the latter, data from NMR spectroscopy and electrophysiology was taken into account. Their structure, thermodynamics, and dynamics in explicit membrane and solvent were explored on the basis of extensive MD simulations, and novel analysis methodology was applied to the results. Figure 6.1 summarizes all simulation systems.

6.1 Plausibility and Stability of the Models

Homology modeling with the alignment strategy outlined in this work leads to generally meaningful initial geometries. Subsequent MD simulations are generally useful for discriminating the quality of the models. This turned out to particularly important for highly flexible regions like the N-termini that were the focus of this work, and for the determination of plausible protonation states of crucial charged residues.

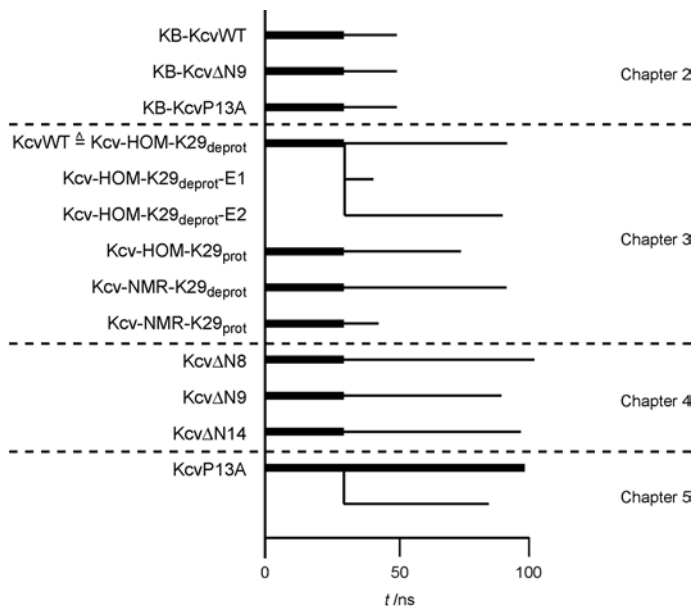


Figure 6.1: Equilibration and simulation protocol for the calculations presented in this thesis and their relation to the chapters. The thick lines represent the trajectories where the atoms of the selectivity filter were constrained. The thin lines represent the trajectories where these restraints were removed. The terminology of the models is explained in Appendix II.

6.2 Validity of the Functional Analogy Hypothesis

The most striking dynamic and structural properties shared by the models based on the KirBac1.1 sequence with those based on the Kcv sequence are: 1) A kink between TM1 and the slide-helix is preserved in all wild-type models (Chapters 2 and 3). 2) This kink tends to disappear in both P13A models during the MD simulations (Chapters 2 and 5). 3) The cytosolic constriction of all symmetrized models is rather wide, thus, these models appear to be in the open, not necessarily conductive, conformation (Chapters 2-5). 4) In all models, the loop, the slide-helix, and the terminal TM2 region exhibit high flexibility (Chapters 2-5). 5) The salt-bridge patterns at the cytosolic side of any analog KirBac1.1 and Kcv model are similar (Chapters 2-4). 6) The characteristics of ion transition into and out of the cavity are similar for any analog KirBac1.1 and Kcv model (Chapters 2-5). 7) Despite the open configuration of the truncation models, K^+ blockage near their cytosolic mouth prevents K^+ ions from entering the cavity (Chapters 2 and 4). This is in either case related to the missing salt bridges between C-termini and nearby positive residues. The C-termini play the role of "turnstiles" for ion passage. 8) The potassium density distributions are topographically similar for all models; specific differences occur at precisely the points of mutation and correlate directly with changes of functionality (Chapters 2-4).

Since all analog KirBac1.1 and Kcv models share these features, it is evident that some key properties of K^+ channels are independent from the individual protein sequence. This statement holds as long as the sequence allows the appropriate K^+ channel folding and if certain pivotal residues are present. Remarkably, both models share these properties despite a low sequence identity of ~ 10% which is typical for K^+ channels (4).

6.3 Ionization State of the Membrane-Exposed Residue Lys29

The results from calculations in combination with experiments presented in Chapter 3 indicate that *in vivo* the deprotonated state of Lys29 is favored: 1) Maximal stability of protein and membrane as well as spontaneous ion transitions were only observed in the deprotonated model. The characteristics of the ion-transition performed by the model channel are widely consistent with proposed transition mechanism of K^+ channels (5,6,7,8,9,10). 2) In electrophysiological experiments, a Lys29 to Ala29 mutant exhibited the same functional properties as the Kcv wild type. If a protonated state of Lys29 was essential for the function of Kcv, the functional properties should have been different.

6.4 The N-terminal region

The effect of all mutations was limited nearly exclusively to the N-terminal slide-helix and, to a much lesser degree, to the terminal region of the inner helix, TM2.

6.4.1 Speculations about the role of the N-terminal slide-helix for gating.

Large-scale concerted motion of the N-termini is the characteristic property of the slowest mode identified from normal mode analysis of an elastic network model of wild-type structures. Furthermore, the deprotonated NMR-based model is remarkably stable and its inner mouth appears to be closed. Thus, there is evidence that the N-termini themselves can act as the cytosolic gate (Chapters 2, 3, and 5). The KcvP13A system, however, marks the limit of computational

capabilities for understanding the gating process: although the non-symmetrized structure resembles closely the terminal, elongated state found for the slowest NMA mode, apparently a closed configuration was found. Molecular timescales for adequate sampling of open/close transitions is still too large to be reached by current computers.

6.4.2 The interaction between the N-terminus and the C-terminus and its role for conductance.

For the truncated mutants, all observables agree with the assumption that the cytosolic side is in its open state. However, in marked contrast to the wild-type, K^+ transition from the cytosolic site into the cavity is inhibited. These results indicate that the truncation mutants form an open yet dysfunctional pore state.

The interaction between the N-terminus and the C-terminus decreases in the N-terminal truncation mutants that lack positively charged residues in the shortened slide-helix. As a consequence, the interaction between the C-terminus and K^+ ions is increased. This correlates with a change of local permeability of the inner mouth constriction (Chapters 2 and 4). Ion transport through the inner mouth is accompanied by coordination and subsequent release by the C-terminal carboxylate. A K^+ blockage at the inner mouth constriction emerges.

The free energy surface governing K^+ transport is apparently characterized by the balance between two competing terms: on one hand, it must not be too strongly attractive since otherwise barriers along the transition pathway become insurmountable. On the other hand, a not too shallow free energy sink must exist in order to guarantee sufficient probability for ions to be found near the mouth. In the filter region, a deep free energy sink exists as well (Figures 2.8 and 4.3 right). In contrast, the filter free energy surface appears to be much more robust since the multi-site filter geometry enforces coordinated ion motion. It remains to be seen whether such an N-terminal free energy balance is a feature of other K^+ channels as well.

References

1. Moroni, A., C. Visconti, V. Sangiorgio, C. Pagliuca, T. Meckel, F. Horvath, S. Gazzarrini, P. Valbusza, J. L. Van Etten, D. DiFrancesco, and G. Thiel. 2002. The short N-terminus is required for functional expression of the virus-encoded miniature K^+ channel Kcv. *FEBS Lett.* 530:65-69.
2. Hertel, B. 2005. Struktur-Funktions-Beziehung in dem minimalen viralen K^+ Kanal Kcv: Funktionelle Rolle des N-terminus bei der Regulation von Kanalaktivität. PhD-Thesis. Technische Universität Darmstadt.
3. Hertel, B., S. Tayefeh, M. Mehmel, S. M. Kast, J. L. Van Etten, A. Moroni, and G. Thiel. 2006. Elongation of outer transmembrane domain alters function of miniature K^+ channel Kcv. *J. Membrane Biol.* 210:1-9.
4. Jan, L. Y. and Y. N. Jan. 1997. Voltage-gated and inwardly rectifying potassium channels. *J. Physiol.* 505:267-282.
5. Berneche, S., and B. Roux. 2001. Energetics of ion conduction through the K^+ channel. *Nature*. 414:73-77.
6. Morais-Cabral, J. H., Y Zhou, and R. MacKinnon. 2001. Energetic optimization of ion conduction rate by the K^+ selectivity filter. *Nature*. 414:37-42.
7. Allen, T. W., S. Kuyucak, and S.-H. Chung. 1999. Molecular dynamics study of the KcsA potassium channel. *Biophys J.* 77:2502-2516.
8. Shrivastava, I. H. and M. S. P. Sansom. 2000. Simulations of ion permeation through a potassium

-
- channel: molecular dynamics of KcsA in a phospholipid bilayer. *Biophys J.* 78:557-570.
9. Berneche, S. and Benoit Roux. 2003. A microscopic view of ion conduction through the K^+ channel. *Proc Natl Acad Sci USA.* 100:8644-8648.
10. Fatemeh, K.A., Tajkhorshid W., and K. Schulten. 2006. Dynamics of K^+ ion conduction through Kv1.2. *Biophys J.* 91: L72-L74.

Zusammenfassung

Der K⁺-Kanal Kcv aus dem *Paramecium bursaria* Chlorellavirus ist der kleinste bekannte K⁺-Kanal dessen Funktion nachgewiesen wurde. Er eignet sich als Minimalmodell für die Aufklärung von Struktur-Funktions-Zusammenhängen bei K⁺-Kanalproteinen.

Gegenstand der vorliegenden Arbeit war die computergestützte Studie der Auswirkung verschiedener Mutationen des Kcv-N-Terminus auf die Kcv-Funktion. Mit Hilfe molekular-dynamischer Simulationen von K⁺-Kanal-Modellen in expliziter Membran und explizitem Solvens wurden die Struktur, Dynamik, und Thermodynamik verschiedener Modellsysteme auf atomarer Skala untersucht. Von besonderem Interesse waren neben dem Wildtyp die hyperaktive Punktmutante KcvP13A, sowie die zwei inaktiven Deletionsmutanten KcvΔN8 und KcvΔN14. Der Protonierungszustand einer Schlüsselaminoäure (Lys29) war ebenfalls Gegenstand eingehender Untersuchung.

Bei der Modellbildung wurde angenommen, dass analoge Topologie auch analoge Funktionalität zur Folge hat. Folglich wurden Kcv-Homologiemodelle, wie auch in Analogie zu Kcv adaptierte KirBac1.1 Kristallstruktur-Modelle untersucht und miteinander verglichen.

Ferner wurde eine neue Methode entwickelt, um symmetrische Erwartungswertstrukturen aus sehr langen Trajektorien zu extrahieren. Die an Hand dieser Methode berechneten Geometrien sind aus strukturbiologischer Sicht interpretierbar und erlauben die weitere Untersuchung mit fortgeschrittenen Methoden wie z.B. der Poisson-Boltzmann-Theorie oder der 3D-RISM-Integralgleichungstheorie. Mit Hilfe letzterer war es möglich, die Ionenverteilung um das Protein vorherzusagen und den Einfluss von Mutationen auf diese zu untersuchen.

Die wichtigsten Ergebnisse lauten:

1. In dieser Arbeit wurden Richtlinien entwickeln, die die Konstruktion von plausiblen K⁺-Kanal-Homologiemodellen ermöglichen. Es stellte sich heraus, dass ein solches Modell geeignet war den vollständigen Kaliumtransport von einer Seite der Membran zur anderen zu simulieren.
2. Die Interaktion positiv geladener Aminosäuren in der N-terminalen Helix ("slide-Helix") mit dem C-Terminus führt zu mutantenabhängigen Salzbrückenmustern. Eine Schwächung dieser Interaktion korreliert mit dem Verlust der Leitfähigkeit.
3. Der N-Terminus kann als sterische Barriere für den Eintritt von K⁺-Ionen agieren und somit zum "Gating"-Mechanismus beitragen. Der Mechanismus unterscheidet sich allerdings deutlich von dem der cytosolischen "Gates" anderer K⁺-Kanäle. Die bisherige Annahme, dass im Kcv lediglich der Selektivitätsfilter als "Gate" agieren kann, muss somit relativiert werden. Andererseits bedeutet die Präsenz eines offenen "Mouths" nicht notwendigerweise, dass auch tatsächlich eine leitfähige Form vorliegt.
4. Der Protonierungszustand von Lys29 in der Simulation war entscheidend für den Eintritt von K⁺-Ionen in den Kanal. Möglicherweise trägt der Protonierungszustand dieser Aminosäure zum "Gating"-Mechanismus bei.
5. Die Annahme, dass eine funktionelle Analogie zwischen Kaliumkanälen existiert, ist berechtigt. Viele Eigenschaften der Kcv-Modelle stimmen mit denen eines weiteren untersuchten analogen Kanals überein, obwohl die Proteinsequenzidentität der beiden untersuchten Modelle nur 10% beträgt.
6. Die vorliegenden Daten reichen nicht aus, um die Hyperaktivität der P13A Mutante zu erklären. Weitere Untersuchungen sind nötig, um ein besseres Modell dieser Mutante zu generieren.

APPENDIX I

Abbreviations

(For a detailed terminology of the channel models, refer to Appendix II)

DNA	Deoxyribonucleic acid
GFP	Green fluorescent protein (from <i>Aequoria victoria</i>)
HNC	hypernetted chain
KcsA	K^+ channel from <i>Streptomyces lividans</i>
Kcv	K^+ channel from <i>Paramecium bursaria</i> chlorella virus (PBCV-1)
KH	Kovalenko-Hirata
KirBac1.1	K^+ channel from <i>Burkholderia pseudomallei</i>
Kv1.2	K^+ channel from <i>Rattus norvegicus</i>
KvAP	K^+ channel from <i>Aeropyrum pernix</i>
MD	Molecular dynamics
MDIIS	Modified direct inversion of interactive subspace
MthK	K^+ channel from <i>Methanobacterium thermoautotrophicum</i>
NMA	Normal mode analysis
NMR	Nuclear magnetic resonance
p-helix	Pore-helix
PBCV-1	<i>Paramecium bursaria</i> chlorella virus
PB	Poisson-Boltzmann
PDB	Protein data base
PMF	Potential of mean force
RISM	Reference interaction site model
RMSD	Root-mean-square deviation
RMSF	Root-mean-square fluctuation
s-helix	Slide-helix
TIP3P	Transferable interaction potential 3 point
TM	Transmembrane domain
tRNA	Transfer ribonucleic acid

APPENDIX II

The terminology of the models

X-ray structure of KirBac1.1 adapted in analogy to Kcv (Chapter 2):

KB-KcvWT	KirBac1.1 X-ray structure truncated in analogy to Kcv wild type.
KB-KcvΔN8	KirBac1.1 X-ray structure truncated in analogy to the Kcv ΔN8 mutant.
KB-KcvP13A	KirBac1.1 X-ray structure truncated and mutated in analogy to the Kcv P13A mutant.

Homology Models (Chapter 3-5):

KcvWT	Kcv wild type, synonym for Kcv-HOM-K29 _{deprot} .
Kcv-HOM-K29 _{deprot}	Kcv wild type with lysine (K) 29 in the deprotonated state .
Kcv-HOM-K29 _{deprot} -E1	Kcv-HOM-K29_{deprot} simulated with an external electrostatic field, 1st trajectory .
Kcv-HOM-K29 _{deprot} -E2	Kcv-HOM-K29_{deprot} simulated with an external electrostatic field, 2nd trajectory .
Kcv-HOM-K29 _{prot}	Kcv wild type with lysine (K) 29 in the protonated state .
KcvΔN8	Kcv mutant with the N-terminal truncated by 8 amino acids .
KcvΔN9	Kcv mutant with the N-terminal truncated by 9 amino acids .
KcvΔN14	Kcv mutant with the N-terminal truncated by 14 amino acids .
KcvP13A	Kcv mutant where the proline at position 13 was mutated to alanine .

Chimera Models based on homology modeling and experimental NMR structure (Chapter 3):

Kcv-NMR-K29 _{deprot}	Kcv wild type model with incorporated NMR structure data and lysine (K) 29 in the deprotonated state .
Kcv-NMR-K29 _{prot}	Kcv wild type model with incorporated NMR structure data and lysine (K) 29 in the protonated state .

APPENDIX III

1- and 3-Letter Code of the standard amino acids

Amino Acid	3-Letter	1-Letter
Alanine	Ala	A
Arginine	Arg	R
Asparagine	Asn	N
Aspartic acid	Asp	D
Cysteine	Cys	C
Glutamic acid	Glu	E
Glutamine	Gln	Q
Glycine	Gly	G
Histidine	His	H
Isoleucine	Ile	I
Leucine	Leu	L
Lysine	Lys	K
Methionine	Met	M
Phenylalanine	Phe	F
Proline	Pro	P
Serine	Ser	S
Threonine	Thr	T
Tryptophan	Trp	W
Tyrosine	Tyr	Y
Valine	Val	V

APPENDIX IV

List of scientific computer program

Local codes

Name	Purpose, programming language, and author
3D-RISM	3D-RISM calculations Fortran95 code written by S. M. Kast and T. Kloss.
Trajtool	Trajectory analysis and calculation of average distance from trajectories for restrained annealing. C++ code written by S. Tayefeh.

External programmes

Name	Purpose and reference
Alscript	Visualization of alignments. Barton, G. J. 1993. ALSCRIPT - A Tool to Format Multiple Sequence Alignments. <i>Prot. Eng.</i> 6:37-40.
Blast	Basic local alignment and sequence database search. Altschul, S. F., T. L. Madden, A. A. Schaffer, J. Zhang, Z. Zhang, W. Miller, and D. J. Lipman. 1997. Gapped BLAST and PSI-BLAST: a new generation of protein database search programs. <i>Nucleic Acids Res.</i> 25:3389-3402.
CHARMM	Poisson-Boltzmann calculations, trajectory analysis, simulation-box setup, energy minimization, initial molecular dynamics simulations, simulated annealing. Brooks, B. R., R. E. Brucolari, B. D. Olafson, D. J. States, S. Swaminathan, and M. Karplus. 1983. CHARMM: a program for macromolecular energy, minimization, and dynamics calculations. <i>J. Comput. Chem.</i> 4:187-217.
ClustalX	Multiple Sequence Alignment. Thompson, J. D., T. J. Gibson, F. Plewniak, F. Jeanmougin, and D. G. Higgins. 1997. The CLUSTAL X windows interface: flexible strategies for multiple sequence alignment aided by quality analysis tools. <i>Nucleic Acids Res.</i> 25:4876-4882.
Hole	Analysis of the pore dimensions of the holes through ion channels. Smart, O. S., J. G. Neduvilil, X. Wang, B. A. Wallace, and M. S. P. Sansom. 1996. HOLE: a program for the analysis of the pore dimensions of ion channel structural models. <i>J. Mol. Graph.</i> 14:354-360.
JalView	Sequence alignment editor and alignment visualization. Clamp, M., J. Cuff, S. M. Searle, and G. J. Barton. 2004. The Jalview Java Alignment Editor. <i>Bioinformatics</i> . 20:426-427.

Molcad	Molecular graphics and volume rendering. Brickmann, J., T. Goetze, W. Heiden, G. Moeckel, S. Reiling, H. Vollhardt, and C. D. Zachmann C.-D. 1995. Tools for Insight and Innovation. In Data Visualization in Molecular Science. J. E. Bowie, editor. Addison-Wesley, Reading, Pennsylvania. 83-97.
Modeller	Homology modeling and evaluation of structures. Marti-Renom M. A., A. Stuart, A. Fiser, R. Sánchez, F. Melo, and A. Sali. 2000. Comparative protein structure modeling of genes and genomes. <i>Annu. Rev. Biophys. Biomol. Struct.</i> 29:291-325.
NAMD	Massive parallel molecular dynamics simulation. Kale, L., R. Skeel, M. Bhandarkar, R. Brunner, A. Gursoy, N. Krawetz, J. Phillips, A. Shinozaki, K. Varadarajan, and K. Schulten. 1999. NAMD2: greater scalability for parallel molecular dynamics. <i>J. Comput. Phys.</i> 151:283-312.
NOMAD	Normal Mode Analysis. Lindahl E., C. Azuara, P. Koehl, and M. Delarue. 2006. NOMAD-Ref: visualization, deformation and refinement of macromolecular structures based on all-atom normal mode analysis. <i>Nucleic Acids Res.</i> 34:W52-W56.
PROCHECK	Structural evaluation. Laskowski, R. A., MacArthur, M. W., Moss, D. S., and J. M. Thornton. 1993. PROCHECK: A program to check the stereochemical quality of protein structures. <i>J. Appl. Cryst.</i> 26:283-291.
PROSA	Structural evaluation. Sippl, M.J. 1993. Recognition of Errors in Three-Dimensional Structures of Proteins. <i>Proteins.</i> 17:355-362.
PROF	Prediction of the secondary protein structure. Rost, B. 2001. Protein Secondary Structure Prediction Continues to Rise. <i>J. Struct. Biol.</i> 134:204-218.
PSI-BLAST	Basic local alignment and sequence database search. (for reference see "Blast")
SYBYL	Molecular mechanics. SYBYL (Tripos Inc., St. Louis, MO).
TMHMM	Prediction of transmembrane domains. Sonnhammer E. L. L, G. von Heijne, and A. Krogh. 1998. A hidden Markov model for predicting transmembrane helices in protein sequences. In Proceedings of the Sixth International Conference on Intelligent Systems for Molecular Biology. J. Glasgow, T. Littlejohn, F. Major, R. Lathrop, D. Sankoff, and C. Sørensen, editors. AAAI Press Menlo Park, CA. 175-182.
TMPred	Prediction of transmembrane domains. Hofmann, K., and W. Stoffel. 1993. TMbase - A database of membrane spanning proteins segments. <i>Biol. Chem. Hoppe-Seyler.</i> 374:166.
VMD	Vizualization and trajectory analysis. Humphrey, W., A. Dalke, and K. Schulten. 1996. VMD: Visual molecular dynamics. <i>J Mol Graphics.</i> 14:33-38.

APPENDIX V

Computer hardware used for calculations

Local linux computers used for trajectory analysis:

- Dell Precision 670, 2x Intel Xeon CPUs at 3GHz, 4GB Ram. Suse 10.0, 64bit.
- Transtec 2100, 2x Dual Core Opteron 270 CPU at 2GHz, 16GB Ram. Suse 10.1-10.2, 64bit.

Linux Computer Cluster used for simulation box setup:

- CSC I at the Universität Frankfurt. 140x Pentium IV Xeon at 2.4GHz. 70 nodes with 2CPUs and 2GB RAM per node. Red Hat Linux 32bit.
- CSC II at the Universität Frankfurt. 564x AMD Opteron 244 at 1.8GHz. 282 nodes with 2CPUs and up to 16GB RAM per node. Red Hat Linux 64bit.

IBM Regatta Shared Memory Machines used for molecular dynamics simulation production run:

- Hessischer Hochleistungsrechner (HHLR) at the Hochschulrechenzentrum (HRZ) Darmstadt. 512 IBM p575 CPUs at 1.9GHz, 62 SMP frames, up to 16 CPUs and 64GB Ram per frame. AIX5.2.
- JUMP at the Forschungszentrum Jülich. 1312 IBM p690 CPUs at 1.7GHz, 41 SMP frames, 32 CPUs and 128GB per frame. AIX5.2.

Curriculum Vitae

Persönliche Daten

Name	Tayefeh
Vorname	Sascha
Geburtstag	30.05.1974
Geburtsort	Hanau

Studium

11/2003 – 07/2007	Promotionsstudium am Institut für Botanik der Technischen Universität Darmstadt in der Arbeitsgruppe von Prof. Dr. Thiel in enger Kooperation mit dem Eduard-Zintl Institut für Anorganische und Physikalische Chemie der Technischen Universität Darmstadt in der Arbeitsgruppe von PD. Dr. S. M. Kast. Thema: „ <i>Computational study of the Kcv potassium channel</i> “. Abschluss: Promotion.
09/2002 – 07/2003	Diplomarbeit am Institut für Botanik der Technischen Universität Darmstadt in der Arbeitsgruppe von Prof. Dr. Thiel. Thema: "Die Anzahl einwärtsgleichrichtender K^+ Kanäle in Abhängigkeit von der Größe der Plasmamembranoberfläche bei Schließzellprotoplasten von Vicia faba".
10/1993 – 07/2003	Studium der Biologie an der Technischen Universität Darmstadt. Schwerpunkt: Pflanzenphysiologie, Spezielle Botanik, Ökologie. Abschluss: Diplom.

Schulausbildung

09/1985 – 06/1993	Goethe-Gymnasium, Bad Ems. Abschluss: Abitur.
09/1980 – 06/1984	Freiherr-von-Stein Grundschule, Bad Ems

Danksagung

An dieser Stelle möchte ich mich bei allen bedanken, die zum Entstehen der vorliegenden Arbeit beigetragen haben. Mein Dank gilt:

Stefan Kast herzlichst für die Möglichkeit, als Teil seiner Arbeitsgruppe diese Arbeit anzufertigen und für seine Betreuung, Expertise, Hilfestellungen und Geduld. Außerdem ganz besonderen Dank für die Bereitstellung all der Technik, ohne die die ganze Arbeit nicht möglich gewesen wäre.

Gerhard Thiel für die Betreuung und ganz besonders für die Einladungen zu all den Konferenzen und Reisen.

Brigitte Hertel für ihre wissenschaftlichen Beiträge zu dieser Arbeit und für die hervorragende Zusammenarbeit. Ganz besonders bedanke ich mich für die Fürsorge und "Rettung" im Rahmen der Bergtour in Hirschgägg.

Thomas Kloss für 3D-RISM Integralgleichungsrechnungen, ohne die viele Interpretationen an den Modellen unmöglich gewesen wären. Außerdem für drei Jahre hervorragender kollegialer Zusammenarbeit und viel Spaß.

Manuela Gebhardt und Dirk Baumeister für die elektrophysiologischen Messungen an den Lys29 Mutanten.

Michael Kreim für die Produktion der Trajektorien mit angelegtem externem Feld.

Allen Mitarbeitern der AG Kast, AG Brickmann und Molcad Forschungsstelle für den herzlichen Umgang, der ständigen Hilfsbereitschaft, die Geduld und die anregenden Diskussionen bei den gemeinsamen Mittagessen.

Allen Mitarbeitern der AG Thiel und AG Moroni für den herzlichen Umgang und der angenehmen Zeit auf Reisen und Konferenzen.

Ausdrücklicher Dank geht an:

Thorsten Borosch, Bernd Schilling, Thosten Schepers, Andreas Seeger und Hans-Jürgen Bär für ihre ständige Bereitschaft, sämtliche meiner Fragen zur allgemeinen und physikalischen Chemie, sowie zur Mathematik zu beantworten und so ihr fundiertes Wissen mit mir zu teilen.

Jürgen Brickmann für all die Einladungen zum essen, sowie für weitere Subventionen dieser Arbeit.

Anna Moroni für die Gastlichkeit und die Beherbergung in Italien.

Stefan Buchhofer, Andreana Clemenz, Lutz Lelgemann, Jens Illig, Susso Schüller und Thorsten Metz für ihre langjährige Freundschaft, den Spaß in Guten und ihre Unterstützung in schlechten Zeiten.

Oliver Korb für all die fruchtbaren Diskussionen und Hilfestellungen im Rahmen der objekt-orientierten Programmierung mit C++.

Allen Mitarbeitern der AG Exner für viel Spaß und die gute Atmosphäre bei den Konferenzen in Erlangen.

Meine Freundin Lena Hamming für die seelische und moralische Unterstützung während der gesamten, und ganz besonders während der letzten Wochen meiner Promotion.

Meine Eltern für ihre langjährige Unterstützung und Liebe, ohne die das alles nicht möglich gewesen wäre.

Eidesstattliche Erklärung

Ich erkläre an Eides statt, dass ich die vorliegende Dissertation selbstständig und nur mit den angegebenen Hilfsmitteln angefertigt habe.

Sascha Tayefeh